

**INVESTIGATION OF SELF-HEATING AND
MACROSCOPIC BUILT-IN POLARIZATION EFFECTS
ON THE PERFORMANCE OF III-V NITRIDE DEVICES**

A Dissertation
Presented to
The Academic Faculty

by

Anusha Venkatachalam

In Partial Fulfillment
of the Requirements for the Degree
Doctor of Philosophy in the
School of Electrical and Computer Engineering

Georgia Institute of Technology
August 2009

INVESTIGATION OF SELF-HEATING AND MACROSCOPIC BUILT-IN POLARIZATION EFFECTS ON THE PERFORMANCE OF III-V NITRIDE DEVICES

Approved by:

Dr. Paul Douglas Yoder, Advisor
School of Electrical and Computer
Engineering
Georgia Institute of Technology

Dr. Samuel Graham
School of Mechanical Engineering
Georgia Institute of Technology

Dr. Benjamin Klein
School of Electrical and Computer
Engineering
Georgia Institute of Technology

Dr. Paul Voss
School of Electrical and Computer
Engineering
Georgia Institute of Technology

Dr. Janet K. Allen
School of Mechanical Engineering
Georgia Institute of Technology

Date Approved: 30 June 2009

To my family.

ACKNOWLEDGEMENTS

First of all I would like to thank my thesis advisor Dr. Douglas Yoder for giving me an opportunity to work in such an exciting field, and for believing in my abilities. Without his support and encouragement, I would not have been able to complete this thesis.

I would like to thank Dr. Benjamin Klein for his guidance in my research. I would like to express my gratitude to my committee members Dr. Samuel Graham, Dr. Paul Voss, and Dr. Janet K. Allen for taking the time to review my thesis and provide their insightful comments and suggestions. I would also like to thank Dr. Alexey Maslov and Dr. Jiangrong Cao from Canon Development Americas Inc., and Dr. Michael Povolotskyi at Georgia Tech Savannah for their valuable insights.

My special thanks to all the staff members at Georgia Tech Savannah, especially Mrs. Patricia Potter, for all the help during my study. All my colleagues and friends at Georgia Tech Savannah deserve a special thank you as well.

Finally, none of this would have been possible without the unconditional love and support of my family. I dedicate this thesis to them.

TABLE OF CONTENTS

DEDICATION	iii
ACKNOWLEDGEMENTS	iv
LIST OF TABLES	vii
LIST OF FIGURES	viii
SUMMARY	xiii
I INTRODUCTION	1
1.1 Motivation and objective	1
1.2 Organization of the thesis	1
1.3 Nitrides in electronics	2
1.4 Nitrides in optoelectronics	6
II OVERVIEW OF III-NITRIDES	11
2.1 Basic material properties	11
2.2 Phonons in GaN	13
2.3 Spontaneous and piezoelectric polarization charges	14
III ELECTROTHERMAL SIMULATION OF ALGAN/GAN HIGH ELECTRON MOBILITY TRANSISTORS	18
3.1 Hot phonon effect in AlGaN/GaN HEMTs	18
3.2 Formulation of the electrothermal problem	21
3.3 Steady state solutions	23
3.4 Efficient solutions of elliptic partial differential equations in two-dimensional semiconductor device simulations	26
3.5 Simulation results	36
3.6 Time-dependent solutions	40
IV SIMULATION OF BULK GAN	43
4.1 MINILASE-A quantum well laser simulator	43
4.2 Introduction to k.p	44

4.3	k.p for wurtzite nitrides	45
4.4	Optical matrix elements	49
4.5	Bulk dispersion	53
4.6	Effect of strain on the bulk bandstructure	53
4.7	Spin-orbit interaction	54
4.8	Verification of the bulk dispersion calculations	55
V	SIMULATION OF INGAN-BASED QUANTUM WELL STRUCTURES	58
5.1	Quantum well dispersion	58
5.2	Inclusion of polarization charges in k.p	60
5.3	Calculation of optical gain	62
5.4	Validation of quantum well dispersion calculations	66
VI	SIMULATION OF NON-(0001) INGAN-BASED LASERS	69
6.1	c-axis vs. non-c-axis	69
6.2	Formulation of the k.p Hamiltonian for arbitrary crystal orientation	71
VII	DESIGN STRATEGIES FOR INGAN-BASED GREEN LASERS	88
7.1	Optimization of TE optical gain	88
VIII	CONCLUSION AND FUTURE RESEARCH DIRECTIONS	100
8.1	Conclusion	100
8.1.1	Electrothermal simulation of AlGa _N /Ga _N HEMTs	100
8.1.2	Simulation of InGa _N -based quantum well lasers	100
8.1.3	Design of InGa _N -based green lasers	101
8.2	Future research directions	101
8.2.1	Electrothermal analysis of metal-oxide-semiconductor HFETs	102
8.2.2	Thermal analysis of InGa _N -based laser diodes	102
	REFERENCES	104
	VITA	123

LIST OF TABLES

1	Electrical properties of Si, GaAs, 4H-SiC and GaN [210, 36, 193, 60, 57, 40, 46].	4
2	Lattice constants and bandgap energy of InN, GaN, and AlN [154]. .	12
3	Fill after LU decomposition for a) without RCM, b) with RCM and pseudoperipheral node finder and c) brute force method, for a Tunnel FET, MOSFET and AlGaIn/GaN HEMT.	34
4	Thermal Diffusivities of Substrate Materials	41
5	Material Parameters for GaN [45].	56
6	Material Parameters for GaN and InN.	68
7	Elastic stiffness and piezoelectric coefficients GaN and InN [154]. . . .	81

LIST OF FIGURES

1	Current and future applications of GaN-based transistors [121]. . . .	3
2	(a) Schematic of an AlGa _N /Ga _N HEMT structure, (b) Conduction band diagram showing the two dimensional electron gas (2DEG). . .	6
3	Ternary and quaternary materials used for optoelectronics along with the wavelengths [152].	7
4	Schematic of a semiconductor single quantum well heterostructure. .	10
5	Wurtzite crystal structure formed by two intertwined hexagonal sublattices [155].	12
6	Phonon dispersion of bulk Ga _N showing the different phonon branches [35]	14
7	Crystal orientation of Ga- and N-face of Ga _N [15].	15
8	Orientation of spontaneous and piezoelectric polarization charges in Ga-face ((a) and (b)) and N-face ((c) and (d)) AlGa _N /Ga _N and InGa _N /Ga _N heterostructures. In Ga-face AlGa _N /Ga _N and N-face InGa _N /Ga _N heterostructures, the net polarization-induced sheet charge density at the interface is positive, giving rise to a 2DEG in the smaller bandgap Ga _N and InGa _N layers respectively [15, 14].	16
9	Block diagram of the optical and acoustic phonon generation and decay process in Ga _N [159].	19
10	Schematic representation of the box method discretization for the lattice heat equation.	24
11	Schematic representation of the box method discretization for Poisson equation.	25
12	Original numbering scheme implemented by ISETCAD [1].	27
13	LU decomposition and back substitution time as a function of the number of nodes for a structured mesh.	30
14	Unstructured mesh of an AlGa _N /Ga _N HEMT with 3985 nodes (dimensions in microns).	31
15	Fill introduced during LU decomposition of reindexed coefficient matrix as a function of starting nodes for the unstructured AlGa _N /Ga _N HEMT mesh in Figure 14.	31
16	Unstructured mesh of a Tunnel Field Effect Transistor (FET) with 1254 nodes (dimensions in microns).	32

17	Unstructured mesh of a MOSFET with 2776 nodes (dimensions in microns).	32
18	Unstructured mesh of an AlGaIn/GaN HEMT with 4291 nodes (dimensions in microns).	33
19	Unstructured mesh of an AlGaIn/GaN HEMT with 2507 nodes for which RCM fails to reduce the fill associated with LU decomposition (dimensions in microns).	35
20	Example of limitation of RCM for the HEMT in Figure 19: (a) LU decomposed matrix without RCM. (b) LU decomposed matrix with RCM and pseudoperipheral node finder. (c) LU decomposed matrix with brute force selection of a starting node for RCM.	35
21	Electrostatic potential profile in an Al _{0.15} Ga _{0.85} N/GaN HEMT. An external bias of $V_{gs} = -2$ V and $V_{ds} = 2$ V is applied to the gate and drain contacts.	36
22	Cross section of the Al _{0.15} Ga _{0.85} N/GaN HEMT showing the thermal and electrical grids.	37
23	Spatial distribution of the non-equilibrium LO phonon occupation number in an Al _{0.15} Ga _{0.85} N/GaN HEMT at $V_{ds} = 5$ V [184].	38
24	Spatial distribution of the non-equilibrium LO phonon occupation number in an Al _{0.15} Ga _{0.85} N/GaN HEMT at $V_{ds} = 40$ V [184].	39
25	Acoustic phonon temperature distribution in an Al _{0.15} Ga _{0.85} N/GaN HEMT at $V_{ds} = 40$ V. The peak temperature is 420 K and is located between the gate and drain electrodes [184].	40
26	Peak acoustic phonon temperature in an Al _{0.15} Ga _{0.85} N/GaN HEMT as a function of substrate thickness. An external bias of $V_{gs} = -2$ V and $V_{ds} = 2$ V is applied to the gate and drain contacts.	41
27	1D profile of the peak acoustic phonon temperature in an Al _{0.15} Ga _{0.85} N/GaN HEMT for different substrate materials. An external bias of $V_{gs} = -2$ V and $V_{ds} = 2$ V is applied to the gate and drain contacts.	42
28	Flowchart of the laser simulator	52
29	Valence band dispersion of bulk wurtzite GaN as a function of the longitudinal (k_z) and transverse (k_x) wavevectors (a) unstrained GaN and (b) 1% biaxial compressive strain applied to GaN.	54
30	Valence band dispersion of bulk wurtzite GaN as a function of longitudinal (k_z) and transverse (k_x) wavevectors (a) with spin-orbit interaction and (b) without spin-orbit interaction.	55

31	Unstrained valence band dispersion comparison for bulk GaN (a) Chuang's calculation [45] (b) Present work.	57
32	Strained valence band dispersion comparison for bulk GaN (a) Chuang's calculation [45] (b) Present work.	57
33	Unstrained (solid curve) and strained (dashed curve) valence band dispersion profiles of an $\text{In}_{0.2}\text{Ga}_{0.8}\text{N}/\text{GaN}$ single quantum well. (a) $L_w = 25 \text{ \AA}$ and (b) $L_w=50 \text{ \AA}$	59
34	Conduction and valence band edges and envelope functions of the first conduction and heavy hole bands of a 25 \AA $\text{In}_{0.2}\text{Ga}_{0.8}\text{N}/\text{GaN}$ single quantum well (a) no polarization at the interface and (b) full polarization at the interfaces.	63
35	Conduction and valence band edges and envelope functions of the first conduction and heavy hole bands of a 50 \AA $\text{In}_{0.2}\text{Ga}_{0.8}\text{N}/\text{GaN}$ single quantum well (a) no polarization at the interface and (b) full polarization at the interfaces.	63
36	Flowchart of the interface between the k.p module and the gain calculation module.	65
37	Unstrained valence band dispersion comparison for $\text{In}_{0.2}\text{Ga}_{0.8}\text{N}/\text{GaN}$ (a) $L_w = 25 \text{ \AA}$ and (b) $L_w = 50 \text{ \AA}$	66
38	Strained valence band dispersion comparison for $\text{In}_{0.2}\text{Ga}_{0.8}\text{N}/\text{GaN}$ (a). $L_w = 25 \text{ \AA}$ and (b). $L_w = 50 \text{ \AA}$	67
39	Schematic views of (a) polar (0001) c-plane, (b) non-polar m-plane ($1\bar{1}00$), (c) non-polar a-plane ($11\bar{2}0$), and (d) semi-polar plane ($11\bar{2}2$).	71
40	Relation between the conventional co-ordinate system (x, y, z) and transformed co-ordinate system (x', y', z') . The polar and azimuthal angles are denoted by θ and ϕ respectively.	73
41	Elastic strain as a function of crystal orientation for bulk $\text{In}_{0.2}\text{Ga}_{0.8}\text{N}$	76
42	Spontaneous and piezoelectric polarization charges in (a) barrier and (b) well region of a 3 nm $\text{In}_{0.2}\text{Ga}_{0.8}\text{N}/\text{GaN}$ SQW as a function of crystal orientation.	79
43	Crystal dependence of the net polarization charge ($\Delta P = P_{tot}^b - P_{tot}^w$) at the well/barrier interface of a 3 nm $\text{In}_{0.2}\text{Ga}_{0.8}\text{N}/\text{GaN}$ SQW.	80
44	Transition energy between the first conduction and valence bands as a function of crystal orientation angle of a 3 nm $\text{In}_{0.2}\text{Ga}_{0.8}\text{N}/\text{GaN}$ SQW.	82
45	Valence band dispersion for bulk $\text{In}_{0.2}\text{Ga}_{0.8}\text{N}$ for (a) c-, (b) m-, and (c) a-planes.	83

46	Valence band dispersion of a 3 nm $\text{In}_{0.2}\text{Ga}_{0.8}\text{N}/\text{GaN}$ SQW. (a) c-, (b) m-, and (c) a-planes.	84
47	Conduction and valence band edges and envelope functions of the first conduction and heavy hole bands of a 3 nm $\text{In}_{0.2}\text{Ga}_{0.8}\text{N}/\text{GaN}$ SQW at $\theta=0^\circ$	86
48	Conduction and valence band edges and envelope functions of the first conduction and heavy hole bands of a 3 nm $\text{In}_{0.2}\text{Ga}_{0.8}\text{N}/\text{GaN}$ SQW at $\theta=45^\circ$	86
49	Conduction and valence band edges and envelope functions of the first conduction and heavy hole bands of a 3 nm $\text{In}_{0.2}\text{Ga}_{0.8}\text{N}/\text{GaN}$ SQW at $\theta=90^\circ$	87
50	Transition energy as a function of well width for 28% and 30% indium mole fractions in the well. The barrier material is $\text{In}_{0.06}\text{Ga}_{0.94}\text{N}$ and the barrier width is 13.4 nm. The carrier density is $3 \times 10^{19} \text{ cm}^{-3}$	89
51	Transition energy versus the barrier $\text{In}_x\text{Ga}_{1-x}\text{N}$ mole fraction for different quantum well widths.	90
52	TE optical gain as a function of wavelength for (a) varying indium well mole fraction, (b) varying indium barrier mole fraction, (c) varying well width, and (d) varying barrier width. The charge density is $N = 3 \times 10^{19} \text{ cm}^{-3}$	92
53	TE optical gain as a function of wavelength for combination of indium well mole fraction and well width. The charge density is $N = 3 \times 10^{19} \text{ cm}^{-3}$. The barrier material is GaN and $L_b = 12.4 \text{ nm}$	92
54	TE optical gain as a function of wavelength. The charge density is $N = 3 \times 10^{19} \text{ cm}^{-3}$. (a) $L_w=2.62 \text{ nm}$, $L_b=14.4 \text{ nm}$ $\text{In}_{0.32}\text{Ga}_{0.68}\text{N}/\text{GaN}$, (b) $L_w=2.9 \text{ nm}$, $L_b=14.4 \text{ nm}$ $\text{In}_{0.32}\text{Ga}_{0.68}\text{N}/\text{In}_{0.04}\text{Ga}_{0.96}\text{N}$, (c) $L_w=2.9 \text{ nm}$, $L_b=12.4 \text{ nm}$ $\text{In}_{0.31}\text{Ga}_{0.69}\text{N}/\text{GaN}$, (d) $L_w=3.14 \text{ nm}$, $L_b=12.4 \text{ nm}$ $\text{In}_{0.3}\text{Ga}_{0.7}\text{N}/\text{GaN}$, (e) $L_w=3.42 \text{ nm}$, $L_b=12.4 \text{ nm}$ $\text{In}_{0.29}\text{Ga}_{0.71}\text{N}/\text{GaN}$, (f) $L_w=3.65 \text{ nm}$, $L_b=12.4 \text{ nm}$ $\text{In}_{0.29}\text{Ga}_{0.71}\text{N}/\text{In}_{0.02}\text{Ga}_{0.98}\text{N}$, and (g) $L_w=3.72 \text{ nm}$, $L_b=12.4 \text{ nm}$ $\text{In}_{0.28}\text{Ga}_{0.72}\text{N}/\text{GaN}$. Inset: Optical gain as a function of wavelength. The charge density is $N = 3 \times 10^{19} \text{ cm}^{-3}$. Solid curve: $L_w=2.7 \text{ nm}$, $L_b=14.4 \text{ nm}$ $\text{In}_{0.32}\text{Ga}_{0.68}\text{N}/\text{In}_{0.04}\text{Ga}_{0.96}\text{N}$, Dashed curve: $L_w=2.9 \text{ nm}$, $L_b=14.4 \text{ nm}$ $\text{In}_{0.32}\text{Ga}_{0.68}\text{N}/\text{In}_{0.06}\text{Ga}_{0.94}\text{N}$, Dotted curve: $L_w=2.9 \text{ nm}$, $L_b=14.4 \text{ nm}$, $\text{In}_{0.3}\text{Ga}_{0.7}\text{N}/\text{In}_{0.04}\text{Ga}_{0.96}\text{N}$, Dotted-dashed curve: $L_w=2.9 \text{ nm}$, $L_b=14.4 \text{ nm}$, $\text{In}_{0.32}\text{Ga}_{0.68}\text{N}/\text{In}_{0.08}\text{Ga}_{0.92}\text{N}$	93
55	TE optical gain contours at a wavelength of 525 nm as a function of well and barrier mole fraction. The charge density is $N = 3 \times 10^{19} \text{ cm}^{-3}$. The well and barrier widths are $L_w = 2.9 \text{ nm}$ and $L_b = 14.4 \text{ nm}$	95

56	(a) in-plane component of strain as a function of barrier mole fraction. (b) Polarization-induced built-in electric field in the barrier regions as a function of barrier mole fraction. The well indium mole fraction is 30% and $L_w = 2.9$ nm and $L_b = 13.4$ nm.	96
57	Transition energy versus the barrier $\text{In}_x\text{Ga}_{1-x}\text{N}$ mole fraction for a 2.9 nm $\text{In}_{0.3}\text{Ga}_{0.7}\text{N}$ SQW with strained and unstrained barriers.	97
58	Transition energy versus well width in $\text{In}_{0.3}\text{Ga}_{0.7}\text{N}/\text{In}_{0.06}\text{Ga}_{0.94}\text{N}$ SQW with strained and unstrained barriers. The barriers are 13.4 nm wide.	97
59	TE optical gain as a function of wavelength. The charge density is $N = 3 \times 10^{19} \text{ cm}^{-3}$. (a) $L_w=2.9\text{nm}$, $L_b=14\text{nm}$ $\text{In}_{0.32}\text{Ga}_{0.68}\text{N}/\text{In}_{0.07}\text{Ga}_{0.93}\text{N}$, (b) $L_w=2.9\text{nm}$, $L_b=14.4\text{nm}$ $\text{In}_{0.31}\text{Ga}_{0.69}\text{N}/\text{In}_{0.01}\text{Ga}_{0.99}\text{N}$, (c) $L_w=3.14\text{nm}$, $L_b=14.4\text{nm}$ $\text{In}_{0.3}\text{Ga}_{0.7}\text{N}/\text{In}_{0.01}\text{Ga}_{0.99}\text{N}$, (d) $L_w=3.4\text{nm}$, $L_b=15.2\text{nm}$ $\text{In}_{0.29}\text{Ga}_{0.71}\text{N}/\text{In}_{0.01}\text{Ga}_{0.99}\text{N}$, and (e) $L_w=3.7\text{nm}$, $L_b=15.2\text{nm}$ $\text{In}_{0.28}\text{Ga}_{0.72}\text{N}/\text{In}_{0.01}\text{Ga}_{0.99}\text{N}$ Inset: Optical gain as a function of wave- length. The charge density is $N = 3 \times 10^{19} \text{ cm}^{-3}$. Solid curve: $L_w=2.7\text{nm}$, $L_b=14\text{nm}$ $\text{In}_{0.32}\text{Ga}_{0.68}\text{N}/\text{In}_{0.07}\text{Ga}_{0.93}\text{N}$, Dashed curve: $L_w=2.9\text{nm}$, $L_b=14$ nm $\text{In}_{0.32}\text{Ga}_{0.68}\text{N}/\text{In}_{0.09}\text{Ga}_{0.91}\text{N}$, Dotted curve: $L_w=2.9\text{nm}$, $L_w=14\text{nm}$, $\text{In}_{0.3}\text{Ga}_{0.7}\text{N}/\text{In}_{0.07}\text{Ga}_{0.93}\text{N}$, Dotted-dashed curve: $L_w=2.9\text{nm}$, $L_b=14\text{nm}$, $\text{In}_{0.32}\text{Ga}_{0.68}\text{N}/\text{In}_{0.11}\text{Ga}_{0.89}\text{N}$	98
60	Contours of the TE optical gain at 525 nm as a function of well and barrier mole fraction. The charge density is $N = 3 \times 10^{19} \text{ cm}^{-3}$. The well and barrier widths are $L_w = 2.9$ nm and $L_b = 14$ nm.	99
61	TE optical gain as a function of wavelength in a 2.9 nm $\text{In}_{0.32}\text{Ga}_{0.68}\text{N}/$ $\text{In}_{0.04}\text{Ga}_{0.96}\text{N}$ SQW. The barriers are 14.4 nm wide. The charge density is $N = 3 \times 10^{19} \text{ cm}^{-3}$	99
62	Schematic view of an $\text{AlGaIn}/\text{GaIn}$ MOSHFET.	102

SUMMARY

The effect of hot phonons and the influence of macroscopic polarization-induced built-in fields on the performance of III-V nitride devices are investigated. Self-heating due to hot phonons is analyzed in AlGaIn/GaN high electron mobility transistors (HEMTs), and the effect of macroscopic polarization charges on the operation of blue and green InGaIn-based quantum well lasers is presented.

AlGaIn/GaN HEMTs are extensively used in high power applications. Under typical operating conditions, highly energetic electrons internal to the device lose their excess energy primarily through the emission of dispersionless longitudinal optical (LO) phonons, which eventually decay into acoustic phonons. Acoustic phonons transport the thermal energy primarily toward the substrate. This thermal transport by acoustic phonons in the diffusive limit is modeled using a two-dimensional lattice heat equation.

InGaIn-based devices are in great demand for blue and green lasers. To characterize these laser structures, the two-dimensional quantum well laser simulator MINILASE is extended to include nitride bandstructure and material models. A six-band **k.p** theory for strained wurtzite materials is used to compute the valence subbands. Spontaneous and piezoelectric polarization charges at the interfaces are included in the calculations, and their effects on the device performance are described. Additionally, **k.p** Hamiltonian for crystal growth directions that minimize the polarization-induced built-in fields are modeled, and valence band dispersions for the non-polar planes are calculated.

Finally, a design parameter subspace is explored to suggest epitaxial layer structures which maximize gain spectral density at a target wavelength for green $\text{In}_x\text{Ga}_{1-x}\text{N}$ -based single quantum well active regions. The dependence of the fundamental optical transition energy on the thickness and composition of barriers and wells is discussed, and the sensitivity of gain spectral density to design parameters, including the choice of buffer layer material, is investigated.

CHAPTER I

INTRODUCTION

1.1 Motivation and objective

The motivation for this research stems from the ever increasing consumer and military demand for better and faster electronics, and is driven by the development of evolving technologies to meet these demands. Comprehensive device simulation tools capable of accurately predicting the electrical, thermal, and optical behavior are key to the successful design and fabrication of next generation devices. This research aims to develop predictive numerical simulation tools for nitride-based wide bandgap material devices. Using advanced modeling and simulation techniques, the micro- and nano-scale operation of GaN-based transistors and lasers is investigated, and various optimized design strategies are explored.

1.2 Organization of the thesis

The remainder of chapter I presents an overview of the history of nitride-based devices and their applications to microelectronics and optoelectronics. Chapter II reviews salient material properties of nitrides like crystal structure, phonon dispersion, and spontaneous and piezoelectric polarization charge. Steady-state electro-thermal simulation of GaN-based high frequency transistors is detailed in chapter III. Chapter IV introduces the two-dimensional quantum well laser simulator MINILASE, followed by a discussion of the implementation of nitride bandstructure and material models. Details of InGaN-based quantum well simulations are presented in chapter V. In chapter VI, nitride-based laser diodes along non-(0001) growth planes are described, and the implementation of arbitrary crystal orientation into the simulator is elaborated upon

in this chapter. Chapter VII explores design strategies to maximize the gain spectral density at a target wavelength for InGaN-based green lasers. Finally, the thesis concludes with chapter VIII, which details future applications of the research conducted in this thesis.

1.3 Nitrides in electronics

Historically, silicon devices such as diodes, thyristors, bipolar junction transistors (BJTs), insulated-gate bipolar transistors (IGBTs), and metal-oxide-semiconductor field effect transistors (MOSFETs) have ruled the power semiconductor industry, catering to both high power electronics as well as systems applications [60]. Devices made with Si are considered “medium power” devices [78], and have numerous disadvantages for high power applications such as a small energy gap, frequency switching limitations [60], and a maximum operating temperature of 180 °C for Si-based chips [78]. At high operating temperatures, Si BJTs suffer from thermal runaway, while Si MOSFETs and complimentary MOS circuits have leakage currents and latch up issues [211]. In such situations, GaAs-based transistors could outperform Si-based transistors, but GaAs transistor applications are limited to operating frequencies near 3 GHz at room temperature and suffer from intrinsically poor thermal conductivity.

Wide bandgap materials like SiC and GaN provide an alternative to Si and GaAs at high power, high temperature, and high frequency operation, mainly because of their wider bandgap, high breakdown field and saturated drift velocity, and higher thermal conductivity of SiC. One fundamental cause of breakdown in devices operating at high voltages is impact ionization, wherein, under the influence of an applied electric field, free electrons traveling with sufficient kinetic energy can cause transitions of bound electrons from the valence band to the conduction band, generating additional electron-hole pairs. With a wider energy gap, a higher magnitude of electric field would be required to initiate an impact ionization event. High breakdown

fields also make it possible to design devices with thinner layers. Higher saturated drift velocities allow for higher current drive, and large thermal conductivities translate into more efficient heat dissipation in the devices. Table 1 compares electrical and thermal parameters for Si, GaAs, SiC, and GaN.

Although SiC and GaN are competing material technologies for device applications, GaN has an edge over SiC. GaN and its alloys are direct bandgap materials making them very attractive for optoelectronic applications. Additionally and most significantly, with binary nitrides and their alloys it is possible to fabricate quantum well heterostructures and modulation doped structures [152].

Among GaN-based devices that are most prevalent are high electron mobility transistors (HEMTs), BJTs, heterostructure bipolar transistors (HBTs), MOSFETs, Schottky and p-i-n rectifiers. Switching power supplies made from GaN are still in their early stages of development [152]. GaN HEMTs find use in cell phones and wireless base stations, military applications, satellite and radar communications, microwave rectifiers, and microwave ovens as depicted in Figure 1 [123, 88, 46]. Many additional microwave power applications exploit GaN-based HBTs and BJTs [152].

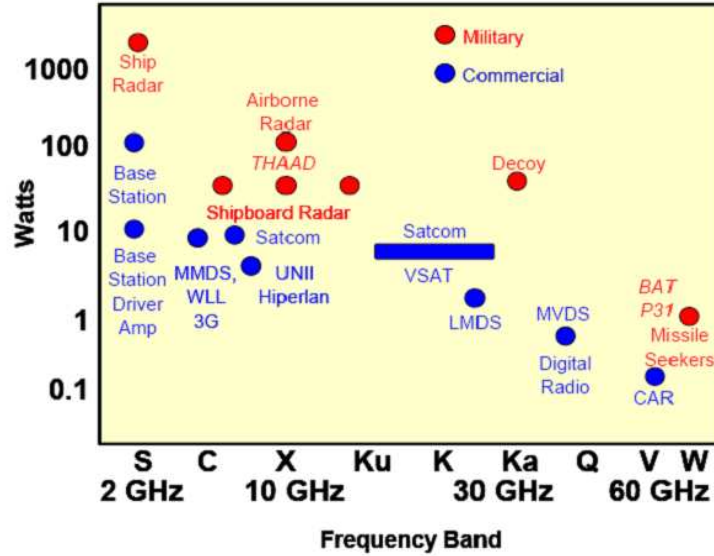


Figure 1: Current and future applications of GaN-based transistors [121].

Table 1: Electrical properties of Si, GaAs, 4H-SiC and GaN [210, 36, 193, 60, 57, 40, 46].

Electrical Property	Si	GaAs	4H-SiC	GaN
Bandgap (eV)	1.12	1.43	3.2	3.47
Breakdown field (MV cm ⁻¹)	0.3	0.4	3	3
Electron mobility (cm ² V ⁻¹ s ⁻¹)	1350	8500	800	900
Saturated electron velocity (x10 ⁷ cm s ⁻¹)	1	1.2	2	2.5
Thermal conductivity (W cm ⁻¹ K ⁻¹)	1.5	0.5	4.5	1.3
Dielectric constant	11.8	12.8	9.7	9

The concept of a HEMT was proposed in 1979 [2], and in 1980 the first GaAs-n-Al_xGa_{1-x}As HEMT with high-speed microwave capabilities was demonstrated by Fujitsu Laboratories [118]. Subsequently, digital integrated HEMT circuits with high switching speeds [119], and cryogenic low noise HEMT amplifiers for radio telescopes were realized [187] and low noise HEMT amplifiers were mass produced with the potential for microwave and millimeter wave applications.

The operation of the first AlGaIn/GaN HEMT was demonstrated by Khan *et al.* in 1994 [91]. The device, with a 0.25 μm gate length, was limited to a maximum current density of 60 mA/mm and a transconductance of 27 mS/mm, but demonstrated potential for microwave and millimeter wave applications. Operation at 1.1 W/mm power density and 2 GHz frequency was reported for the first time for an AlGaIn/GaN HEMT on sapphire by Wu *et al.* two years later [215]. With improvement in device structures and fabrication techniques, the reported power density increased to 1.5-1.7 W/mm at 4-10 GHz [7, 221, 217]. High Al-content barriers proved to be the key to even higher power density demonstrated at 2.84 W/mm and 8 GHz [219], and 3.1 W/mm at 18 GHz [220]. Better gate recessing techniques resulted in a power density of 4.6 W/mm at 6 GHz for a GaN HEMT on sapphire substrates [218]. When the substrate material was changed from sapphire to SiC, the power density improved to 6.9 W/mm at 10 GHz [178].

The current generation of AlGaIn/GaN HEMTs have an output power of more than 32 W/mm, 7.8 W/mm, and 10.5 W/mm at 4 GHz [222], 15 GHz [141], and 40 GHz [142] respectively. Theoretically calculated values of electron mobility in AlGaIn/GaN HEMTs lie around $1602 \text{ cm}^2/\text{V-s}$ at $T = 300 \text{ K}$ [228], which is close to the measured value of $2019 \text{ cm}^2/\text{V-s}$ [69], and measured and calculated carrier concentrations are in the range of $0.7\text{-}1.4 \times 10^{13} \text{ cm}^{-2}$ [41, 68, 228]. Simulated and measured values of the saturation velocity in bulk GaN and AlGaIn/GaN heterostructures are $3.1 \times 10^7 \text{ cm/s}$ [185, 21, 229]. Peak electron velocity is $2.1 \times 10^7 \text{ cm/s}$, and the breakdown electric field is 3 MV/cm , which is higher than the breakdown field in conventional Si and GaAs based devices [57].

A schematic of an AlGaIn/GaN HEMT is shown in Figure 2a. It consists of a thin unintentionally doped narrow bandgap region (GaN) bounded by a doped barrier region of wider bandgap (AlGaIn). Such a structure is also called modulation-doped field effect transistor (MODFET) [118]. With the application of a gate bias, electrons from the doped barrier diffuse into the GaN and get trapped there, forming a thin conducting channel. They are prevented from reentering the AlGaIn region because of the potential barrier that exists at the channel/barrier interface (Figure 2b). The trapped electrons in the triangular-shaped potential energy region form a two-dimensional electron gas (2DEG), and travel under the influence of an applied drain bias along the channel/barrier interface between source and drain. The mobile carriers in the GaN channel are spatially separated from the dopant atoms in the AlGaIn barrier region. As a result, the frequency of scattering with the ionized dopants is considerably reduced. These devices tend to have higher carrier mobilities than conventional transistors, hence the name “high electron mobility transistor”. Sometimes a thin wide bandgap spacer layer such as AlN is inserted between the barrier and channel regions to provide further separation between the charge carriers and dopant atoms.

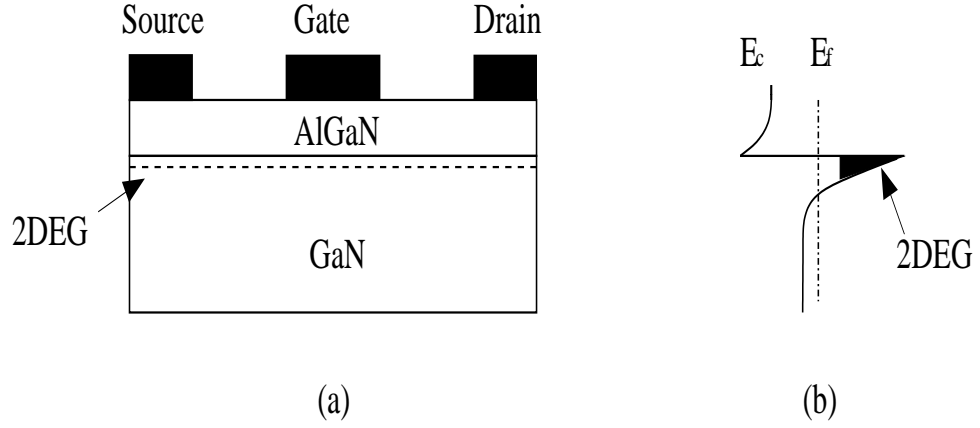


Figure 2: (a) Schematic of an AlGaN/GaN HEMT structure, (b) Conduction band diagram showing the two dimensional electron gas (2DEG).

1.4 Nitrides in optoelectronics

The bandgaps of III-nitrides (0.608-6.0 eV for InN-AlN [154]) and their alloys span a wide spectrum of energies, from infrared to deep ultraviolet as shown in Figure 3. Such a range would not be possible with any of the other III-V compound semiconductor systems and this opens up diverse avenues for a wide range of nitride-based optoelectronic applications including blue and green light emitting diodes (LEDs), ultraviolet, blue and green laser diodes (LDs), ultraviolet photodetectors, and electro-absorption and Mach-Zehnder modulators [55, 128, 129, 53, 197, 87].

Demand for high efficiency light sources, full color displays, and indicators with high reliability have led researchers to explore novel and exotic material systems. The color displays require red, blue, and green color elements such as LEDs to reproduce the full color spectrum. Nitride-based blue and green LEDs complete the color spectrum, with immediate applications like color displays and traffic signals. Touted as the “ultimate lamp” [86, 47], LEDs are rapidly replacing conventional light sources such as light bulbs and fluorescent bulbs because of their higher luminescence efficiency and longer lifetimes [128]. Additionally, the red, blue, and green colors can be combined to produce white LEDs for long lasting and efficient illumination. Other

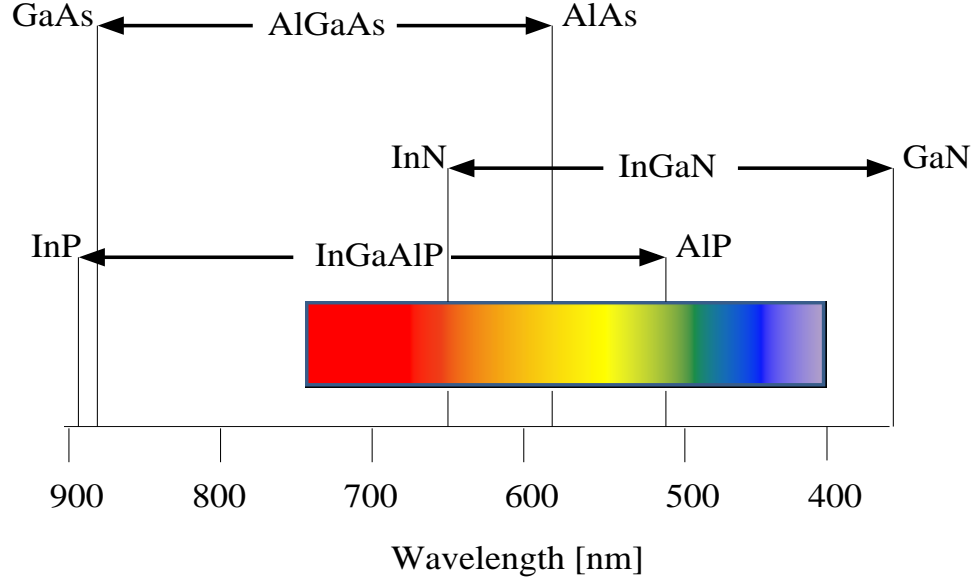


Figure 3: Ternary and quaternary materials used for optoelectronics along with the wavelengths [152].

applications include sensors, indicator lamps for instrumentation, and automobile instrument panel illumination.

GaN-based UV photodetectors are increasingly being used for defense and space applications like missile plume detection systems, solar UV monitoring and detection, flame sensors, UV source calibration, and secure space communication [55]. Electro-absorption modulators are used in optical interconnects, Q switching and low chirp modulation of LDs [87].

LDs have also gained importance in commercial applications like communication systems, optical readout sources and optical printing, sensors, and various medical equipment that require cheap coherent lasers with moderate power over short wavelengths. The most prevalent forms of optical storage devices today are CDs and DVDs. CDs typically use 780 nm AlGaAs laser diodes with a storage capacity of 650 MB. On the other hand, 650 nm AlGaInP lasers are used for DVDs, which provide a storage of up to 9.4 GB. Diode lasers made of II-VI material like ZnSe and its alloys emit light at 490 nm, but have several drawbacks [79, 169], mainly, short

lifetimes, low thermal conductivity, and low thermal stability. With the availability of 405 nm violet InGaN LDs, blue-ray discs with storage capacities of 50 GB have now been realized. The use of smaller wavelength nitride lasers in optical storage and readout sources offers reduced focal diameters, since the storage capacity increases quadratically with optical frequency. This can give rise to higher recording densities [55, 122, 19].

The evolution of semiconductor lasers started in 1953 when von Neumann first suggested the possibility for light emission in a semiconductor via stimulated emission [20]. In 1962, four groups reported light emission from GaAs p-n junction diodes [80, 133, 85, 160]. These structures were homojunction lasers. In addition to lasing in GaAs, many groups also reported lasing in InAs and $\text{Ga}_x\text{In}_{1-x}\text{As}$ [117], InP [209], and $\text{InP}_x\text{As}_{1-x}$ [8]. However, these homojunction lasers needed very high lasing threshold current densities ($> 50,000 \text{ A/cm}^2$) at room temperature. To circumvent this problem, Kroemer in 1963 suggested the use of a heterostructure, which constituted a material of narrow bandgap sandwiched between two layers of wider bandgap [102]. Following this, several groups demonstrated the operation of GaAs-AlGaAs single [101, 82] and double heterostructures [143, 56].

Stimulated emission from optically pumped GaN was first observed by Dingle *et al.* in 1971 [51]. Although there were other optically pumped stimulated emission observations from GaN films [9, 231], InGaN films [93, 97], AlGaIn/InGaN double heterostructures [12], and GaN/AlGaIn double heterostructures [3, 172], it was Nakamura *et al.* [131] who fabricated the first current-injected nitride-based laser diode. The active region of this laser consisted of an InGaN-based multiple quantum well (MQW) that emitted coherent light at 417 nm under pulsed current injection at room temperature, with a threshold current density of 4 kA/cm^2 . Nakamura also successfully demonstrated the continuous-wave (cw) operation of an InGaN MQW LD at 233 K, which had a threshold current density of 8.7 kA/cm^2 [130].

To understand the basic operation of a semiconductor laser diode, consider the schematic shown in Figure 4. It consists of an active region made up of alternating layers of wide and narrow gap materials called barrier and well, respectively. The active region is sandwiched between “light-guiding” waveguide layers followed by n- and p- cladding (lower refractive index) layers. When a forward bias voltage is applied to the electrodes of this device, electrons from the n-side and holes from the p-side are injected into the “potential energy well” of the active region, where they recombine spontaneously to produce light. During this process, the waveguide layers help to confine the light generated in the active region, mainly because of the difference in the refractive indices of the cladding and the waveguide layers. Such a structure is called separate confinement heterostructure (SCH), because the light is generated within the active region and confined by the waveguides. The active region along with the waveguiding layers forms the laser cavity. The generated light propagates along the active region, parallel to the waveguides, and is reflected back and forth by the mirrors that are present at either ends of the laser cavity. The reflected light initiates stimulated emission of photons due to the recombination of electrons and holes, which further increases the photon population in the optical cavity and gives rise to increased stimulated emission. At a threshold current, strong stimulated emission occurs in the laser cavity and the structure acts as a laser diode.

This thesis addresses two issues that are critical to the operation of nitride-based devices:

1. Self-heating due to hot phonon effects in AlGa_N/Ga_N HEMTs that operate at high temperatures, and
2. Presence of macroscopic built-in polarization fields in blue and green InGa_N/Ga_N quantum well lasers.

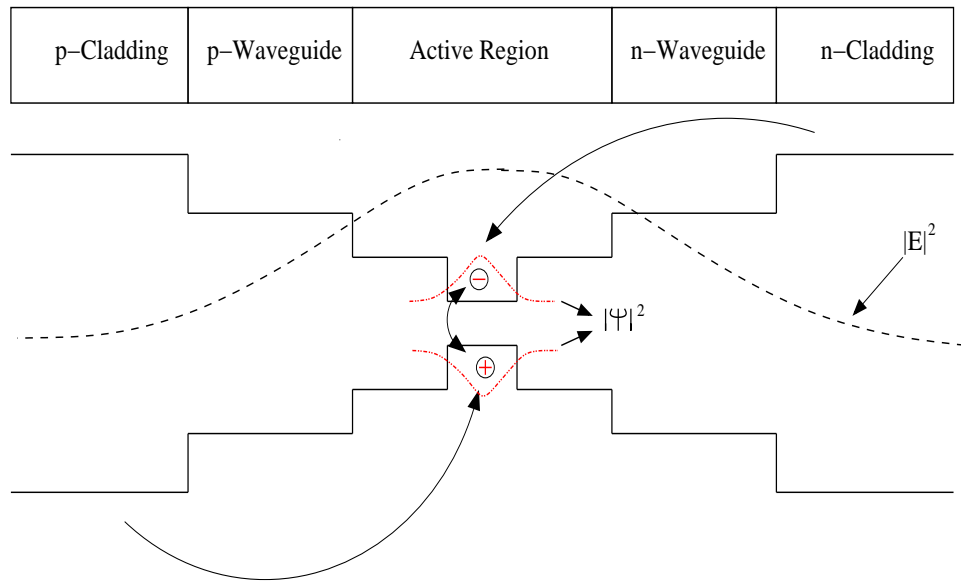


Figure 4: Schematic of a semiconductor single quantum well heterostructure.

CHAPTER II

OVERVIEW OF III-NITRIDES

2.1 Basic material properties

Group III-nitrides occur in three crystal structures, namely, wurtzite, zincblende, and rocksalt. The thermodynamically stable state for bulk AlN, GaN, and InN is the wurtzite structure (α -GaN). The Bravais lattice of the wurtzite structure shown in Figure 5 is a hexagon with a space group of C_{6v}^4 ($P6_3mc$). Wurtzite crystals have a basis of four atoms in each hexagonal unit cell. The unit cell is described by its base length ‘a’ and height ‘c’. It is also characterized by a dimensionless internal cell parameter known as ‘u’, which is the cation-anion bond length parallel to the c-axis [0001]. The hexagonal crystal structure may be visualized as two intertwining hexagonal closed packed (HCP) sublattices. Each sublattice has one type of atom offset along the c-axis by 5/8 of the cell height i.e., 5/8c. The bandgap of the wurtzite III-nitrides increases from InN to AlN, while the lattice constants increase from AlN to InN. Table 2 shows the typical lattice constants and the bandgap energies of the binaries InN, GaN, and AlN. Because of the lattice mismatch between different layers of heteroepitaxial material in the wurtzite III-nitrides, there is inherent strain present in devices with heterojunctions. The induced strain can influence the optical and electrical properties of the devices.

Although GaN-based devices hold a promising future, material growth had been problematic for two main reasons, namely,

1. There have been no suitable substrate materials available that could be lattice matched to GaN. Sapphire and SiC, the most commonly used substrate materials, have a lattice mismatch of 13.8% [151] and 3.5% [109], respectively, with

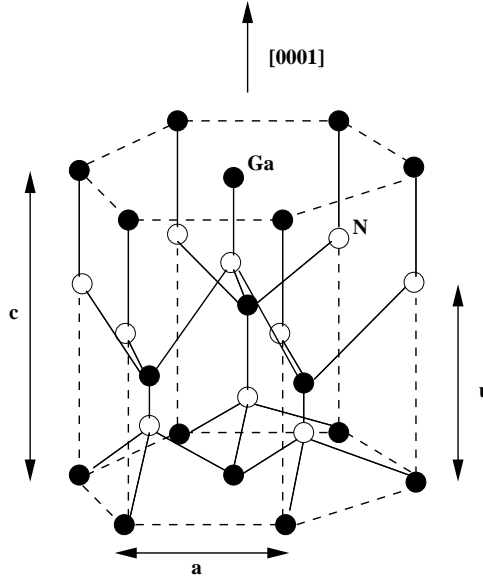


Figure 5: Wurtzite crystal structure formed by two intertwined hexagonal sublattices [155].

Table 2: Lattice constants and bandgap energy of InN, GaN, and AlN [154].

Parameters	InN	GaN	AlN
a (Å)	3.545	3.189	3.112
c (Å)	5.703	5.185	4.982
E_g (eV) at 300K	0.608	3.437	6.00

GaN. Growth of GaN on these substrates has resulted in numerous dislocations. This problem has been partially resolved by growing high-quality GaN films on sapphire substrates using the metalorganic chemical vapor deposition (MOCVD) technique with AlN [11, 6] and GaN [125] nucleation layers.

2. It has been difficult to grow p-doped materials due to both the high n-type background concentration as well as the deep ionization levels of common acceptors. Improvements have been possible using low-energy electron-beam irradiation (LEEBI) of Mg-doped GaN to obtain p-type GaN [10], and also by thermal annealing in an N_2 ambient [127]. More recently, reliable Mg-doped GaN films

have been grown using plasma assisted molecular beam epitaxy (PAMBE) techniques [37], and doping concentrations as high as $8 \times 10^{20} \text{ cm}^{-3}$ using MOCVD with a measured mobility of $62 \text{ cm}^2/\text{V-s}$ [100], and $3.5 \times 10^{20} \text{ cm}^{-3}$ using MBE [132] techniques have been reported. Additional information about the electrically active fraction of these dopants has not been reported.

2.2 Phonons in GaN

Electrical and optical properties of semiconductor devices may be significantly affected by carrier-phonon interactions. For electronic devices like high speed transistors, carrier-phonon interactions may scatter carriers from one energy level to another, leading to reduced mobilities. In optoelectronic devices, lattice phonons may participate in near-bandgap emission and absorption processes, which may cause enhanced absorption near the fundamental bandgap and broadening of the emission spectrum [74].

The total number of vibrational phonon modes in any crystal is dependent on the number of atoms per unit cell. For a crystal with 'n' atoms per unit cell, there are $3n$ phonon modes. Of these $3n$ modes, 3 are acoustic and $3n-3$ are optical modes. Wurtzite GaN has four atoms per unit cell, and hence, there are 12 phonon modes with 3 acoustic (one longitudinal acoustic (LA) and two transverse acoustic (TA)) and 9 optical modes in the long-wavelength limit. In a 3D crystal, the ratio of the transverse optical (TO) modes to the longitudinal optical (LO) modes is always two. The phonon dispersion curves for bulk wurtzite GaN is shown in Figure 6 [35]. In the dispersion plot, the curves that have zero frequency (energy) at $\mathbf{k}=0$ are the acoustic phonon branches, while the high frequency branches are the optical phonons. For propagation along the c-axis, $1A_1(\text{LA})$ and $2E_1(\text{TA})$ are the acoustic modes and $1A_1(\text{LO})$, $2E_1(\text{TO})$, $1B_1(\text{low})$, $1B_1(\text{high})$, $2E_2(\text{low})$, and $2E_2(\text{high})$ are the optical modes. Near the Γ point, only 8 modes are visible instead of 12, because all the

transverse modes are degenerate. Of these different modes, one A_1 and one E_1 modes are both Raman and infrared active, two E_2 modes are only Raman active and the B_1 modes are silent modes, which means that these modes can be detected by neither first-order Raman nor infrared spectroscopy [38].

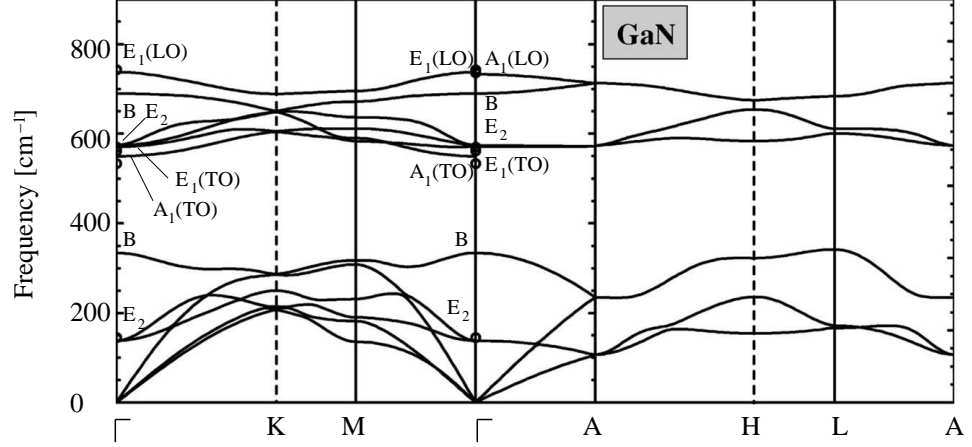


Figure 6: Phonon dispersion of bulk GaN showing the different phonon branches [35]

2.3 Spontaneous and piezoelectric polarization charges

An important property of III-V nitride materials is the presence of macroscopic polarization. Macroscopic polarization was previously known to exist only in low-symmetry ferroelectric crystals [135]. However, its existence in III-V wurtzite nitrides has been confirmed by both first-principles calculations and experiments [29, 13, 75]. Polarization charges in III-nitrides are made up of two components, namely, spontaneous and piezoelectric polarization.

The ionicity associated with the cation-anion bonds in wurtzite nitrides gives rise to significant spontaneous polarization charges in these materials. The polarity of spontaneous polarization depends on the direction of the bonds in the crystal, parallel to the c -axis. The typical pseudomorphic growth direction for III-V wurtzite nitrides is either in the $[0001]$ (Ga-face polarity) or the $[000\bar{1}]$ (N-face polarity) direction as shown in Figure 7 [15]. In the Ga-face polarity, the Ga atom is at the top position of

the $\{0001\}$ bilayer and the direction of the bonds is from cation Ga atom to anion N atom. On the other hand, in the N-face polarity, the N atom is at the top position of the $\{000\bar{1}\}$ bilayer, and here, the bonds are from anion N atom to cation Ga atom. Designating the positive direction to be pointing from the cation to the anion atom, i.e., Ga to N atom ($[0001]$ growth direction), spontaneous polarization is negative for Ga-face heterostructures and positive for N-face heterostructures. In such cases, the spontaneous polarization-induced electric field will also be in the growth direction. Figure 8 shows the orientation of these charges for AlGaN/GaN and InGaN/GaN heterostructures.

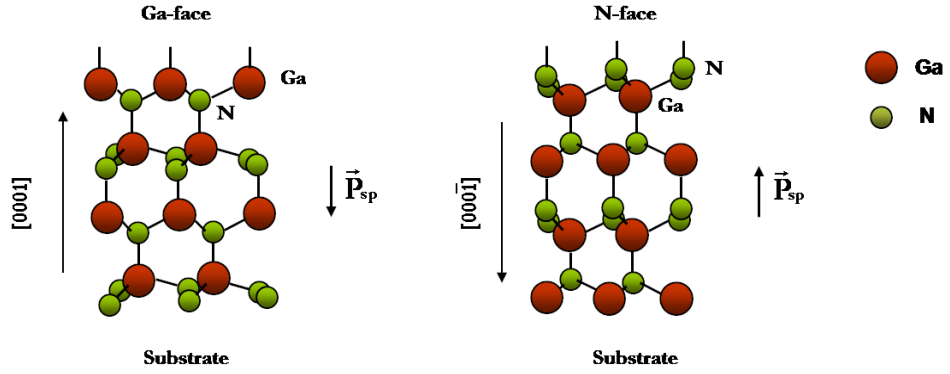


Figure 7: Crystal orientation of Ga- and N-face GaN [15].

When layers of III-V nitrides are pseudomorphically grown, they are under strain because of the inherent lattice mismatch between the layers. The strain is tensile for $\text{Al}_x\text{Ga}_{1-x}\text{N}$ and $\text{Al}_x\text{In}_{1-x}\text{N}$ (for $x > 0.82$) and compressive for $\text{In}_x\text{Ga}_{1-x}\text{N}$ and $\text{Al}_x\text{In}_{1-x}\text{N}$ (for $x \leq 0.82$) layers grown on top of thick relaxed GaN buffer layers. As a result, these strained layers give rise to piezoelectric polarization charges at material interfaces. Piezoelectric polarization is positive for compressive strains and negative for tensile strain and is also oriented parallel to the growth axis, i.e., c-axis. Positive value of piezoelectric polarization means that the direction of the polarization is pointing away from the substrate.

In Figure 8, spontaneous polarization in G-face heterostructures is oriented toward

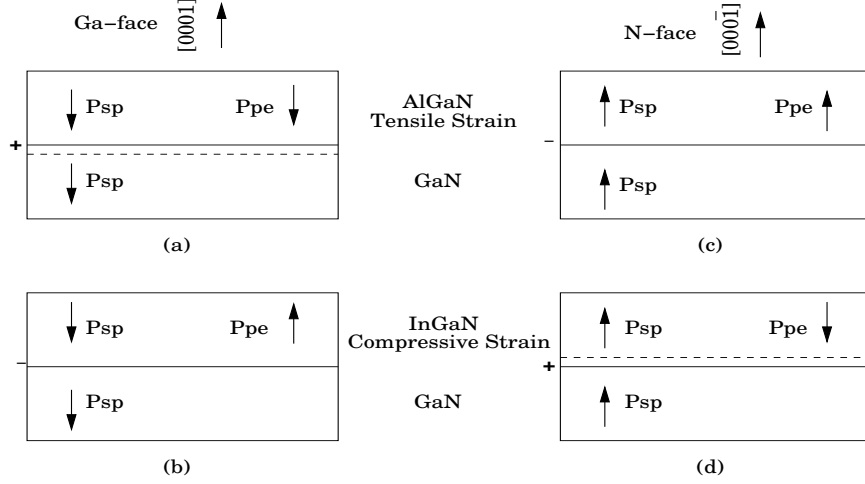


Figure 8: Orientation of spontaneous and piezoelectric polarization charges in Ga-face ((a) and (b)) and N-face ((c) and (d)) AlGaN/GaN and InGaN/GaN heterostructures. In Ga-face AlGaN/GaN and N-face InGaN/GaN heterostructures, the net polarization-induced sheet charge density at the interface is positive, giving rise to a 2DEG in the smaller bandgap GaN and InGaN layers respectively [15, 14].

the substrate, while in N-face it is oriented away from the substrate. Also, in Ga-face AlGaN/GaN and N-face InGaN/GaN systems, the net polarization-induced charge density at the interface is positive, giving rise to a 2DEG in the lower bandgap GaN and InGaN materials respectively, as shown in Figure 8 (a) and (d).

The magnitudes of piezoelectric constants in III-nitrides is about ten times higher than other III-V or II-VI compounds. In addition to this, the spontaneous polarization in nitrides, in the absence of strain, is the highest [29]. The values of spontaneous polarization in binary GaN and InN are close, and hence, the net spontaneous polarization charge at the interface of an $\text{In}_x\text{Ga}_{1-x}\text{N}/\text{GaN}$ system is negligible. However, there is a significant lattice mismatch between GaN and InN layers, and as a result, polarization charge at $\text{In}_x\text{Ga}_{1-x}\text{N}/\text{GaN}$ interface is mainly piezoelectric in nature. On the other hand, the lattice mismatch between AlN and GaN is much smaller. AlN has the highest spontaneous polarization among the nitrides, and its value is only about a few orders of magnitude smaller than the ferroelectric perovskites [13, 28].

Hence $\text{Al}_x\text{Ga}_{1-x}\text{N}/\text{GaN}$ heterostructures have predominantly spontaneous polarization charge at the interfaces.

Under the influence of both spontaneous and piezoelectric polarization charges, quantum confined Stark effect (QCSE) has been observed in $\text{AlGaIn}/\text{GaInN}$ [95, 107, 192] and $\text{InGaIn}/\text{GaInN}$ [190, 191] quantum well structures. The net polarization charge at each heterointerface is known to induce large ($\approx\text{MV}/\text{cm}$) built-in fields in nitrides [27] that depend on the strain, piezoelectric constants, device geometry i.e., the number of quantum wells, thickness of each well, and material composition, boundary conditions, and even temperature. These fields may give rise to 2DEGs with sheet carrier concentrations in excess of 10^{13} cm^{-2} [15]. These sheet charge densities in wurtzite nitrides are much higher than reported in any other III-V material system. This property of nitrides is particularly useful in the operation of $\text{AlGaIn}/\text{GaInN}$ HEMTs, where 2DEGs with high sheet carrier concentrations can be achieved at the interface without any intentional doping in the device. This phenomenon is, however, deleterious to some aspects of optoelectronic device operation. The impact of these polarization charges on device performance is discussed in subsequent chapters of this thesis.

CHAPTER III

ELECTROTHERMAL SIMULATION OF ALGaN/GaN HIGH ELECTRON MOBILITY TRANSISTORS

3.1 Hot phonon effect in AlGaN/GaN HEMTs

Due to their various applications in power electronics, AlGaN/GaN HEMTs usually operate at high temperature [55]. Under typical operating conditions, large bias voltages accelerate channel electrons to energies high above the band edge. In energetic distributions far from equilibrium, electrons transfer a large amount of energy to the lattice, predominantly through the emission of long wavelength LO phonons via the Fröhlich interaction [177]. These generated phonons are eventually either reabsorbed by the electrons, or decay into lower order optical and acoustic phonon modes via various pathways determined by the appropriate selection rules [23, 181]. This process in turn creates a non-equilibrium phonon population, thereby giving rise to hot phonons in the channel [98]. These hot phonons may be responsible for reduced power dissipation [161] and electron velocities [224] in GaN-based devices.

The emitted LO phonons have a finite lifetime, and the lifetime may be inferred using subpicosecond time-resolved Raman spectroscopy [196, 195], with values ranging from 0.75-3 ps at 300 K for bulk GaN [195, 181, 25]. For an AlGaN/GaN heterostructure, a lifetime of 0.35 ps at 373 K has been reported using a short-time-domain gated radiometric microwave noise technique [115, 114]. Tsen *et al.* [196, 195] have deduced that the most reasonable theoretical interpretation of measured phonon decay lifetimes is that the decay path involves a three-phonon process, wherein zone-center LO phonons decay into a large wavevector TO phonon and a large wavevector LA or TA phonon, i.e., $\text{LO} \rightarrow \text{TO} + (\text{LA or TA})$, thereby conserving both energy and

momentum [164, 195]. Zone-center optical phonons generated by hot electrons are spatially localized to the immediate vicinity of their generation, owing to their negligible group velocity, leading to the formation of a local hot spot. On the other hand, zone-center acoustic phonons have a finite group velocity, and they are largely responsible for the transport of heat away from the active region of a device, mostly toward the substrate. Energy transfer and transport in GaN-based devices may therefore be visualized using the block diagram shown in Figure 9 [159].

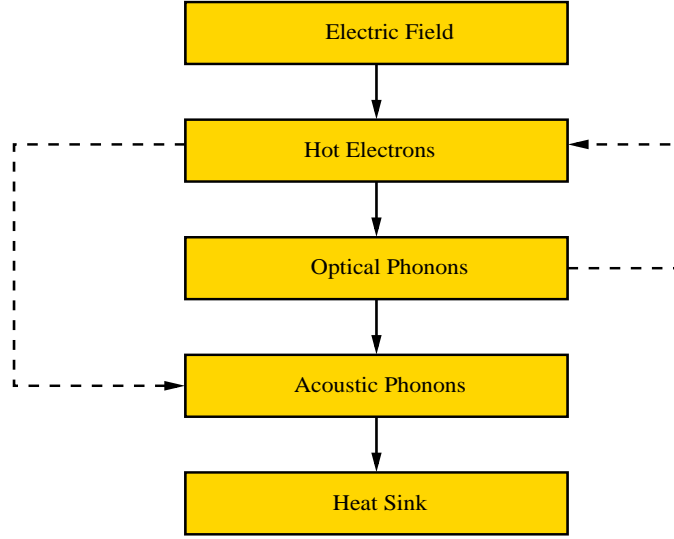


Figure 9: Block diagram of the optical and acoustic phonon generation and decay process in GaN [159].

Self-heating in HEMTs may significantly impact the current-voltage characteristics [67], and hence, accurate modeling and simulation of these thermal effects is crucial to the understanding of the operation of these devices. Self-heating is more important in GaN than GaAs. The 2DEG sheet carrier concentration in GaN (10^{13} /cm²) is an order of magnitude greater than in GaAs (2×10^{12} /cm²) [180]. Additionally, the energetic electrons in the channel emit LO phonons every 50 ± 10 fs in GaN [194] and 150-200 fs in GaAs [90, 83], while the LO phonon decay times are comparable with about 3 ps for GaN [195] and 2.1 ps for GaAs [201]. This means that for every excited electron, more LO phonons may be generated in GaN than in

GaAs per unit time.

Thermal simulations have been previously performed by Wu *et al.* to investigate self-heating effects in AlGaIn/GaN HEMTs using a dual heat source model to compute the channel temperature [215, 216]. In this model, the heat generation region is divided into two parts, 1) the active region consisting of the channel region, i.e., the gate-length plus the gate-to-drain depletion distance and, 2) the parasitic region made up of the Ohmic contact transfer length and source-to-drain spacing. The temperature rise in the HEMT device is calculated according to a heat conduction equation in each region separately, and the actual temperature is obtained by a superposition of the two solutions. The total power dissipation for the heat equation is obtained experimentally. Channel temperatures have also been calculated by other authors using a non-linear three dimensional heat spreading simulation [58]. The heat source for this simulation is assumed to be of a planar geometry.

Although the above methods may predict the channel temperature, they may fail to provide an exact location of the hot spots in the active regions of the HEMT, and subsequently the location of the peak temperature. The source term of the heat equation employed in this thesis, which is the energy loss rate as described later, implicitly contains information about the spatial distribution of non-equilibrium LO phonon population, and hence, the solution of the heat equation provides a more accurate estimation of the location of the hot spot. This also eliminates the additional power measurements, which form the source terms for the above methods.

More elaborate electrothermal simulations have been carried out by Sadi *et al.* [168] for AlGaIn/GaN HEMTs using the analytical thermal resistance matrix approach [24]. This method employs a mutual thermal resistance matrix R_{ij} that relates the power dissipated in the j^{th} region P_j to the temperature change $\Delta\theta_i$ in the i^{th} region i.e., $\Delta\theta_i = R_{ij}P_j$. However, due to the simple spherical nature of the band-structure used in these calculations, simulation accuracy is limited to low voltage

biases. Additionally, our present work assumes a non-equilibrium LO phonon population whose decay into acoustic modes in addition to the direct emission of acoustic phonons by channel electrons contributes to a rise in the acoustic phonon temperature in the active regions of the device [184].

3.2 *Formulation of the electrothermal problem*

To model the electrical and thermal behavior of AlGaIn/GaN HEMTs, an electrothermal solver has been developed, the details of which are presented in this section. The electrothermal solver has been self-consistently coupled to an ensemble Monte Carlo simulator [184]. The electric field profile within the device is obtained from the electrical solver, properly accounting for the charge distributions and boundary conditions, while the thermal solver calculates the temperature distribution within the device. The advantage of the formulation presented in this thesis is that a single discretization scheme (described in section 3.3) can be applied to both the electrical and thermal equations, thereby, considerably reducing the computational load of the simulator.

Acoustic phonons transport the majority of the thermal energy generated by hot electrons toward the substrate. In this thesis, thermal transport among acoustic modes is treated in the diffusive limit, and is modeled using a two-dimensional lattice heat equation. Optical modes are treated as dispersionless and their occupation number is modeled with a position-dependent rate equation. The defining equations are as follows:

$$\nabla \cdot [\kappa(x, y) \nabla T(x, y)] = \frac{\partial T(x, y)}{\partial t} + S(x, y) \quad (1)$$

$$\frac{N_q^n(x, y)}{dt} = -\frac{(N_q^n(x, y) - N_{eq}^n)}{\tau_n} + G^n(x, y) \quad (2)$$

where, $T(x, y)$ is the spatially varying acoustic phonon temperature, $\kappa(x, y)$ is the thermal diffusivity tensor and S is the net energy loss rate (ELR) in units of K/s and it consists of two parts, 1) the net power transferred from the optical to the acoustic

phonons, and 2) the power delivered to the acoustic phonons directly from electrons. N_q^n is the occupation number of an LO mode with index n and wavevector q , τ_n is the phonon lifetime, G^n is the net optical phonon emission rate. The equilibrium phonon population N_{eq}^n is given by the Bose-Einstein relation,

$$N_{eq}^n = \frac{1}{e^{\frac{\hbar\omega_n}{k_B T_{eq}}} - 1} \quad (3)$$

where, $\hbar\omega_n$ is the energy of the n^{th} phonon, k_B is the Boltzmann constant, and T_{eq} is the equilibrium temperature. Non-equilibrium phonon populations are then used to calculate the strength of various scattering mechanisms in the Monte Carlo simulator.

The thermal diffusivity is related to the thermal conductivity K (W/m-K) by the following relation,

$$\kappa = \frac{K}{c\rho_d} \quad (4)$$

where, c is the specific heat capacity in (J/kg-K) and ρ_d is the density in (kg/m³).

Electrical self-consistency with the Monte Carlo simulator is obtained through the solution of a two-dimensional Poisson equation on an irregular grid.

$$\nabla \cdot [\epsilon(x, y) \nabla \phi(x, y)] = -[\rho(x, y) + \rho^{pol}] \quad (5)$$

$\phi(x, y)$ is the electrostatic potential, $\rho(x, y)$ is the three-dimensional charge density in C/m³, and $\epsilon(x, y)$ is the permittivity tensor. Charges are assigned using the cloud-in-cell scheme [32, 106]. ρ^{pol} is given by,

$$\rho^{pol} = -\nabla \sigma \quad (6)$$

where, σ is the polarization-induced sheet charge density at the AlGaIn/GaN interface,

$$\sigma = P_{sp}(AlGaIn) + P_{pe}(AlGaIn) - P_{sp}(GaN) + P_{pe}(GaN) \quad (7)$$

The spontaneous P_{sp} and piezoelectric P_{pe} charges inherent of AlGaIn/GaN HEMTs are modeled based on the method outlined in [15], and are shown below,

$$P_{sp}(x') = (-0.052x' - 0.029) \text{ C/m}^2 \quad (8)$$

and,

$$P_{pe}(x') = 2 \frac{a(x') - a_o}{a_o} \left(e_{31}(x') - e_{33}(x') \frac{C_{13}(x')}{C_{33}(x')} \right) \text{ C/m}^2 \quad (9)$$

where, x' is the material mole fraction and a_o is the equilibrium lattice constant. The lattice constant for the ternary is:

$$a(x') = (-0.077x' + 3.189)10^{-10} \text{ m}, \quad (10)$$

The elastic and piezoelectric constants are:

$$C_{13}(x') = (5x' + 103) \text{ GPa},$$

$$C_{33}(x') = (-32x' + 405) \text{ GPa}, \quad (11)$$

$$e_{31}(x') = (-0.11x' - 0.49) \text{ C/m}^2$$

$$e_{33}(x') = (0.73x' + 0.73) \text{ C/m}^2$$

The polarization-induced sheet charges are incorporated as fixed charge source terms in the Poisson equation.

3.3 *Steady state solutions*

Electrical simulations are performed only near the active regions of the device, since uncontacted substrates, which are several hundred microns thick, are electrically irrelevant. However, for thermal simulations, since the heat sink is at the bottom of the substrate, it is important to include this region in the thermal simulation domain. Hence, the thermal transport equation in (1) is solved on a non-uniform two-dimensional extension of the electrical grid.

In steady state, equation (1) is discretized by the box method [202, 175]. The first step to discretization using the box method is to construct a Wigner-Seitz cell around each node. To do this, perpendicular bisectors are drawn to each edge connecting the node as shown in Figure 10. The partial differential equation in (1) is then integrated over the area of the box formed by the intersection of all the perpendicular bisectors.

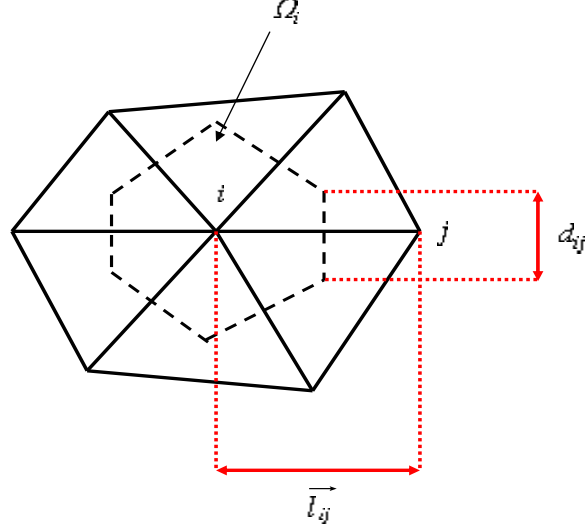


Figure 10: Schematic representation of the box method discretization for the lattice heat equation.

Applying the box method and using Green's theorem, equation (1) becomes [202],

$$\oint_C \kappa \nabla T \cdot \vec{dl} = \int_{\Omega} S d\Omega \quad (12)$$

\vec{dl} is the normal vector pointing outwards from each side of the box, with magnitude equal to the length of the corresponding side of the box. The integral on the right hand side is evaluated over the area of the box. The integral can also be expressed in a discrete form as,

$$\sum_{j=1, j \neq i}^m \bar{\kappa} \nabla T_{ij} d_{ij} = S_i \Omega_i \quad (13)$$

where T_{ij} is the temperature flux along the edge ij going from node i to j , d_{ij} is the length of the perpendicular bisector of the edge $\{ij\}$, S_i is the net power transferred

per unit volume into the acoustic modes and Ω_i is the area of the box around node i . The summation is carried out over all the nodes that connect to node i . m is the degree of node i which is defined as the number of nodes that directly connect to node i [49].

From Figure 11, the Poisson equation can be discretized in a similar manner,

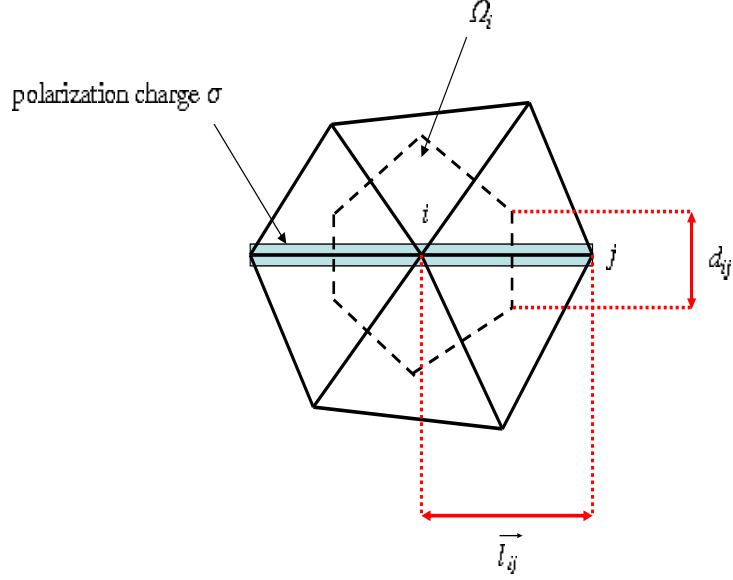


Figure 11: Schematic representation of the box method discretization for Poisson equation.

$$\sum_{j=1, j \neq i}^m \bar{\epsilon} \nabla \phi_{ij} d_{ij} = -\rho_i \Omega_i - \frac{1}{2} \sum_{j \neq i} \sigma_{ij} |\vec{l}_{ij}| \quad (14)$$

where, ϕ_{ij} is the electric flux from node i to j , ρ_i is the volumetric charge density at node i , σ_{ij} is the polarization charge, and $|\vec{l}_{ij}|$ is the length of the edge $\{ij\}$.

The resultant large system of linear equations arising from the discretization of (1) and (5) is of the form $Ax = b$, where A is a large symmetric sparse coefficient matrix, b is the source vector and x is the solution vector. Solutions are obtained by LU decomposition of the coefficient matrix A , solving for the unknown spatial temperature or potential via back substitution. Dirichlet boundary conditions are

applied to the electrodes and thermodes and von-Neumann boundary conditions are used on all other surfaces with vanishing fluxes.

The LU decomposition of such a large sparse matrix can prove inefficient, not only requiring large storage space, but also requiring considerable computational time. This computational burden is due to the “fill” associated with the LU decomposition [166]. The fill of a matrix is the number of non-zero elements appearing in the matrix after the LU decomposition is performed, in places where the original matrix had no previous entries. In such situations, simple node-reindexing techniques may be employed to reduce the bandwidth of the resultant coefficient matrix. The reduction in bandwidth leads to a reduction in memory storage space and also lessens the computational burden.

A widely used node-reindexing technique is the Cuthill-McKee (CM) algorithm [49]. A variant of the Cuthill-McKee reordering is the Reverse Cuthill-McKee (RCM) algorithm [70], which has been used here to reorder the nodes of the coefficient matrix A . In implementing the reordering scheme, the choice of the starting node plays a very important role as it determines the bandwidth and fill of the reordered matrix [49]. For this reason, a *pseudoperipheral node finder* is also employed to find a near-optimal starting node for the RCM reindexing scheme [72], details of which are described in the next section.

3.4 Efficient solutions of elliptic partial differential equations in two-dimensional semiconductor device simulations

In this section, the efficacy of the RCM algorithm to reduce the computational burden of the direct solution of 2D elliptic partial differential equations typically encountered in semiconductor device simulation is described, along with the details of the *pseudoperipheral node finder* algorithm. A comparison is presented of the computational burden of 1) the LU decomposition of the coefficient matrix, 2) back substitution,

both with and without the use of the RCM technique, and 3) “brute force” method to calculate fill as a function of the starting node in the mesh. The motivation for this work is that minimum degree may not always be the most efficient reordering algorithm for all device grids, and it is beneficial to have a flexible alternative like RCM available.

For the purpose of this work, two-dimensional meshes have been generated using ISETCAD MDRAW [1]. Figure 12 shows the node numbering scheme by MDRAW for a simple structured mesh of 25 nodes. For the solution of elliptic PDEs, such a node numbering scheme is inefficient since it gives rise to a coefficient matrix with a larger than necessary bandwidth. For larger matrices, this inefficiency can become particularly acute in the case of both structured and unstructured meshes as a result of excessive fill. A node-reindexing scheme can effectively reduce the bandwidth of the original coefficient matrix, which typically but not always improves the speed and performance of the program by reducing the fill associated with LU decomposition. This point shall be revisited later in the section.

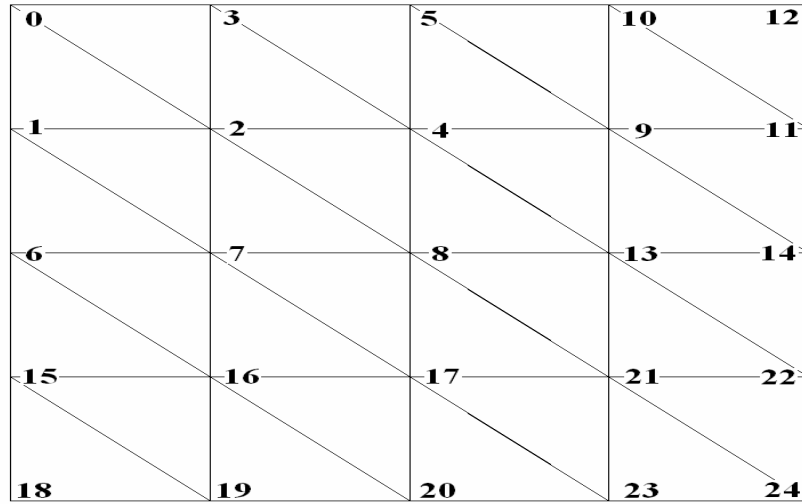


Figure 12: Original numbering scheme implemented by ISETCAD [1].

Cuthill-McKee reordering scheme is intended to generate a permutation matrix P

such that when P is applied to a system of linear equations of the form $Ax = b$, the following form is obtained [49]:

$$PAP^T(Px) = Pb \quad (15)$$

The resultant matrix PAP^T is sparse and symmetric. This resultant matrix can then be decomposed into a lower and upper triangular matrix.

The Cuthill-McKee algorithm selects a node of minimum degree as the root node and labels it x_1 . This is now the zero level structure with only the root node in this level. The unnumbered neighbors of this root node are then numbered x_2, x_3, \dots, x_m in increasing order of their degree m . This determines the first level structure of the reordering scheme. In the second level structure, the unnumbered neighbors of all the nodes in the first level are again numbered. This process is repeated until all the nodes in the mesh have been renumbered.

The RCM algorithm is a slight modification of the Cuthill-McKee algorithm, in which the ordering of the CM vertices is inverted. If the node numbering in the CM reordering scheme is denoted as $1, 2, \dots, N$ where N is the total number of nodes in the mesh, then the RCM reordering gives $N, N - 1, \dots, 2, 1$. It has been shown that RCM is often superior, but never inferior to the CM approach, from the perspective of computational efficiency and storage [110].

The efficiency of RCM algorithm depends on the choice of the starting node. In order to identify a good starting node for the mesh, the pseudoperipheral node finder algorithm described in reference [72] has been implemented. The algorithm is based on the *rooted level structure* [16].

If $G = (X, E)$ is a graph consisting of a set of nodes X and a set of edges E , then the distance $d(x, y)$ between any two nodes x and y in G is defined as the length of the shortest path between the two nodes [72]. The *eccentricity* of a node x , also

called the length is defined as [26],

$$l(x) = \max\{d(x, y) | y \in X\} \quad (16)$$

The *pseudoperipheral node finder* starts with an arbitrary node p in the set X . With this node as the root node, a level structure is constructed such that $L(p) = L_0(p), L_1(p), \dots, L_{l(p)}(p)$. $L_0(p)$ consists of only the root node. The next level $L_1(p)$ consists of the neighbors of the root node. Successive levels consist of neighbors of their previous levels. The width of the level structure is defined as [72],

$$w(x) = \max\{|L_i(x)| | 0 \leq i \leq l(x)\} \quad (17)$$

The next step in finding the pseudoperipheral node is to choose a node x in the last level $L_{l(p)}(p)$ which has a minimum degree. A new level structure is now constructed with x as the root node to give $L(x) = L_0(x), L_1(x), \dots, L_{l(x)}(x)$. If at this stage the eccentricity of node x is greater than the eccentricity of node p , then x replaces p and the whole process is repeated with this new root node x . In the final step, after the termination test is performed, node x is the pseudoperipheral node. This pseudoperipheral node now becomes the starting node for the RCM algorithm.

To illustrate the effect of the reindexing on the efficiency of direct solutions of the Poisson equation, tensor product grids with varying numbers of nodes were generated using MDRAW. RCM reordering was applied to each mesh. After reordering, LU decomposition was performed on the new permuted coefficient matrix followed by back substitution to obtain the solution vector. Simulation time required for LU decomposition and backfill operations both with and without application of the RCM algorithm is illustrated in Figure 13. As is evident, the benefit of the RCM algorithm for both LU decomposition and backfill operations increases monotonically with matrix size.

Figure 14 shows a mesh structure of an AlGaIn/GaN HEMT. The mesh has 3985 nodes. The solid lines at the top and bottom of the device indicate metal contacts

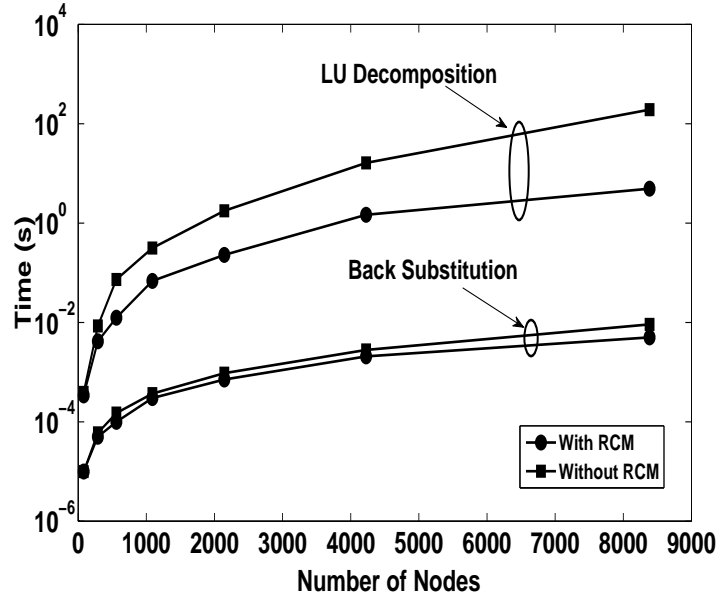


Figure 13: LU decomposition and back substitution time as a function of the number of nodes for a structured mesh.

where Dirichlet boundary conditions are applied. Figure 15 shows a plot of the fill of the coefficient matrix after LU decomposition as a function of the starting node, for the case of the 3985-node unstructured mesh. The fill of the original matrix after LU decomposition was found to be 1,323,752. Upon application of the RCM algorithm using the *pseudoperipheral node finder*, the fill was reduced to 386,090, representing an improvement of 70%.

Even though the RCM with pseudoperipheral node identification is able to substantially reduce the bandwidth of the original matrix, a significant further reduction in the amount of fill can be achieved by a brute force selection of the optimal starting node. In the case of the matrix considered in Figure 14, the brute force selection of the starting node reduces fill to 312,346, representing a further improvement of 19% to the fill. These computational techniques offer tremendous advantage to semiconductor device simulation, where thousands of sequential solutions of elliptic PDEs are common, and often contribute disproportionately to simulation time.

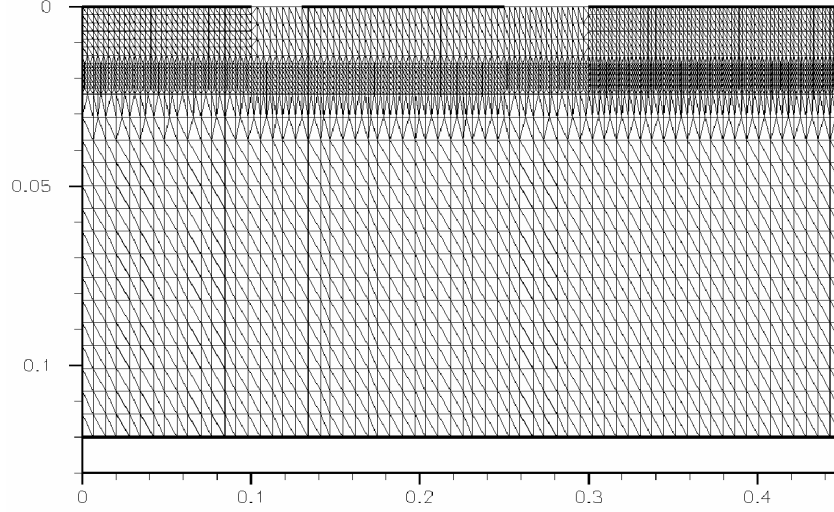


Figure 14: Unstructured mesh of an AlGaIn/GaN HEMT with 3985 nodes (dimensions in microns).

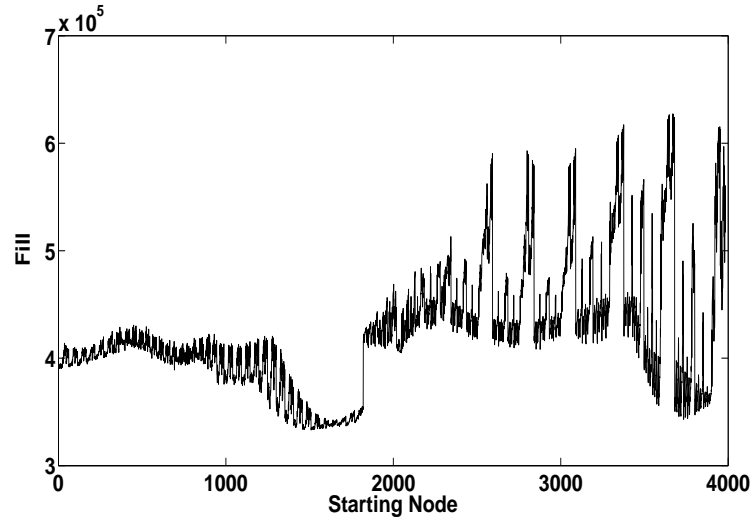


Figure 15: Fill introduced during LU decomposition of reindexed coefficient matrix as a function of starting nodes for the unstructured AlGaIn/GaN HEMT mesh in Figure 14.

Figures 16-18 show mesh structures for three devices obtained from the ISE TCAD example directory. The mesh of Tunnel Field Effect Transistor (FET) with 1254 nodes is shown in Figure 16. The solid lines in the mesh indicate metal contacts. Figure 17 is a mesh of a MOSFET with 2776 nodes and Figure 18 is that of an AlGaIn/GaN

HEMT with 4291 nodes. Table 3 presents a comparison of the fill produced in the coefficient matrix for LU decomposition for the following cases: a) without RCM, b) RCM using a pseudoperipheral node finder, and c) brute force selection of starting node for RCM, for each of the devices described above.

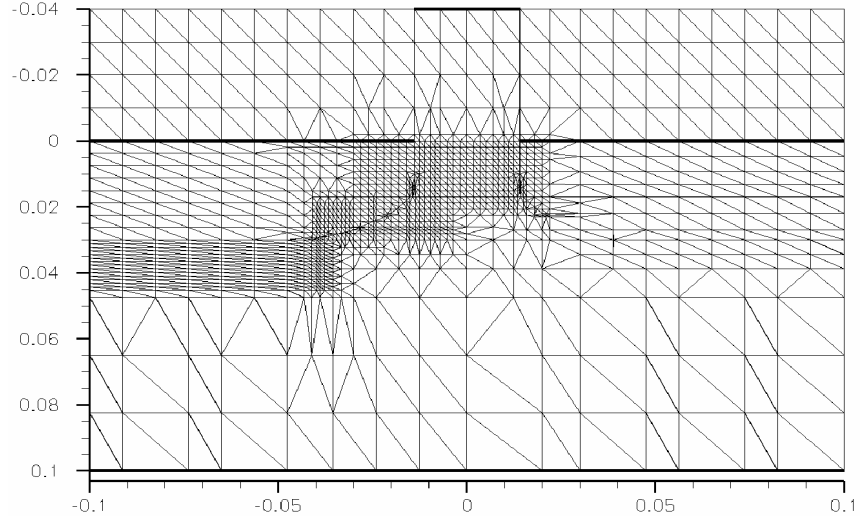


Figure 16: Unstructured mesh of a Tunnel Field Effect Transistor (FET) with 1254 nodes (dimensions in microns).

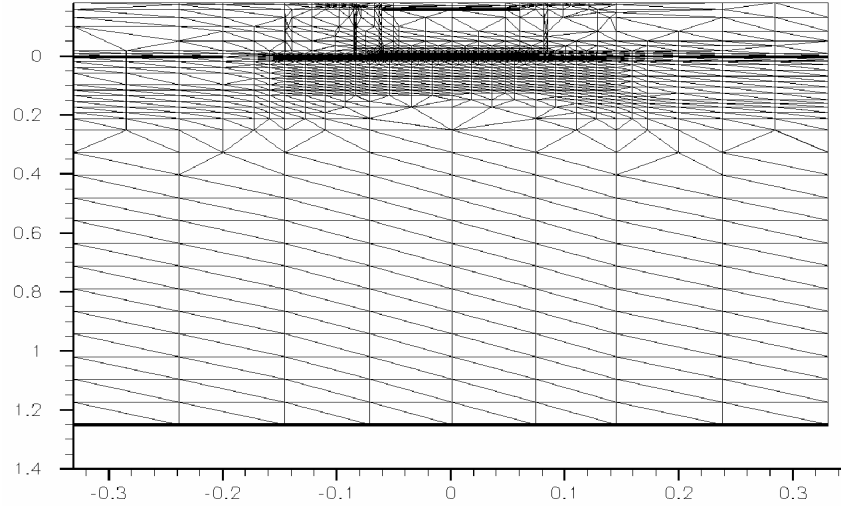


Figure 17: Unstructured mesh of a MOSFET with 2776 nodes (dimensions in microns).

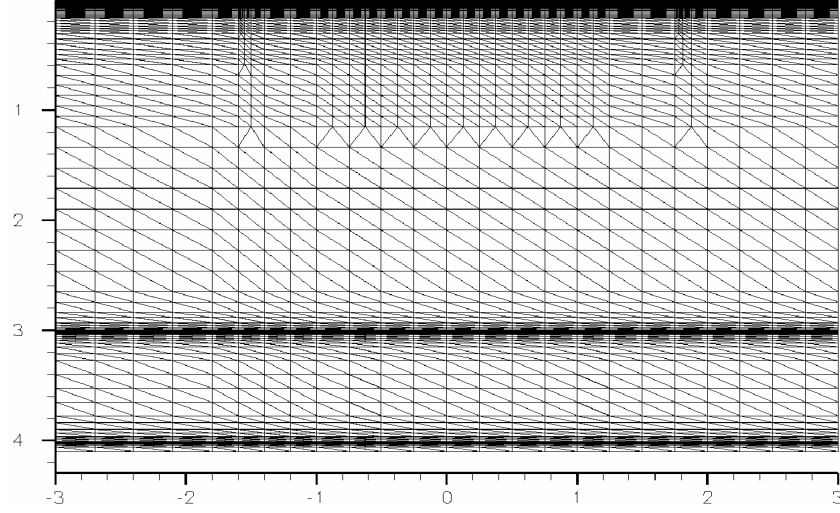


Figure 18: Unstructured mesh of an AlGaIn/GaN HEMT with 4291 nodes (dimensions in microns).

Brute force initial node selection in conjunction with the RCM algorithm achieves a full 29.3% reduction of the fill associated with LU decomposition of the Tunnel FET mesh. If only pseudoperipheral initial node selection is used, however, the fill associated with application of the RCM is greater than that for the un-reindexed mesh. The Tunnel FET example therefore underscores the advantage of brute force rather than pseudoperipheral selection of the RCM starting node. The RCM algorithm applied to the MOSFET example also achieves a significant reduction in the fill. Perhaps the most dramatic example, however, is that of the 4291-node AlGaIn/GaN HEMT structure, whose fill may be reduced by 66.36% through application of optimal RCM reindexing.

There also exist meshes for which the bandwidth reduction associated with RCM reordering can actually increase the fill after LU decomposition, which ultimately dictates the computational burden required to find the solution vector. One such example, demonstrated in Figure 19, is that of an unstructured mesh of an AlGaIn/GaN HEMT with 2507 nodes. Figure 20a depicts the LU decomposition of the original matrix, and Figure 20b is the LU decomposition of the same coefficient matrix, but

Table 3: Fill after LU decomposition for a) without RCM, b) with RCM and pseudoperipheral node finder and c) brute force method, for a Tunnel FET, MOSFET and AlGa_N/Ga_N HEMT.

Device	Without RCM	RCM with PNF	Brute Force
Tunnel FET (1254 nodes)	133,102	142,934	94,048
MOSFET (2776 nodes)	414,744	381,184	359,870
HEMT (4291 nodes)	896,237	315,765	301,479

for which RCM reindexing has been applied along with the *pseudoperipheral node finder*. In spite of providing a dramatic bandwidth reduction from 1547 to 134, application of the RCM algorithm actually results in a decomposed matrix with 417,373 non-zero entries, compared to only 176,637 entries in the decomposed form of the original matrix. Even after the brute force method selects an optimal RCM starting node, the best case fill cannot be reduced below 297,969 as is evident in Figure 20c. Although RCM is highly efficient for grids with long and thin level structures and a dominant axis, its efficiency is often surpassed by other approaches in the case of grids with no clearly dominant axis.

In summary, RCM is most effective in reducing the bandwidth and fill when the level structures are “long and narrow” [72, 71]. This means that the generated level structure has many levels and each level has few nodes. Thus, in the vast majority of cases, RCM reordering in conjunction with optimal initial node selection has been found to result in considerable reduction of computational burden for both the decomposition and backfill operations. Pseudoperipheral initial node selection for the RCM algorithm has been uniformly advantageous for tensor product grids, and usually so for the unstructured meshes studied here. Meshes with extreme two-dimensional refinement profiles are found to result in shorter and wider RCM level structures, with significant fill; in such cases, which appear to be the exception rather than the rule, a geometric partitioning algorithm with intra-partition reindexing may

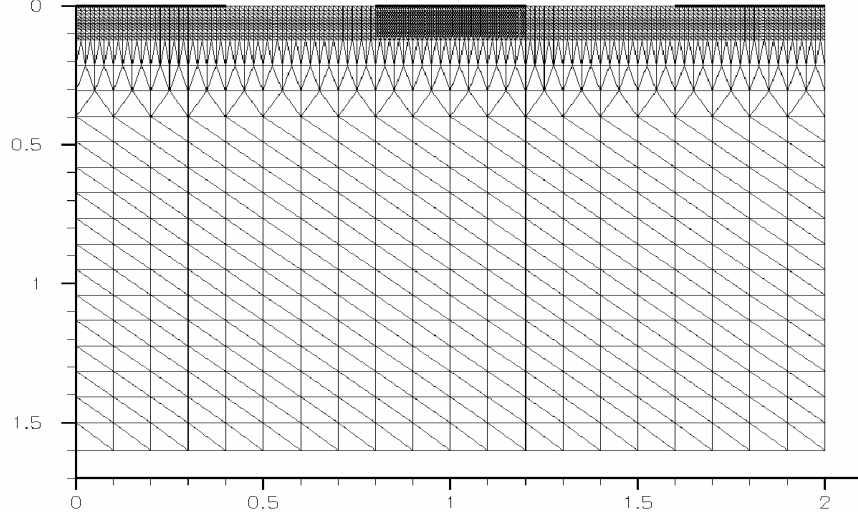


Figure 19: Unstructured mesh of an AlGaIn/GaN HEMT with 2507 nodes for which RCM fails to reduce the fill associated with LU decomposition (dimensions in microns).

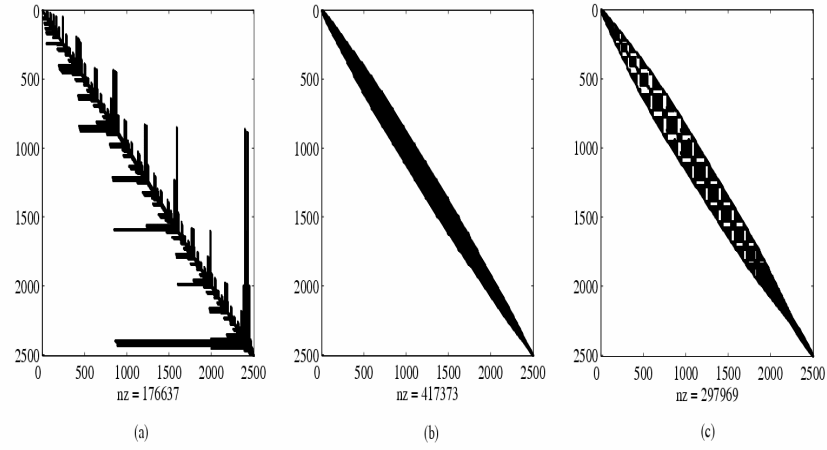


Figure 20: Example of limitation of RCM for the HEMT in Figure 19: (a) LU decomposed matrix without RCM. (b) LU decomposed matrix with RCM and pseudoperipheral node finder. (c) LU decomposed matrix with brute force selection of a starting node for RCM.

be preferable to the RCM strategy.

3.5 Simulation results

Electrostatic potential profile within an $\text{Al}_{0.15}\text{Ga}_{0.85}\text{N}/\text{GaN}$ HEMT with 180 nm doped ($N_d = 1 \times 10^{18} \text{ cm}^{-3}$) $\text{Al}_{0.15}\text{Ga}_{0.85}\text{N}$ barrier and 928 nm unintentionally doped GaN layer is depicted in Figure 21. The gate, drain, and source widths are $0.3 \mu\text{m}$ each, and the gate-source and gate-drain spacings are $0.55 \mu\text{m}$.

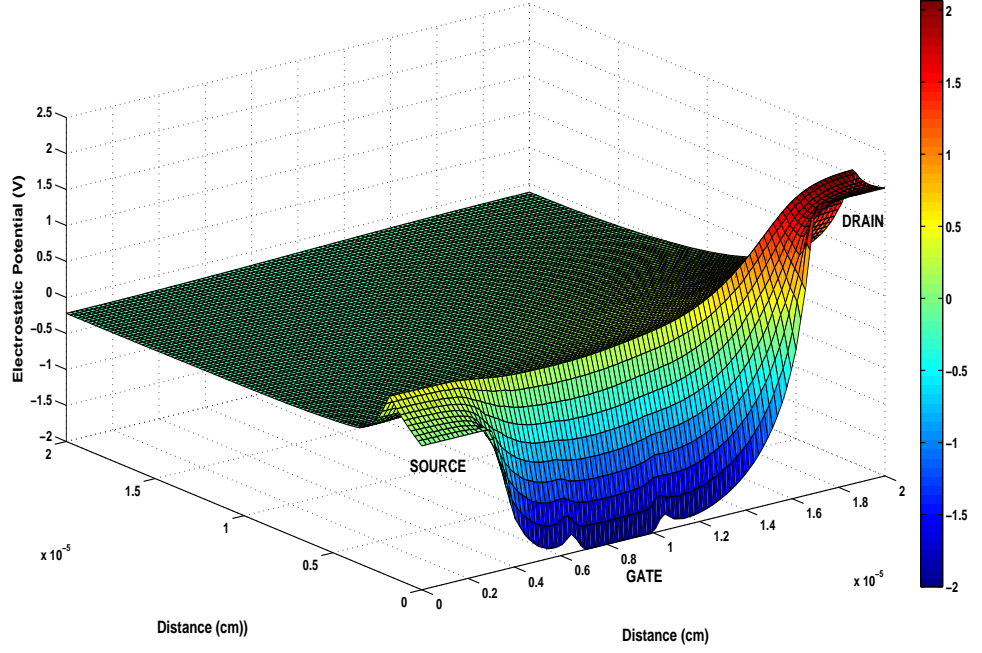


Figure 21: Electrostatic potential profile in an $\text{Al}_{0.15}\text{Ga}_{0.85}\text{N}/\text{GaN}$ HEMT. An external bias of $V_{gs} = -2 \text{ V}$ and $V_{ds} = 2 \text{ V}$ is applied to the gate and drain contacts.

A representative thermal simulation has been performed using a hierarchical meshing scheme. Figure 22 shows the electrical and thermal domains used in the simulations. Green's function solution of the lattice heat equation decreases rapidly and monotonically with the distance from the heat source. This calls for a meshing algorithm that is dense in regions with the heat source (electrical domain) and is coarse in regions away from the heat source (thermal domain). Therefore, to account for this, the meshing routine in the thermal simulations is implemented such that an i^{th} mesh

point in the extended thermal domain is at a distance of $i^2\delta$ from the corresponding boundary of the electrical domain. Here, δ is the mesh spacing in the thermal domain. In this case, the electrically simulated device consists of a 20 nm $\text{Al}_{0.15}\text{Ga}_{0.85}\text{N}$ barrier layer and a 200 nm intrinsic GaN. The doping level in the barrier is $1 \times 10^{18} \text{ cm}^{-3}$. The gate contact is 200 nm wide, the source-gate spacing is $1 \mu\text{m}$, and the gate-drain spacing is $1.5 \mu\text{m}$. Source and drain are modeled as Ohmic contacts and gate is modeled as a Schottky contact. For thermal transport modeling, a $300 \mu\text{m}$ thick SiC substrate is used, and a heat sink at 300 K is placed at the bottom of the substrate. von Neumann thermal boundary conditions are assumed on the top and sides of the device [144], imposing the constraint of zero flux.

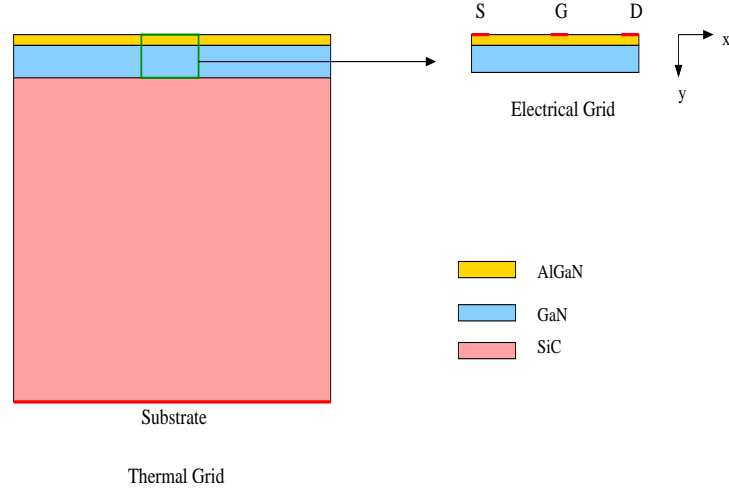


Figure 22: Cross section of the $\text{Al}_{0.15}\text{Ga}_{0.85}\text{N}/\text{GaN}$ HEMT showing the thermal and electrical grids.

Simulation results reveal a localized hot spot in the channel region between the gate and the drain contacts as illustrated in Figure 23, which shows the spatial variation of the non-equilibrium LO phonon occupation number at a low drain bias of $V_{ds} = 5 \text{ V}$. With an increase in the drain-to-source bias, the hot spot is expected to extend toward the drain end of the device (Figure 24), with a subsequent increase in the acoustic phonon temperature throughout the device. The acoustic phonon

temperature distribution at $V_{ds} = 40$ V is plotted in Figure 25. The peak acoustic phonon temperature in the device is 420 K.

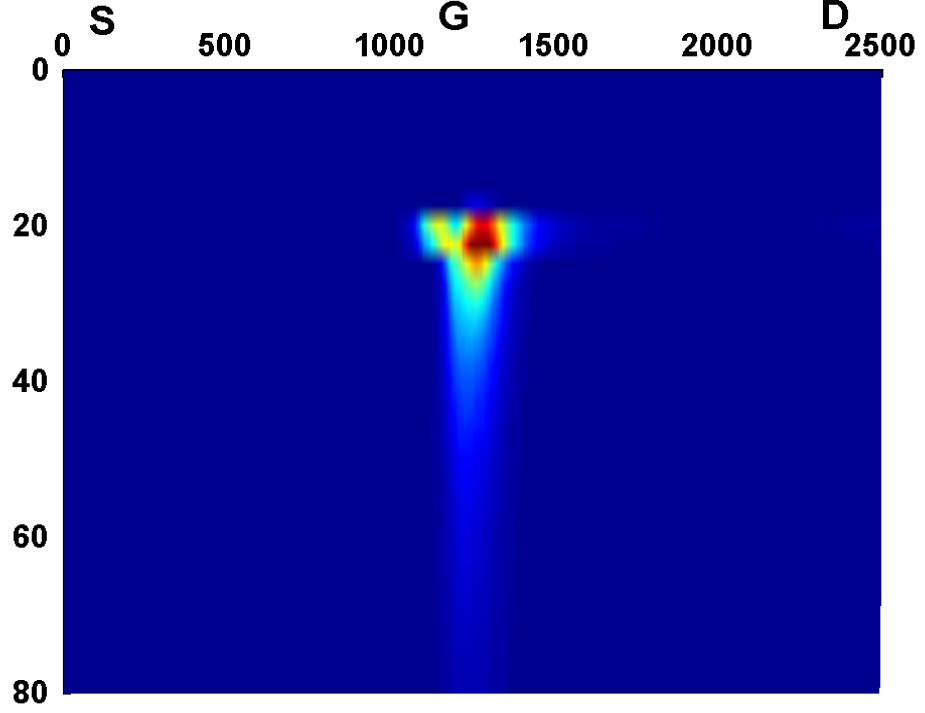


Figure 23: Spatial distribution of the non-equilibrium LO phonon occupation number in an $\text{Al}_{0.15}\text{Ga}_{0.85}\text{N}/\text{GaN}$ HEMT at $V_{ds} = 5$ V [184].

Figure 26 shows the variation in the peak acoustic phonon temperature in the device as a function of substrate thickness. The substrate material is SiC. As the substrate thickness increases from 0 to $500 \mu\text{m}$, the thermal resistance of the substrate is also expected to increase [223]. This may be understood by writing out Fourier's law of heat conduction [52]:

$$Q = \frac{KA}{t}(T - T_{sink}) = \frac{T - T_{sink}}{R} \quad (18)$$

$$R = \frac{t}{KA} \quad (19)$$

Here, Q is the heat transfer rate, T_{sink} and T are the temperature of the heat sink and device, K denotes the thermal conductivity, A is the cross sectional area, t is the

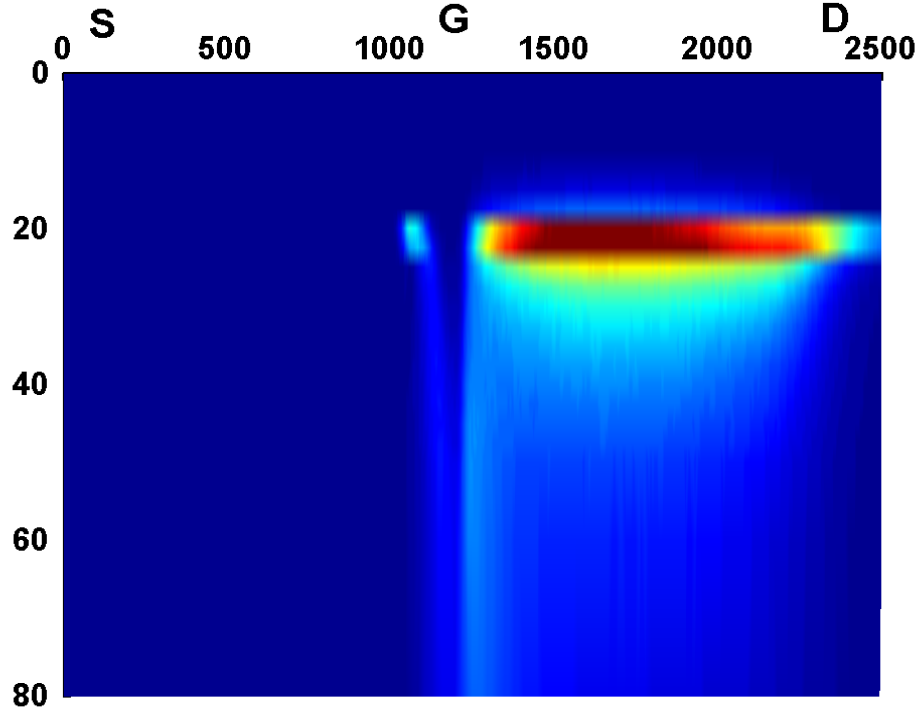


Figure 24: Spatial distribution of the non-equilibrium LO phonon occupation number in an $\text{Al}_{0.15}\text{Ga}_{0.85}\text{N}/\text{GaN}$ HEMT at $V_{ds} = 40$ V [184].

substrate thickness, and R is the thermal resistance. Accordingly, there is an almost linear rise in the temperature within the device with increasing substrate thickness.

Substrate material also plays an important role in determining the peak temperature in AlGaIn/GaN HEMTs. The peak acoustic phonon temperature along the HEMT y-axis is plotted in Figure 27 for three different substrate materials, namely, SiC, Si and sapphire. The substrate thickness in each case is $300 \mu\text{m}$. The thermal diffusivities of these materials are listed in Table 4. According to equation (18), temperature is inversely proportional to thermal conductivity or equivalently, thermal diffusivity. Since the thermal conductivity of SiC is the higher than that of Si and sapphire, the peak temperature with a SiC substrate is the lowest. On the other hand, a sapphire substrate shows the highest peak temperature in the device due to a lower thermal conductivity of sapphire.

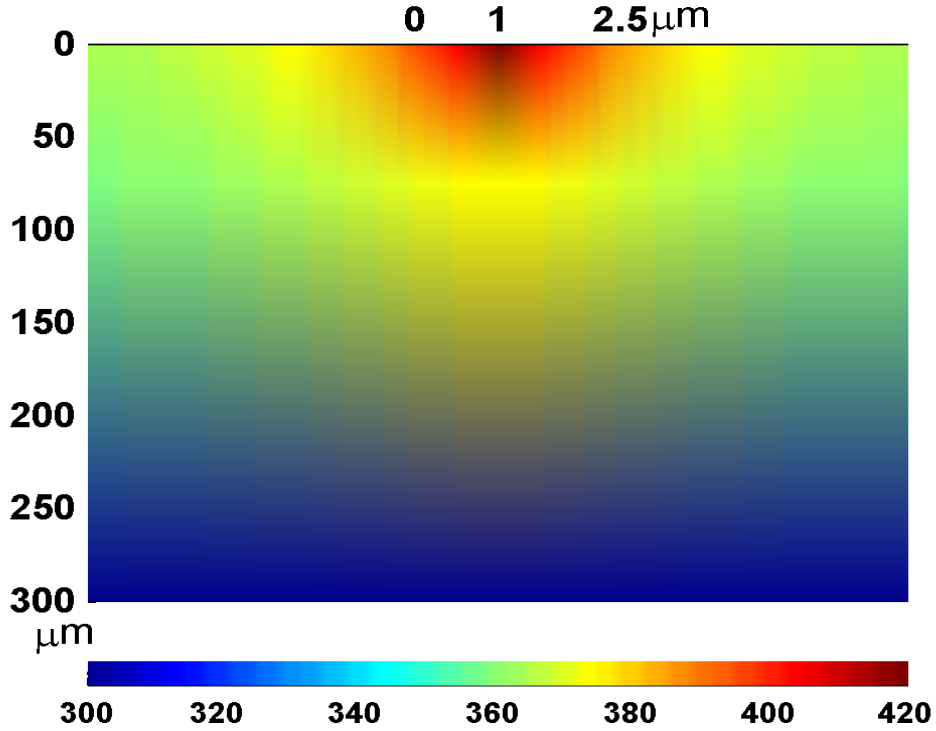


Figure 25: Acoustic phonon temperature distribution in an $\text{Al}_{0.15}\text{Ga}_{0.85}\text{N}/\text{GaN}$ HEMT at $V_{ds} = 40$ V. The peak temperature is 420 K and is located between the gate and drain electrodes [184].

3.6 Time-dependent solutions

There have been reports in literature suggesting contradicting effects of self-heating in GaN-based devices under pulsed mode operation. Measured [17] and simulated [223] current characteristics show that self-heating is particularly important at high electric fields, under pulsed mode operations. On the other hand, Barker *et al.* using pulsed voltage measurements, attribute the reduced saturated velocities in AlGaIn/GaN heterostructures to poor contacts as opposed to self-heating [22]. Additionally, width and duty cycle of the pulse, along with the characteristic length scales of the device also play a role in determining the self-heating effect under pulsed mode operation. To equip the simulator with this capability, a time dependent 2D lattice heat equation has been implemented. The heat equation is discretized in time using the Crank-Nicolson implicit discretization scheme [48], and the box method is used for spatial

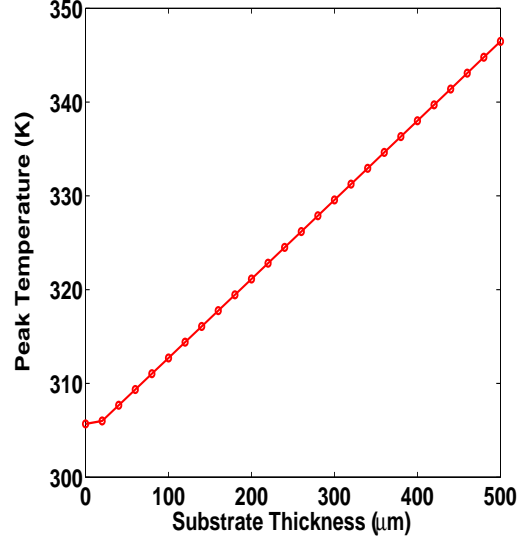


Figure 26: Peak acoustic phonon temperature in an $\text{Al}_{0.15}\text{Ga}_{0.85}\text{N}/\text{GaN}$ HEMT as a function of substrate thickness. An external bias of $V_{gs} = -2$ V and $V_{ds} = 2$ V is applied to the gate and drain contacts.

Table 4: Thermal Diffusivities of Substrate Materials

Material	Thermal Diffusivities (cm^2/s)
SiC	2.2
Si	0.8
Sapphire	0.1167

discretization [202, 175]. The resultant set of equations are of the form shown below,

$$AT^{n+1} = BT^n + S(x, y) = b \quad (20)$$

LU decomposition of the coefficient matrix can be carried out at the beginning of the simulation, and the time dependent temperature profile can be obtained by performing back substitution at each time step.

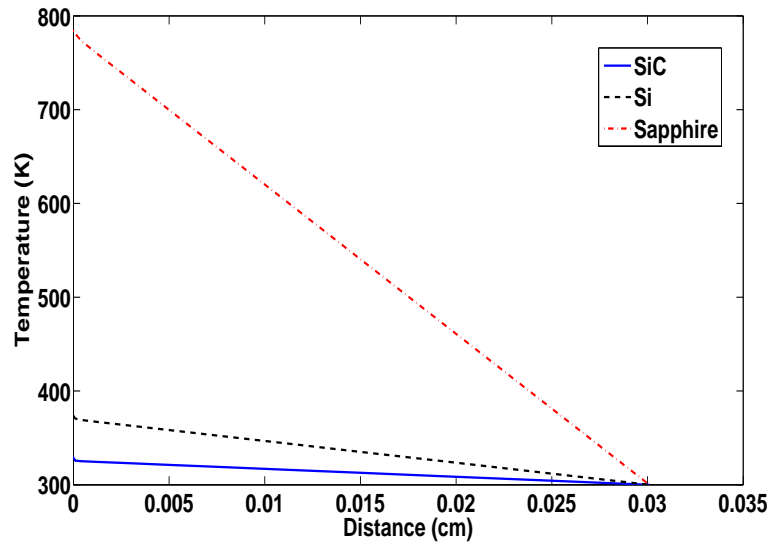


Figure 27: 1D profile of the peak acoustic phonon temperature in an $\text{Al}_{0.15}\text{Ga}_{0.85}\text{N}/\text{GaN}$ HEMT for different substrate materials. An external bias of $V_{gs} = -2$ V and $V_{ds} = 2$ V is applied to the gate and drain contacts.

CHAPTER IV

SIMULATION OF BULK GAN

4.1 MINILASE-A quantum well laser simulator

MINILASE is a two-dimensional quantum well (QW) laser simulator, that may be used to simulate GaAs-AlGaAs and AlGaAs-InGaAs based devices [182, 77]. The simulator features many of the models and algorithms used by silicon-based electron device simulators [170, 175, 59]. The electronic and optical equations appropriate for a two-dimensional quantum well laser are solved self-consistently. The electronic equations are the *Poisson equation* and *carrier continuity equations* for both free and bound electrons and holes [208]. The source term for the Poisson equation is the spatial profile of net volumetric charge density, and includes both the electron and hole free carrier densities, as well as partially ionized donor and acceptor densities. The former two quantities are themselves solution variables, while the latter two are either known or calculated via process simulation. The continuity equations balance the divergence of carrier flux with the net loss of carriers, considering recombination mechanisms like Shockley-Read-Hall and Auger, as well as spontaneous and stimulated radiative recombination.

Carrier transport in the bulk regions of the device is modeled with the drift-diffusion approximation. Ballistic transport across the heterojunctions is treated with Bethe's thermionic emission theory, under the assumption that the heterojunctions are abrupt [77]. Once the carriers are ballistically transferred across the heterojunctions into continuum states of the quantum well, there can be three possibilities [77]:

- The carriers can travel in the transverse direction, i.e., within the plane of the well. Drift-diffusion is used to model this transport and this accounts for current

spreading in the transverse direction.

- The carriers can cross the QW active region into the classical regions on the other side. Continuum electrons and holes in the active region are treated by drift-diffusion.
- The carriers can scatter into the bound quantum well states. This capture process into the bound states is modeled by carrier-carrier and carrier-phonon scattering.

In the bound states, carriers may either absorb phonons and be ejected back into the continuum states, or recombine through mechanisms like Shockley-Read-Hall and Auger as well as spontaneous and stimulated radiative recombination.

A scalar Helmholtz equation is solved for the optical problem, and a photon rate equation is used to calculate the photon occupation number of each mode.

The electronic bandstructure of the underlying material is calculated using the **k.p** method for zincblende material systems [206, 139]. Many-body effects such as bandgap renormalization and Coulomb enhancement of the optical matrix elements are likewise considered, with the former effect included in the local density approximation [140].

Simulation models to analyze nitride-based laser diodes have been previously developed by Witzigmann *et al.* [212, 213, 214]. However, it is the aim of this research to build upon a laser simulator that in the past has successfully predicted details of device operation. As a first step toward this goal, the electronic part of the two-dimensional quantum well simulator MINILASE is extended to model nitride materials and bandstructure [204]. Strain and spontaneous and piezoelectric polarization charges are considered in the calculation of the electronic states.

4.2 Introduction to *k.p*

To predict the electronic or optical properties of any device, it is essential to understand the bandstructure of the constituent materials, and in many cases deduce the quantum confined energy levels and envelope functions. Common methods used to

determine the bandstructure include the **k.p** method, the tight binding approximation, the orthogonalized plane wave method, the augmented plane wave method, the pseudopotential method, variational methods, and the cellular method.

Most optoelectronic devices such as lasers and LEDs, are made using direct bandgap materials. Optical transitions in these devices occur primarily at or near the band edges. Because of this, the relevant part of the bandstructure is confined to a small range of energies close to the band edges. The **k.p** method is the most widely used method for computing the bandstructure near band extrema in bulk materials and quantum well structures. Based on time independent perturbation theory, the **k.p** theory was first developed by Seitz to study the constitution of metallic lithium [173, 174]. Shockley extended the theory for the case of degenerate bands [179], and Dresselhaus *et al.* generalized to account for spin-orbit coupling. [54].

4.3 k.p for wurtzite nitrides

Due to the large bandgap energy in wurtzite III-nitrides, the conduction band may be modeled using to Löwdin's second order perturbation theory [108], and the valence bands with a coupled degenerate approach [45, 163, 31]. The strained 8x8 Hamiltonian is split into a 2x2 Hamiltonian for the conduction band and a 6x6 Hamiltonian for the valence bands. Decoupling the conduction and valence bands precludes the possibility for non-parabolicity in the former, but non-parabolicity is not important in the energy range of interest, and the explicit decoupling from the valence bands avoids the well known problem of spurious mid-gap states when this Hamiltonian is extended to one spatial dimension [99].

$$H = \begin{bmatrix} \lambda & 0 & -H & I^* & \Delta & 0 & 0 & 0 \\ 0 & \lambda & 0 & \Delta & -H & I^* & 0 & 0 \\ -H^* & 0 & F & K^* & 0 & 0 & 0 & 0 \\ I & \Delta & K & G & 0 & 0 & 0 & 0 \\ \Delta & -H^* & 0 & 0 & G & K^* & 0 & 0 \\ 0 & I & 0 & 0 & K & F & 0 & 0 \\ 0 & 0 & 0 & 0 & 0 & 0 & E_c & 0 \\ 0 & 0 & 0 & 0 & 0 & 0 & 0 & E_c \end{bmatrix} \begin{matrix} |u_3\rangle \\ |u_6\rangle \\ |u_1\rangle \\ |u_5\rangle \\ |u_2\rangle \\ |u_4\rangle \\ |u_7\rangle \\ |u_8\rangle \end{matrix} \quad (21)$$

where,

$$F = \Delta_1 + \Delta_2 + \lambda + \theta,$$

$$G = \Delta_1 - \Delta_2 + \lambda + \theta,$$

$$\begin{aligned} \lambda &= \frac{\hbar^2}{2m_o} [A_1 k_z^2 + A_2 (k_x^2 + k_y^2)] + D_1 \epsilon_{zz} + D_2 (\epsilon_{xx} + \epsilon_{yy}), \\ \theta &= \frac{\hbar^2}{2m_o} [A_3 k_z^2 + A_4 (k_x^2 + k_y^2)] + D_3 \epsilon_{zz} + D_4 (\epsilon_{xx} + \epsilon_{yy}), \end{aligned} \quad (22)$$

$$K = \frac{\hbar^2}{2m_o} A_5 (k_x + ik_y)^2 + D_5 \epsilon_+,$$

$$H = \frac{\hbar^2}{2m_o} i A_6 (k_x + ik_y) k_z - A_7 (k_x + ik_y) + D_6 \epsilon_{z+},$$

$$I = \frac{\hbar^2}{2m_o} i A_6 (k_x + ik_y) k_z + A_7 (k_x + ik_y) + D_6 \epsilon_{z+},$$

$$\Delta = \sqrt{2} \Delta_3.$$

Here, $\{A_i\}$ are the Luttinger-like parameters for wurtzite nitrides, $\{D_i\}$ are the valence band deformation potentials and k_i is the wavevector (transverse or longitudinal). The symbols Δ_1 , Δ_2 , and Δ_3 are related to the crystal-field split-off energy Δ_{cr} and the spin-orbit split-off energy Δ_{so} by the relation,

$$\Delta_1 = \Delta_{cr}, \quad \Delta_2 = \Delta_3 = \frac{\Delta_{so}}{3} \quad (23)$$

For a strained wurtzite quantum well/barrier system, the elements of the strain tensor are given by,

$$\begin{aligned}
\epsilon_{xx} &= \epsilon_{yy} = \frac{a_0 - a}{a}, \\
\epsilon_{zz} &= \frac{-2C_{13}}{C_{33}}\epsilon_{xx}, \\
\epsilon_{+} &= \epsilon_{xx} + 2i\epsilon_{xy} - \epsilon_{yy}, \\
\epsilon_{z+} &= \epsilon_{zx} + i\epsilon_{yz}.
\end{aligned} \tag{24}$$

where a_0 and a are the lattice constants of the substrate and the epitaxial layers, and C_{13} and C_{33} are the stiffness constants. If growth is along in the [0001] direction, then the off-diagonal terms in Equation (24) go to zero, i.e., $\epsilon_{xy} = \epsilon_{yz} = \epsilon_{zx} = 0$ and only the diagonal components of the strain tensor remain.

Including strain effects the conduction band may be described by the following equation:

$$\begin{aligned}
E_c &= \frac{\hbar^2}{2m_o} \left(\frac{k_x^2 + k_y^2}{m_e^t} + \frac{k_z^2}{m_e^z} \right) + E_g + \Delta_1 + \Delta_2 + P_{ce} \\
P_{ce} &= a_{cz}\epsilon_{zz} + a_{ct}(\epsilon_{xx} + \epsilon_{yy})
\end{aligned} \tag{25}$$

where, m_e^t and m_e^z are the electron transverse and longitudinal effective masses respectively, E_g is the bandgap energy, and a_{ct} and a_{cz} are the transverse and longitudinal conduction band deformation potentials. Given the hydrostatic deformation potentials a_1 and a_2 , the conduction band deformation potentials can be derived using the relations: $a_1 = (a_{cz} - D_1)$ and $a_2 = (a_{ct} - D_2)$ [153].

The band-edge basis functions $\{u_i\}$ are made up of linear combinations of $|X\rangle$, $|Y\rangle$ and $|Z\rangle$ orbitals for the valence bands and $|S\rangle$ orbitals for the conduction bands.

$$\begin{aligned}
|u_1\rangle &= \frac{-1}{\sqrt{2}} |(X + iY) \uparrow\rangle \\
|u_2\rangle &= \frac{1}{\sqrt{2}} |(X - iY) \uparrow\rangle \\
|u_3\rangle &= |Z \uparrow\rangle
\end{aligned} \tag{26}$$

$$\begin{aligned}
|u_4\rangle &= \frac{1}{\sqrt{2}} |(X - iY) \downarrow\rangle \\
|u_5\rangle &= \frac{-1}{\sqrt{2}} |(X + iY) \downarrow\rangle \\
|u_6\rangle &= |Z \downarrow\rangle \\
|u_7\rangle &= |S \uparrow\rangle \\
|u_8\rangle &= |S \downarrow\rangle
\end{aligned}$$

The bulk valence band structure may be determined by solving for the eigenvalues of the equation:

$$\det [H_{ij}^v(k) - \delta_{ij} E^v(k)] = 0 \quad (27)$$

The equation for quantum well structures may be obtained by replacing k_z in the bulk Hamiltonian with $-i \frac{\partial}{\partial z}$. The six valence subbands may be solved by the following equation [227, 44],

$$\sum_{j=1}^6 [H_{ij} + \delta_{ij} (E_0^v(z) + V_{pot}(z))] \phi_n^j(z, \mathbf{k}) = E_n^v(\mathbf{k}) \phi_n^i(z, \mathbf{k}) \quad (28)$$

where n is the valence subband index, E_0^v is the unstrained valence band energy in the quantum well, and V_{pot} is the electrostatic potential due to the charge carrier density in the QW. The envelope function for the valence bands may be expanded in a Fourier series as,

$$\begin{aligned}
\phi_n^j(z, \mathbf{k}) &= \frac{e^{i(xk_x + yk_y)}}{\sqrt{L}} \sum_m c_{n,m,k_x,k_y}^j e^{im \frac{2\pi}{L} z} \\
j &= 1, 2, \dots, 6
\end{aligned} \quad (29)$$

where L is the fundamental period, i.e., in this case $L = L_w + L_b$, where L_w and L_b are the widths of the quantum well and barrier regions respectively. c_{n,m,k_x,k_y}^j is the coefficient of the m^{th} Fourier component of the n^{th} envelope function for the j^{th} basis

function. The wave function of the n^{th} valence subband may therefore be described as,

$$\Psi_{n,k_x,k_y}^v(z) = \sum_j \phi_n^j(z, k_x, k_y) |u_j\rangle \quad (30)$$

$$j = 1, 2, \dots, 6$$

where $|u_j\rangle$ is defined in Equation (26).

Similarly, the conduction subbands may be determined through the relation,

$$[H^c + E_0^c(z) + V_{pot}(z)] \phi_{n'}(z, \mathbf{k}) = E_{n'}^c \phi_{n'}(z, \mathbf{k}) \quad (31)$$

$$H^c = \frac{\hbar^2}{2m_o} \left(\frac{k_x^2 + k_y^2}{m_e^t} + \frac{k_z^2}{m_e^z} \right) + P_{ce} \quad (32)$$

here n' denotes the conduction subband index. E_0^c is the unstrained conduction band energy in the quantum well. m_e^t and m_e^z are the electron effective masses in the transverse and longitudinal directions, respectively. P_{ce} is the hydrostatic shift in conduction band energy. The envelope function for the conduction band may be written in a manner similar to that of the valence bands:

$$\phi_{n'}(z, \mathbf{k}) = \frac{e^{i(xk_x + yk_y)}}{\sqrt{L}} \sum_m c'_{n',m,k_x,k_y} e^{im\frac{2\pi}{L}z} \quad (33)$$

Here again, c'_{n',m,k_x,k_y} has the analogous definition for electron states. The n^{th} conduction subband wavefunction is then written as,

$$\Psi_{n',k_x,k_y}^c(z) = \phi_{n'}(z, k_x, k_y) |u_i\rangle \quad (34)$$

$|u_i\rangle$ are band-edge basis functions for the conduction bands as described in Equation (26).

4.4 Optical matrix elements

Following the formulation presented in the previous section, the transition matrix elements (also called optical matrix elements (OME)) may be derived in terms of the band edge momentum matrix elements for all relevant wurtzite materials [44].

The transition matrix element describes the strength of the interaction between the conduction and valence band Bloch functions as defined in equation (26) [230]. In terms of the electron and hole wavefunctions defined by equations (30) and (34), the transition matrix element may be expressed as,

$$|\mathbf{M}_{n'n}^{c-v}(k_x, k_y)|_\alpha^2 = \left| \left\langle \Psi_{n',k_x,k_y}^c(z) | \hat{\mathbf{e}} \cdot \mathbf{p} | \Psi_{n,k_x,k_y}^v(z) \right\rangle \right|^2 \quad (35)$$

\mathbf{p} is the momentum operator, α defines the polarization of the field i.e., field \parallel QW plane (transverse electric (TE)) or field \perp QW plane (transverse magnetic (TM)), and $\hat{\mathbf{e}}$ is the unit polarization vector in the direction of the field. Writing the wavefunctions in terms of the envelope functions (or equivalently the Bloch functions) and expanding the envelope functions using plane waves, the transition matrix element becomes,

$$|\mathbf{M}_{n'n}^{c-v}(k_x, k_y)|_\alpha^2 = \sum_{\eta=\uparrow,\downarrow} \sum_{j=1}^6 \left| \langle u_c, \eta | \hat{\mathbf{e}} \cdot \mathbf{p} | u_j, \eta \rangle \sum_m c_{n',m,k_x,k_y}^{\prime*} c_{n,m,k_x,k_y}^j \right|^2 \quad (36)$$

where n' and n are the conduction and valence subband indices, k_x and k_y are the transverse wavevectors, η is the electron spin, index j runs over six valence bands, “*” denotes complex conjugate, and m runs over all plane waves of the Fourier basis.

Consider an optical transition between the conduction band and the heavy hole band for TE polarized field. The transition matrix element for this particular transition pair can be now written as,

$$|\mathbf{M}_{n'n}^{c-hh}(k_x, k_y)|_{TE}^2 = |\langle u_c, \uparrow | \hat{\mathbf{e}} \cdot \mathbf{p} | u_{hh}, \uparrow \rangle|^2 \left| \sum_m c_{n',m,k_x,k_y}^{\prime*} c_{n,m,k_x,k_y}^{hh} \right|^2 \quad (37)$$

The conduction and valence band Bloch functions of opposite spin do not couple because photons are spinless, and spin angular momentum must be conserved in the interaction [89, 111]. With this condition defined, the \uparrow and \downarrow notations have been dropped from the remainder of the derivation.

The dot product $\hat{\mathbf{e}} \cdot \mathbf{p}$ in equation (37) between the unit polarization vector and the momentum operator may now be replaced by $e_x p_x + e_y p_y$. Since only the TE mode is

considered here, $e_z = 0$. Also rewriting $|u_c\rangle$ and $|u_{hh}\rangle$ in terms of the basis functions $|S\rangle$, $|X\rangle$, and $|Y\rangle$ from equation (26), the first term in equation (37) becomes

$$\begin{aligned} |\langle u_c | \hat{\mathbf{e}} \cdot \mathbf{p} | u_{hh} \rangle|^2 &= \frac{1}{2} |\langle S | e_x p_x + e_y p_y | (X + iY) \rangle|^2 \\ &= \frac{1}{2} |\langle S | p_x | X \rangle e_x + i \langle S | p_y | Y \rangle e_y|^2 \end{aligned}$$

Using the fact the momentum operator is isotropic in the transverse plane, the above equation is given by,

$$|\langle u_c | \hat{\mathbf{e}} \cdot \mathbf{p} | u_{hh} \rangle|^2 = \frac{1}{2} |\langle S | p_x | X \rangle|^2 |e_x + ie_y|^2 \quad (38)$$

$|\langle S | p_x | X \rangle|^2$ is called the interband momentum matrix element [44]. The interband momentum matrix element is a fundamental material property, which may either be calculated theoretically or inferred from optical measurement.

$$|\langle S | p_x | X \rangle|^2 = \frac{m_o E_{px}}{2} \quad (39)$$

E_{px} is an energy parameter (also known as Kane's parameter) defined by the following expression [44],

$$E_{px} = \left(\frac{m_o}{m_e^t} - 1 \right) \frac{E_g [(E_g + \Delta_1 + \Delta_2)(E_g + 2\Delta_2) - 2\Delta_3^2]}{(E_g + \Delta_1 + \Delta_2)(E_g + \Delta_2 - \Delta_3^2)} \quad (40)$$

E_g is the bandgap energy. Substituting equation (38) and (39) into (37), the transition matrix element may now be expressed as,

$$|\mathbf{M}_{n'n}^{c-hh}(k_x, k_y)|_{TE}^2 = \frac{m_o E_{px}}{4} (e_x^2 + e_y^2) \left| \sum_m c_{n',m,k_x,k_y}^{*} c_{n,m,k_x,k_y}^{hh} \right|^2 \quad (41)$$

Similarly, the transition matrix elements for transitions between the conduction band and the LH and CH bands may be derived. Final expressions are shown below.

$$|\mathbf{M}_{n'n}^{c-lh}(k_x, k_y)|_{TE}^2 = \frac{m_o E_{px}}{4} (e_x^2 + e_y^2) \left| \sum_m c_{n',m,k_x,k_y}^{*} c_{n,m,k_x,k_y}^{lh} \right|^2 \quad (42)$$

$$|\mathbf{M}_{n'n}^{c-ch}(k_x, k_y)|_{TE}^2 = 0 \quad (43)$$

Similarly, for the TM mode,

$$|\mathbf{M}_{n'n}^{c-hh}(k_x, k_y)|_{TM}^2 = |\mathbf{M}_{n'n}^{c-lh}(k_x, k_y)|_{TM}^2 = 0 \quad (44)$$

$$|\mathbf{M}_{n'n}^{c-ch}(k_x, k_y)|_{TM}^2 = \frac{m_o E_{pz}}{2} e_z^2 \left| \sum_m c_{n',m,k_x,k_y}^{l*} c_{n,m,k_x,k_y}^{ch} \right|^2 \quad (45)$$

where the energy parameter E_{pz} is given as [44]

$$E_{pz} = \left(\frac{m_o}{m_e^z} - 1 \right) \frac{(E_g + \Delta_1 + \Delta_2)(E_g + 2\Delta_2) - 2\Delta_3^2}{(E_g + 2\Delta_2)} \quad (46)$$

A flowchart of the simulator is depicted in Figure 28.

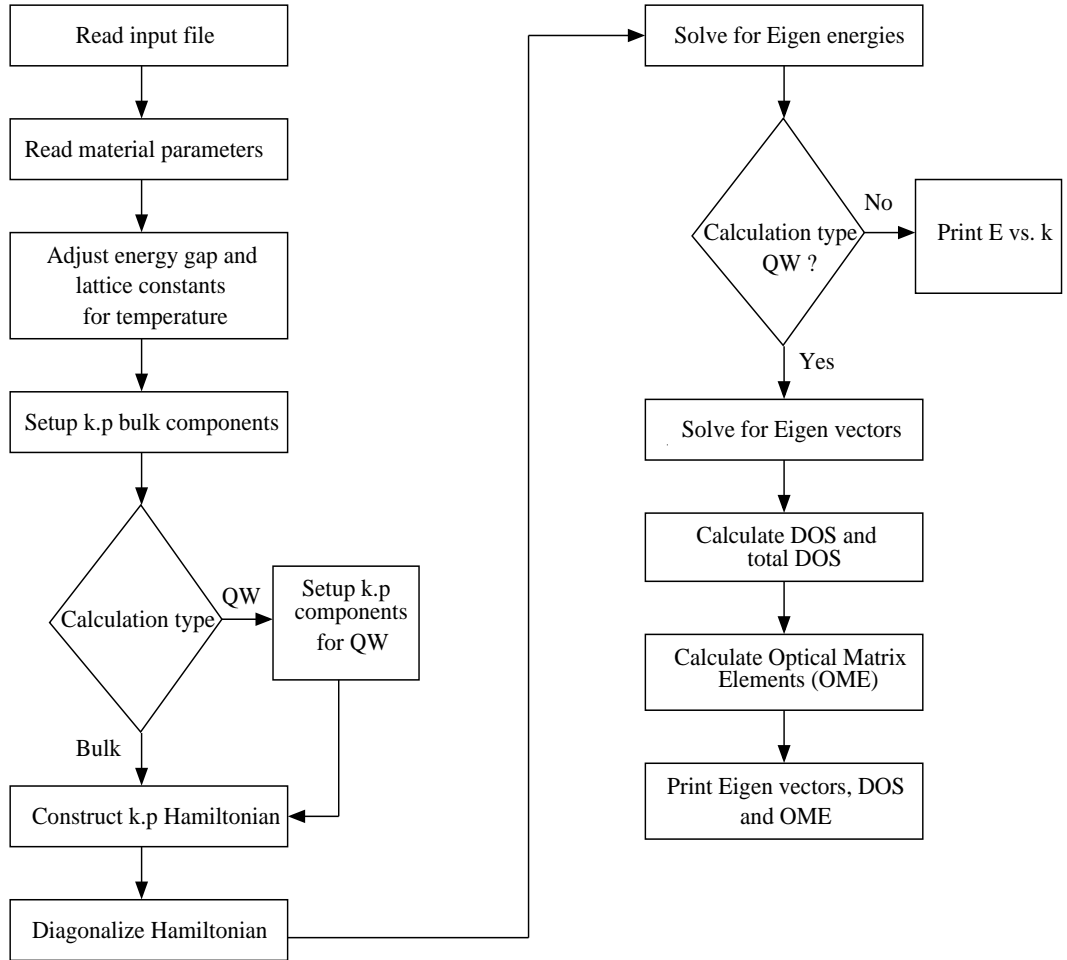


Figure 28: Flowchart of the laser simulator.

4.5 Bulk dispersion

Based on the formulation presented in the previous section, the valence band dispersion of bulk wurtzite GaN has been calculated. The influence of strain in the $\mathbf{k}\cdot\mathbf{p}$ Hamiltonian may be seen in Figure 29, which shows the valence band dispersion of bulk GaN near the zone center as a function of in-plane (k_z) and transverse (k_x) wavevectors with (a) showing the valence bands without any strain in the material and (b) 1% compressive biaxial strain applied to GaN. Material parameters for bulk GaN are listed in Table 5. The maxima of the valence band lies at the Γ point, i.e., at $|\mathbf{k}|=0$. Due to the spin-orbit and crystal-field coupling, the top of the valence band in GaN is split into three doubly degenerate subbands at the zone-center. The three subbands are called heavy hole (HH), light hole (LH) and crystal-field split-off (CH) bands respectively. The HH band has Γ_9 symmetry and the LH and CH bands have Γ_7 symmetry [126]. The anisotropy of the hole effective masses that is characteristic of III-V wurtzite nitrides is also evident in Figures 29-32. The HH band is nearly parabolic both \parallel and \perp to the c-axis, but with different parabolicities. However, due to the strong coupling between the LH and CH bands \perp to the c-axis, the LH bands are less parabolic in this direction. Due to the strongly anisotropic nature of the valence bands, the usual effective mass approximation cannot be used effectively to represent the valence band dispersion of wurtzite nitrides.

4.6 Effect of strain on the bulk bandstructure

Strain has a lesser impact on wurtzite GaN than GaAs. The result of applying a biaxial compressive strain to GaN is a downward shift of all the three valence bands. The HH and LH bands are shifted by almost equal amounts at zone center (see Figure 29b). However, at zone center, the CH band is disproportionately shifted to a lower energy with a flatter dispersion at larger wavevector. The biaxial compressive strain retains the crystal symmetry, thereby having little effect on the shift of the HH and

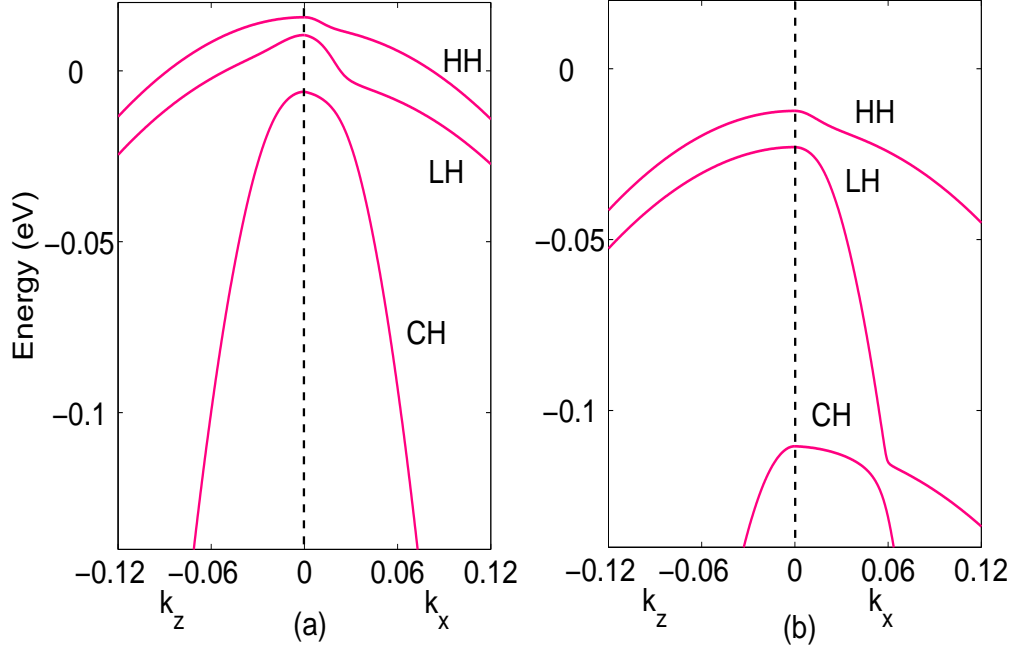


Figure 29: Valence band dispersion of bulk wurtzite GaN as a function of the longitudinal (k_z) and transverse (k_x) wavevectors (a) unstrained GaN and (b) 1% biaxial compressive strain applied to GaN.

LH bands [124].

4.7 Spin-orbit interaction

The Hamiltonian in equation (21) is slightly different from the $\mathbf{k}\cdot\mathbf{p}$ Hamiltonian formulated by Chuang [45]. In the Hamiltonian formulated by Chuang, the A_7 term, which represents part of the spin-orbit interaction required for wurtzite material, is not included. Without this contribution to the spin-orbit interaction, each of the valence bands are doubly degenerate. Including appropriate contribution to the spin-orbit interaction via the A_7 term in the Hamiltonian, this degeneracy is removed along the c -axis. The effect of the spin-orbit interaction on the valence band dispersion of bulk GaN is presented in Figure 30 (a) considering the spin-orbit interaction and (b) without any spin-orbit interaction.

The lifting of degeneracy is only seen along the \perp direction and is absent along

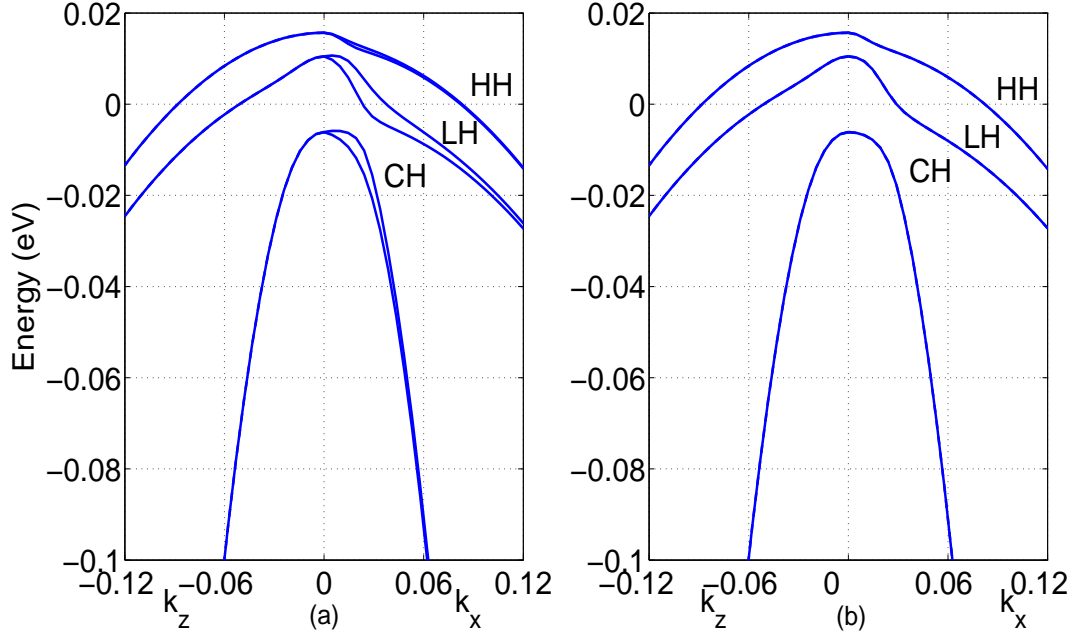


Figure 30: Valence band dispersion of bulk wurtzite GaN as a function of longitudinal (k_z) and transverse (k_x) wavevectors (a) with spin-orbit interaction and (b) without spin-orbit interaction.

the \parallel direction. This is because A_7 in the Hamiltonian only interacts with the \perp wavevectors. Proper inclusion of the spin-orbit interaction term in the Hamiltonian for wurtzite nitrides is known to result in larger calculated optical gain [162].

4.8 Verification of the bulk dispersion calculations

To verify the accuracy of the k.p calculations, the bulk valence band dispersion of unstrained and strained GaN is computed and compared with results previously reported by Chuang [45]. For this particular simulation, the spin-orbit coupling term A_7 is set to zero in the $\mathbf{k}\cdot\mathbf{p}$ Hamiltonian for this thesis for purposes of direct comparison. Binary material parameters for GaN are listed in Table.5. Comparison of the valence band dispersion as a function of wavevector may be found in Figure 31 for unstrained and Figure 32 for 1% compressively strained GaN. These figures demonstrate excellent agreement.

Table 5: Material Parameters for GaN [45].

Parameters	GaN
Lattice Constant (\AA)	
a	3.1892
c	5.185
Energy Parameters	
E_g (eV) at 300 K	3.44
Δ_{cr} (meV)	16
Δ_{so} (meV)	12
Valence band effective mass parameters	
A_1	6.56
A_2	-0.91
A_3	5.65
A_4	-2.83
A_5	-3.13
A_6	-4.86
Deformation potentials (eV)	
D_1	0.7
D_2	2.1
D_3	1.4
D_4	-0.7
Elastic stiffness constants (GPa)	
C_{13}	158
C_{33}	267

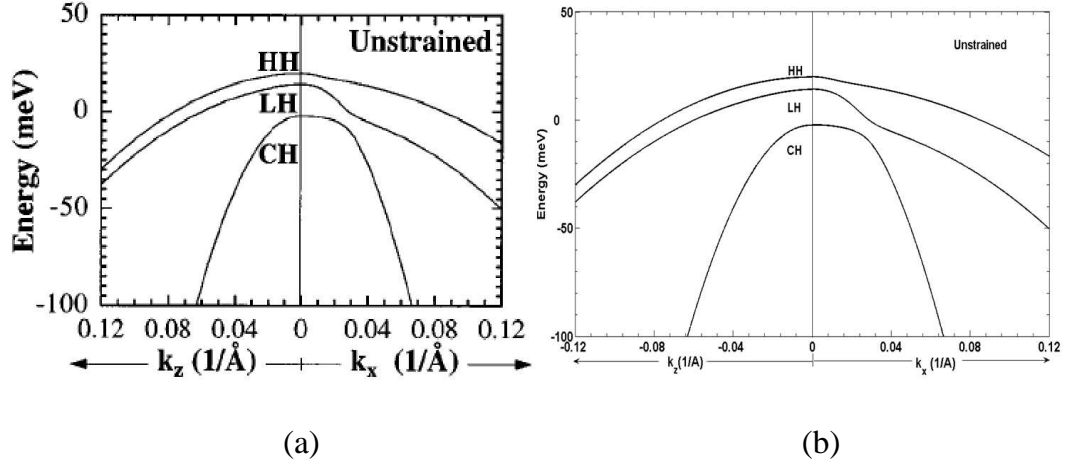


Figure 31: Unstrained valence band dispersion comparison for bulk GaN (a) Chuang's calculation [45] (b) Present work.

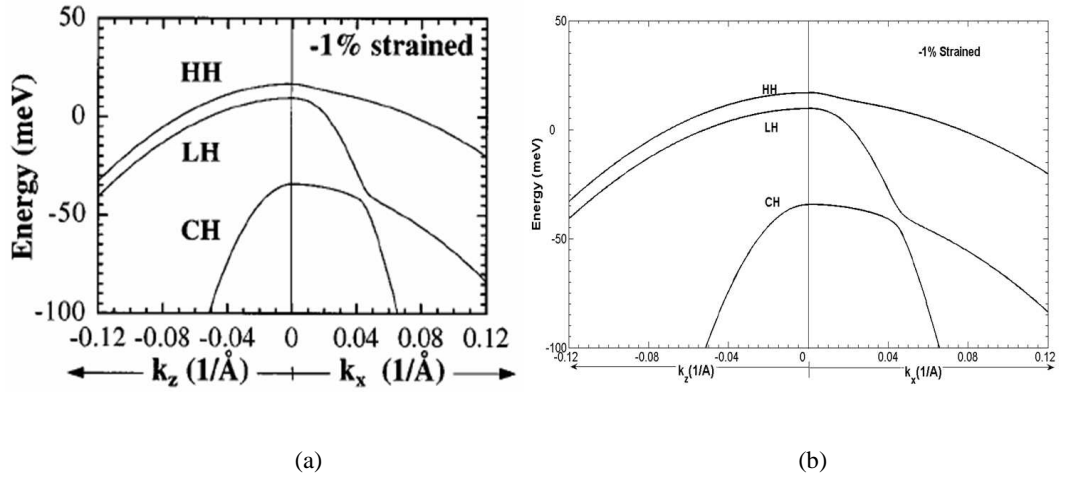


Figure 32: Strained valence band dispersion comparison for bulk GaN (a) Chuang's calculation [45] (b) Present work.

CHAPTER V

SIMULATION OF INGAN-BASED QUANTUM WELL STRUCTURES

5.1 *Quantum well dispersion*

The **k.p** method has been used to calculate the electronic and valence band dispersion of an $\text{In}_{0.2}\text{Ga}_{0.8}\text{N}/\text{GaN}$ single quantum well (SQW) system. Figure 33 shows the valence band dispersion curves considering biaxial compressive strain (dashed) and neglecting strain (solid) for two well widths (a) 25 Å and (b) 50 Å. Barrier widths for these structures are 4 nm and 9 nm respectively. Biaxial strain in the quantum well results from the lattice mismatch between the substrate and the epitaxial $\text{In}_{0.2}\text{Ga}_{0.8}\text{N}$ well material. This strain is about 2.16% and is compressive in nature due to the larger lattice constant of the well material. The barriers are lattice matched to the substrate and are unstrained. Material parameters for binary GaN and InN are listed in Table 6. As is common practice, deformation potentials for InN are adopted from known GaN values [154, 156]. All other parameters for the alloy $\text{In}_x\text{Ga}_{1-x}\text{N}$ (except the bandgap) are linearly interpolated using Vegard's law and are given as,

$$Y^{\text{In}_x\text{Ga}_{1-x}\text{N}} = xY^{\text{InN}} + (1-x)Y^{\text{GaN}} \quad (47)$$

The bandgap of the alloy is given by the following quadratic expression

$$E_g^{\text{In}_x\text{Ga}_{1-x}\text{N}} = xE_g^{\text{InN}} + (1-x)E_g^{\text{GaN}} - b^{\text{InGaN}}x(1-x) \quad (48)$$

where b^{InGaN} is the bowing parameter for the bandgap and is taken to be 1.2 eV [33]. A Varshni expression is used to adjust the bandgap for any arbitrary temperature,

$$E_g(T) = E_g(T_{\text{ref}}) + \alpha \left[\frac{T^2}{T + \beta} - \frac{T_{\text{ref}}^2}{T_{\text{ref}} + \beta} \right] \quad (49)$$

where $E_g(T_{ref})$ is the bandgap energy at temperature T_{ref} and α and β are the fitting parameters in units of (eV/K) and (K) respectively.

The conduction to valence band offset ratio is taken to be $\Delta E_c:\Delta E_v = 0.7:0.3$ [120, 104, 103]. Thirty Fourier coefficients are used in the bandstructure calculation.

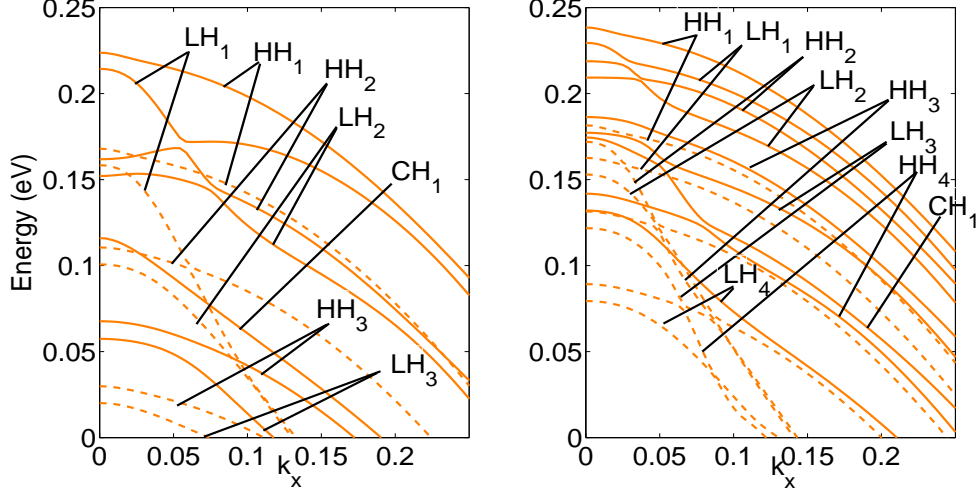


Figure 33: Unstrained (solid curve) and strained (dashed curve) valence band dispersion profiles of an $\text{In}_{0.2}\text{Ga}_{0.8}\text{N}/\text{GaN}$ single quantum well. (a) $L_w = 25 \text{ \AA}$ and (b) $L_w = 50 \text{ \AA}$.

For the case of InGaN/GaN quantum wells, biaxial compressive strain only increases the crystal-field split-off energy, while the shape of the valence band dispersion remains essentially unchanged. This is because the biaxial compressive nature of the strain retains the C_{6v} symmetry of the wurtzite crystal [126]. Wurtzite GaN is less affected by biaxial strain than zincblende GaAs. Unstrained wurtzite GaN can be thought of as prestrained zincblende crystal, since the HH and LH bands are separated at the zone center in both cases. The impact of biaxial strain (compressive or tensile) on the valence bands of wurtzite nitrides is to merely shift the energy values [128].

5.2 Inclusion of polarization charges in $k.p$

For a pseudomorphic Ga-face $\text{In}_x\text{Ga}_{1-x}\text{N}/\text{GaN}$ structure, the spontaneous polarization points toward the substrate and piezoelectric polarization points toward the surface (see Figure 8). The total polarization charge in a layer is the sum of spontaneous and piezoelectric polarization charges, i.e.,

$$P_{tot} = P_{sp} + P_{pe} \quad (50)$$

The GaN barriers are assumed to be lattice matched to the substrate, while the $\text{In}_x\text{Ga}_{1-x}\text{N}$ wells are under strain. The spontaneous and piezoelectric charges in the well are given as,

$$\begin{aligned} P_{sp}^{\text{In}_x\text{Ga}_{1-x}\text{N}} &= xP_{sp}^{\text{InN}} + (1-x)P_{sp}^{\text{GaN}} \\ P_{pe}^{\text{In}_x\text{Ga}_{1-x}\text{N}} &= 2\epsilon_{xx}\Lambda^{\text{In}_x\text{Ga}_{1-x}\text{N}} \end{aligned} \quad (51)$$

$\Lambda^{\text{In}_x\text{Ga}_{1-x}\text{N}}$ is linearly interpolated between the binary values Λ^{InN} and Λ^{GaN} , each of which are in turn proportional to the piezoelectric and elastic stiffness constants.

$$\Lambda^{\text{In}_x\text{Ga}_{1-x}\text{N}} = x\Lambda^{\text{InN}} + (1-x)\Lambda^{\text{GaN}}$$

and

$$\Lambda = e_{13} - e_{33}\frac{C_{13}}{C_{33}} \quad (52)$$

The x-component of the strain tensor is,

$$\epsilon_{xx} = \frac{a_o - a}{a},$$

Here, a_o and a are the lattice constants of the substrate (GaN) and epilayers respectively. In case of the $\text{In}_x\text{Ga}_{1-x}\text{N}$ quantum well material, the strain is compressive in nature and ϵ_{xx} is negative. e_{13} and e_{33} are the piezoelectric constants in (C/m^2) and C_{13} and C_{33} are the elastic stiffness constants in units of (GPa). Reliable binary material parameters used in the calculation of polarization charge are listed in Table 6.

The electric field in each layer is proportional to the difference in the polarization charges at each interface and is given by,

$$E_b = \frac{-L_w(P_{tot}^b - P_{tot}^w)}{(L_b\epsilon_w + L_w\epsilon_b)\epsilon_o}$$

$$E_w = -\frac{L_b}{L_w}E_b = \frac{L_b(P_{tot}^b - P_{tot}^w)}{(L_b\epsilon_w + L_w\epsilon_b)\epsilon_o} \quad (53)$$

P_{tot}^b and P_{tot}^w are the total polarization charges in the barrier and well respectively. L_b and L_w are the lengths and ϵ_b and ϵ_w are the dielectric constants of the barrier and well respectively, and ϵ_o is the permittivity of free space. Screening of the polarization fields is considered via the QW carrier-induced electrostatic potential as described in (28). Periodic boundary conditions are applied to calculate the built-in electric fields [28]:

$$\sum_i L_i E_i = 0 \quad (54)$$

where the sum runs over all the layers, L_i is the width of the i^{th} well or barrier, and E_i is the electric field in the i^{th} layer. In the electrostatic model adopted here, fields throughout the active region are independent of the number of quantum wells considered, by virtue of the periodic boundary conditions. In an actual device, an increase or decrease in the number of quantum wells will increase or decrease the thickness of the depletion region, respectively, and modify the *contribution* to the electrostatic field in the active region due to the built-in junction potential. We note that this contribution to the electrostatic field in the active region depends on materials and doping densities *outside* of the multiple QW (MQW) active region, but for typical device structures is on the order of 100kV/cm at zero bias. This is to be compared to the contribution to the electrostatic field in the MQW active region from the polarization charge, which is typically in the range of 1-3MV/cm, i.e., an order of magnitude higher. Furthermore, as laser diodes are operated under strong forward

bias, the relative contribution to the electrostatic field in the active region due to the junction potential is far less significant during lasing.

Due to the fact that the supercell is periodically repeated outside the simulation domain, the calculated spectral density is per well. The electrostatic potential due to the field is,

$$V(z) = - \int_0^z dz' E(z') \quad (55)$$

This electrostatic potential is Fourier transformed and its coefficients are added appropriately to the **k.p** Hamiltonian in equation (21).

Figure 34 shows the conduction and valence band edges and normalized zone-center envelope functions of the first conduction (C1) and heavy hole (HH1) bands of a 25 Å In_{0.2}Ga_{0.8}N/GaN single quantum well. Two cases are considered here, namely, (a) no polarization at the In_{0.2}Ga_{0.8}N/GaN interface and (b) full polarization at the In_{0.2}Ga_{0.8}N/GaN interface. The built-in polarization fields cause a spatial separation of the electron and hole envelope functions. This separation of envelope functions reduces the overlap factor, and is known to degrade the intensity of electroluminescence. As the well width increases, it is expected that the electrons and holes will become more and more localized at the opposite ends of the QW reducing the transition probability even further. This is indicated in Figure 35 for a 50 Å well width. Polarization-induced built-in fields also cause a red-shift in transition energy associated with the QCSE [167].

5.3 *Calculation of optical gain*

The TE and TM optical gain for a quantum well system are calculated using an in-house gain module. Figure 36 shows the interface between the **k.p** solver and the gain module.

As a first step to the optical gain calculation, coefficients of plane waves from the **k.p** solver are transformed into real space envelope functions for the conduction and

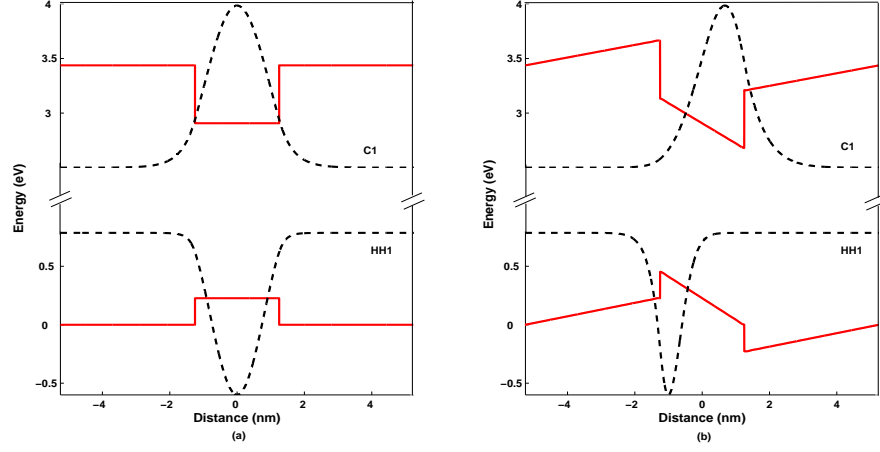


Figure 34: Conduction and valence band edges and envelope functions of the first conduction and heavy hole bands of a 25 Å $\text{In}_{0.2}\text{Ga}_{0.8}\text{N}/\text{GaN}$ single quantum well (a) no polarization at the interface and (b) full polarization at the interfaces.

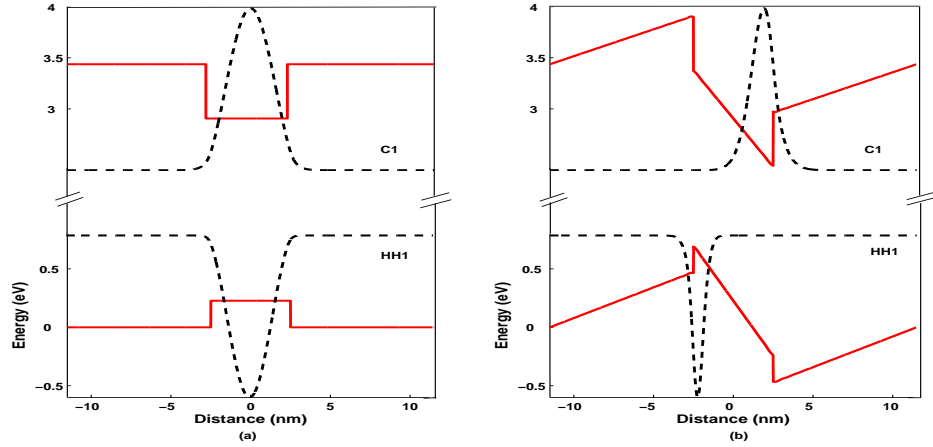


Figure 35: Conduction and valence band edges and envelope functions of the first conduction and heavy hole bands of a 50 Å $\text{In}_{0.2}\text{Ga}_{0.8}\text{N}/\text{GaN}$ single quantum well (a) no polarization at the interface and (b) full polarization at the interfaces.

valence bands. Next the interband transition matrix elements are calculated from the overlap between the conduction and valence subbands,

$$|\mathbf{M}_{n'n}^{c-v}(k_x, k_y)|_\alpha^2 = \sum_{\eta=\uparrow, \downarrow} \sum_{j=1}^6 \left| \langle u_c, \eta | \hat{\mathbf{e}} \cdot \mathbf{p} | u_j, \eta \rangle \sum_m c_{n', m, k_x, k_y}'^* c_{n, m, k_x, k_y}^j \right|^2 \quad (56)$$

Here, \mathbf{p} is the momentum operator, α defines the polarization of the field (TE or

TM), $\hat{\mathbf{e}}$ is the unit polarization vector in the direction of the field, u_c and u_j are conduction and valence band Bloch functions as defined in equation (26), n' and n are the conduction and valence subband indices, k_x and k_y are the x- and y-component of the wavevectors, η is the electron spin, index j runs over six valence bands, “*” denotes complex conjugate, and m runs over all plane waves of the Fourier basis. The density of states for the n^{th} conduction or valence subband is calculated as,

$$g_n(E) = \frac{1}{4\pi^2} \int dk_x \int dk_y \delta(E - E_n(k_x, k_y)) \quad (57)$$

The total density of states is then obtained by summing up the contribution from each subband i.e.,

$$g_{c,v}(E) = \sum_n g_n(E) \quad (58)$$

The Fermi energy dependence on the carrier density (N_c or N_v) is implicitly evaluated from the following relations,

$$N_c = \int_{-\infty}^{\infty} dE f_c(E) g_c(E) \quad (59)$$

and

$$N_v = \int_{-\infty}^{\infty} dE f_v(E) g_v(E) \quad (60)$$

Here, the Fermi-Dirac distributions are,

$$f_c = \frac{1}{1 + \exp\left(\frac{E - E_f^c}{k_b T}\right)} \quad (61)$$

and

$$f_v = \frac{1}{1 + \exp\left(\frac{-E + E_f^v}{k_b T}\right)} \quad (62)$$

where, E_f^c and E_f^v are the electron and hole Fermi energies, k_b is Boltzmann's constant.

The imaginary part of the quantum well susceptibility is then calculated as follows [4, 5],

$$\text{Im}(X_{TE}) = \frac{q^2 \pi}{(\hbar \omega)^2} \left(\frac{1}{2\pi} \right)^2 \pi p_{\perp} \left| \frac{\partial k^2(E)}{\partial E} \right| (1 - f_c - f_v)$$

$$Im(X_{TM}) = \frac{q^2\pi}{(\hbar\omega)^2} \left(\frac{1}{2\pi}\right)^2 \pi p_{\parallel} \left| \frac{\partial k^2(E)}{\partial E} \right| (1 - f_c - f_v) \quad (63)$$

where, q is the electronic charge, $\hbar\omega$ is the photon energy and, p_{\perp} and p_{\parallel} are the transition matrix elements.

The gain in the quantum well/barrier system for a given carrier density can then be obtained from the imaginary part of the quantum well susceptibility using the following relation [43],

$$G_{\alpha} = -\frac{4\pi\omega\mu c}{n_r} Im(X_{\alpha}) \quad (64)$$

where, α denotes TE or TM polarization of the field, ω is related to the photon energy, n_r is the refractive index of the material, c is the velocity of light in free space.

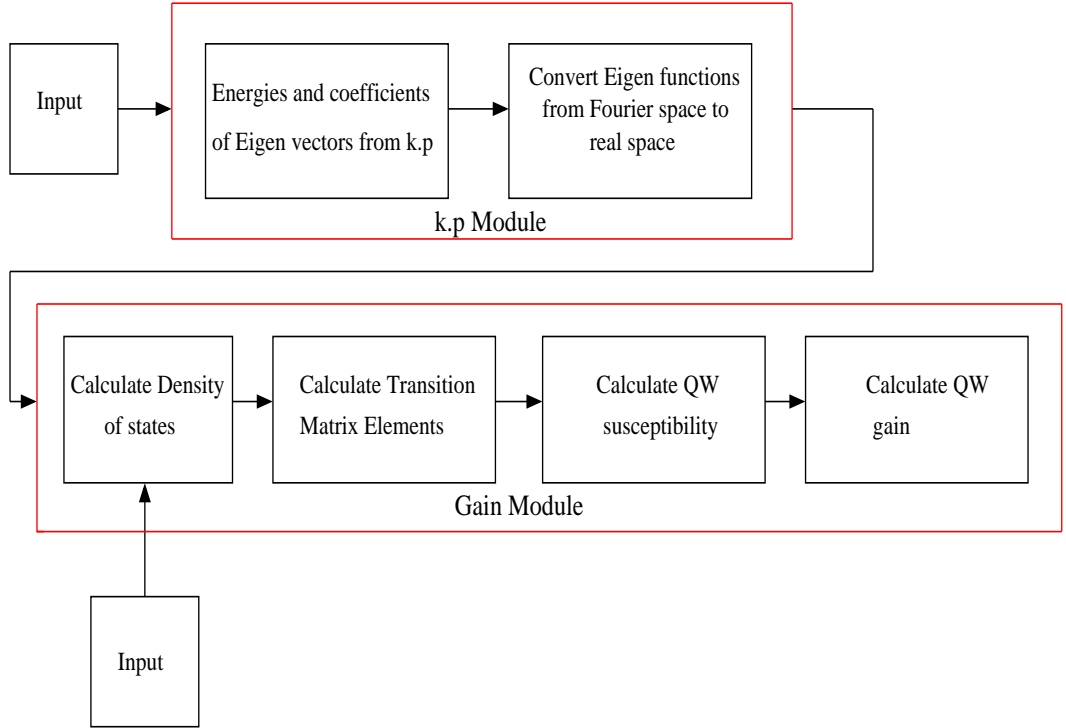


Figure 36: Flowchart of the interface between the **k.p** module and the gain calculation module.

5.4 Validation of quantum well dispersion calculations

The unstrained (Figure 37) and strained (Figure 38) valence band dispersions of an $\text{In}_{0.2}\text{Ga}_{0.8}\text{N}/\text{GaN}$ SQW structure are compared with the previously reported calculations of Yeo *et al.* [227] for (a) $L_w = 25 \text{ \AA}$ and (b) $L_w = 50 \text{ \AA}$. $\mathbf{k}\cdot\mathbf{p}$ calculations were performed with a basis of thirty Fourier coefficients. Binary material parameters for the calculation are taken from [226], in which the conduction to valence band offset ratio is $\Delta E_c:\Delta E_v = 0.7:0.3$. As Yeo *et al.* do not consider the influence of polarization in their SQW calculations, it is likewise ignored here for purposes of direct comparison. For both the unstrained and strained cases, the agreement is excellent.

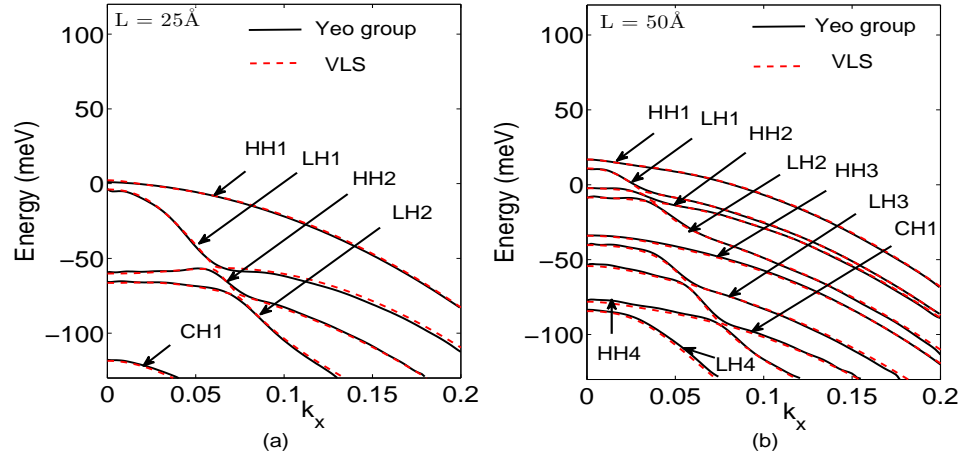


Figure 37: Unstrained valence band dispersion comparison for $\text{In}_{0.2}\text{Ga}_{0.8}\text{N}/\text{GaN}$ (a) $L_w = 25 \text{ \AA}$ and (b) $L_w = 50 \text{ \AA}$

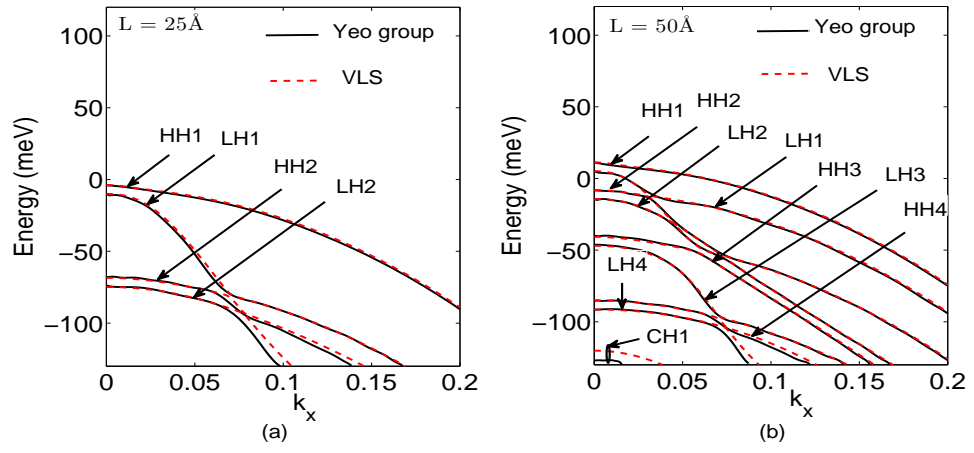


Figure 38: Strained valence band dispersion comparison for $\text{In}_{0.2}\text{Ga}_{0.8}\text{N}/\text{GaN}$ (a) $L_w = 25 \text{ \AA}$ and (b) $L_w = 50 \text{ \AA}$.

Table 6: Material Parameters for GaN and InN.

Parameters	GaN	InN
Lattice Constant* (\AA)		
a	3.188	3.540
c	5.185	5.70
Energy Parameters**		
E_g (eV) at 300 K	3.437	0.608
α (meV/K)	0.914	0.414
β (K)	825	154
Δ_{cr} (meV)	10	24
Δ_{so} (meV)	17	5
Conduction band effective masses*		
m_e^z/m_0	0.2	0.1
m_e^t/m_0	0.2	0.1
Valence band effective mass parameters**		
A_1	-7.21	-8.21
A_2	-0.44	-0.68
A_3	6.68	7.57
A_4	-3.46	-5.23
A_5	-3.40	-5.11
A_6	-4.90	-5.96
A_7 (meV/ \AA)	93.7	0
Deformation potentials (eV)**		
a_1^\uparrow	-4.9	-3.5
a_2^\uparrow	-11.3	-3.5
D_1^\uparrow	-3.7	-3.7
D_2^\uparrow	4.5	4.5
D_3	5.2	5.2
D_4	-2.7	-2.7
Elastic stiffness constants (GPa)*		
C_{13}	115	95
C_{33}	385	200
Piezoelectric constants (C/m²)*		
e_{13}	-0.33	-0.22
e_{33}	0.65	0.43
Spontaneous polarization (C/m²)*		
P_{sp}	-0.029	-0.032

* [157]

** [154]

 \uparrow [156]

CHAPTER VI

SIMULATION OF NON-(0001) INGAN-BASED LASERS

6.1 c-axis vs. non-c-axis

InGaN/GaN quantum well lasers grown along the c-axis have been described in the previous chapters. These c-axis laser diodes have two main problems associated with them, namely:

1. High threading dislocation densities along the c-plane: the dislocation densities degrade the device performance by acting as non-radiative recombination centers [183].
2. Large spontaneous and piezoelectric polarization induced electric fields: these fields give rise to a quantum-confined Stark effect, and decrease the electron-hole wavefunction overlap. This leads to longer radiative recombination lifetimes [105] that are well-width dependent and cause reduced emission efficiencies [50].

This thesis work deals with the second problem associated with built-in electric fields. Various solutions have been suggested in literature:

1. Screening of the polarization fields: this might either be achieved through optical excitation, electrical pumping or aggressive doping [63]. Excess photogenerated carriers may screen the polarization charges. However, for electrically pumped lasers, Piprek has demonstrated that the rate of charge injection may be insufficient to achieve the high carrier densities necessary for screening [158]. Also, unrealistically high doping densities may be required to achieve efficient screening of the fields.

2. Use of zincblende nitrides grown along [001] direction: the lack of favorable substrates make this difficult to achieve [73].
3. Growth of nitride devices on non-polar planes e.g., m-plane ($1\bar{1}00$) [207, 171] and a-plane ($11\bar{2}0$) [39], and on semi-polar planes (inclined with respect to the c-axis) such as ($10\bar{1}\bar{1}$) [199], ($10\bar{1}\bar{3}$) [176] and ($11\bar{2}2$) [65]: As the name suggests, semi-polar material exhibits reduced polarization-induced fields than c-axis material, while the non-polar planes are completely free from the polarization charges. Some common growth planes are illustrated in Figure 39. It has been reported that the optical gain in laser structures grown along non-[0001] directions is also significantly higher, owing to the larger optical matrix elements in non-[0001] directions [136, 137, 134]. In addition to macroscopic polarization charges, wurtzite GaN (c-plane) has a higher hole effective mass than zincblende GaAs [188, 200]. This results in higher threshold current densities in wurtzite GaN QW-based lasers compared to GaAs-based QW lasers. Alternate crystal orientations help to reduce the hole effective masses in GaN [136, 134] in the direction perpendicular to the plane of the QWs.

The first non-polar m-plane InGaN-based laser diode was demonstrated under pulsed mode condition by Schmidt *et al.*, with a threshold current density of 18 kA/cm² at 405.5 nm [171], and under continuous-wave operation by Okamoto *et al.* with a threshold current density of 4 kA/cm² at 400 nm [138]. Feezell *et al.* demonstrated the operation of non-polar laser diodes without AlGaIn cladding layers with a threshold current density of 3.7 kA/cm² under pulsed mode conditions [62], while Farrell *et al.* demonstrated the continuous-wave operation of these laser diodes with a threshold current density of 6.8 kA/cm² [61]. Lasing in the first semi-polar nitride-based laser diode under pulsed conditions was observed with a threshold current density of 18 kA/cm² at 405.9 nm [198]. Additionally, stimulated emission from non-polar and semi-polar InGaIn MQWs in the blue-green (480 nm) and green (514

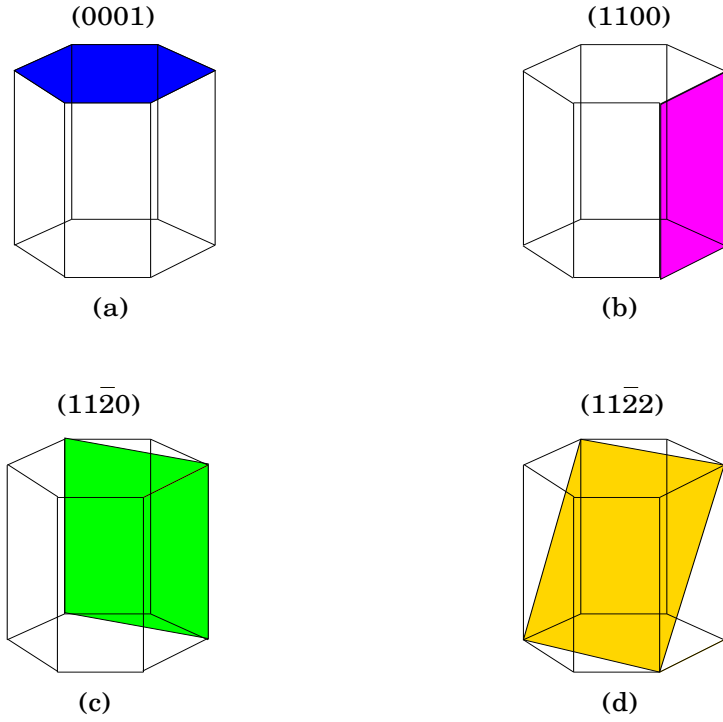


Figure 39: Schematic views of (a) polar (0001) c-plane, (b) non-polar m-plane ($\bar{1}\bar{1}00$), (c) non-polar a-plane ($11\bar{2}0$), and, (d) semi-polar plane ($11\bar{2}2$).

nm) wavelength regimes has also been realized [197]. With so much progress in the fabrication and growth of non- and semi-polar materials and structures, it becomes imperative to consider crystal orientation for predictive simulation of non-polar and semi-polar lasers.

6.2 Formulation of the $k \cdot p$ Hamiltonian for arbitrary crystal orientation

Crystal orientation plays a crucial role in dictating the electronic and optical properties of wurtzite III-nitrides, such as the valence band structure, hole effective mass, transition energies and optical matrix elements. This is because the spontaneous and piezoelectric polarization charges and strain vary as function of the crystal orientation [189]. To understand and model this dependence, the coordinates (x, y, z) along the c-axis must be transformed into new coordinates (x', y', z') of an arbitrary crystal

orientation, as shown in Figure 40, using a rotation matrix of the form [186],

$$U = \begin{pmatrix} \cos \theta \cos \phi & \cos \theta \sin \phi & -\sin \theta \\ -\sin \phi & \cos \phi & 0 \\ \sin \theta \cos \phi & \sin \theta \sin \phi & \cos \theta \end{pmatrix} \quad (65)$$

where, θ and ϕ are the polar and azimuthal angles, respectively, of z' with respect to the coordinates (x, y, z) . $\theta = 0^\circ$ is along the c-axis and $\theta = 90^\circ$ corresponds to the direction perpendicular to the c-axis or $[10\bar{1}0]$ direction. The wavevector k_i , strain tensor ϵ_{ij} and stiffness coefficient tensor C_{ijkl} can be transformed into the new coordinates [84, 135],

$$\begin{aligned} k'_i &= U_{ij}k_j, \\ \epsilon'_{ij} &= U_{ik}U_{jl}\epsilon_{kl}, \\ C'_{ijkl} &= U_{im}U_{jn}U_{ko}U_{lp}C_{mnop} \end{aligned} \quad (66)$$

or equivalently,

$$\begin{aligned} k_i &= U_{ji}k'_j, \\ \epsilon_{ij} &= U_{ki}U_{lj}\epsilon'_{kl}, \\ C_{ijkl} &= U_{mi}U_{nj}U_{ok}U_{pl}C'_{mnop} \end{aligned} \quad (67)$$

Here the Einstein rule for summation of repeated indices is used and U_{ij} are elements of the rotation matrix in (65) [135].

For arbitrary angles θ and ϕ , using (65) and (67) the Hamiltonian in 21 can be written as,

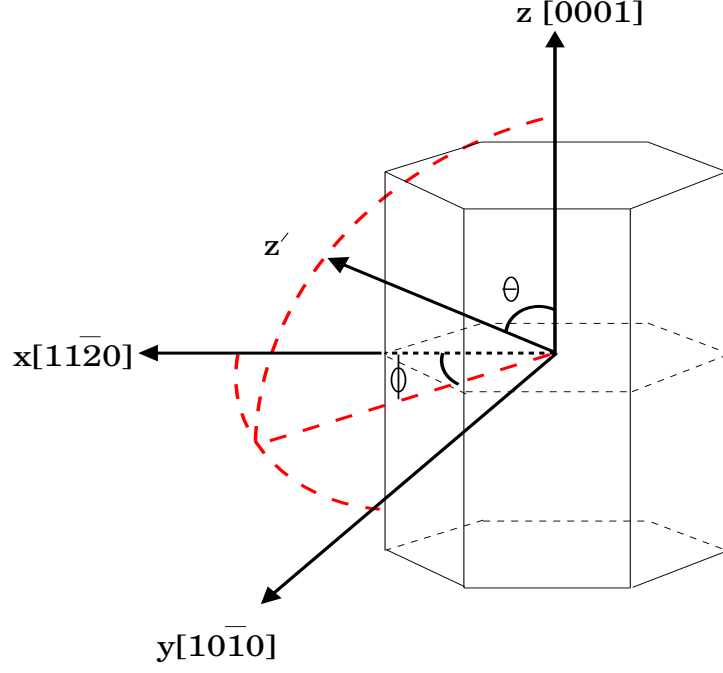


Figure 40: Relation between the conventional co-ordinate system (x, y, z) and transformed co-ordinate system (x', y', z') . The polar and azimuthal angles are denoted by θ and ϕ respectively.

$$H = \begin{bmatrix} \lambda' & 0 & -H' & I'^* & \Delta & 0 & 0 & 0 \\ 0 & \lambda' & 0 & \Delta & -H' & I'^* & 0 & 0 \\ -H'^* & 0 & F' & K'^* & 0 & 0 & 0 & 0 \\ I' & \Delta & K' & G' & 0 & 0 & 0 & 0 \\ \Delta & -H'^* & 0 & 0 & G' & K'^* & 0 & 0 \\ 0 & I' & 0 & 0 & K' & F' & 0 & 0 \\ 0 & 0 & 0 & 0 & 0 & 0 & E_c & 0 \\ 0 & 0 & 0 & 0 & 0 & 0 & 0 & E_c \end{bmatrix} \begin{matrix} |u_3\rangle \\ |u_6\rangle \\ |u_1\rangle \\ |u_5\rangle \\ |u_2\rangle \\ |u_4\rangle \\ |u_7\rangle \\ |u_8\rangle \end{matrix} \quad (68)$$

where,

$$F' = \Delta_1 + \Delta_2 + \lambda' + \theta',$$

$$G' = \Delta_1 - \Delta_2 + \lambda' + \theta',$$

$$\lambda' = \frac{\hbar^2}{2m_o} [A_1 K_z'^2 + A_2 (K_x'^2 + K_y'^2)] + D_1 \epsilon_{zz} + D_2 (\epsilon_{xx} + \epsilon_{yy}),$$

$$\theta' = \frac{\hbar^2}{2m_o} [A_3 K_z'^2 + A_4 (K_x'^2 + K_y'^2)] + D_3 \epsilon_{zz} + D_4 (\epsilon_{xx} + \epsilon_{yy}),$$

$$K' = \frac{\hbar^2}{2m_o} A_5 (K_x' + iK_y')^2 + D_5 \epsilon_+,$$

$$H' = \frac{\hbar^2}{2m_o} iA_6 (K_x' + iK_y') K_z' - A_7 (K_x' + iK_y') + D_6 \epsilon_{z+},$$

$$I' = \frac{\hbar^2}{2m_o} iA_6 (K_x' + iK_y') K_z' + A_7 (K_x' + iK_y') + D_6 \epsilon_{z+},$$

where K_x' , K_y' and K_z' can now be written as,

$$K_x' = k_x' \cos \theta \cos \phi - k_y' \sin \phi + k_z' \sin \theta \cos \phi,$$

$$K_y' = k_x' \cos \theta \sin \phi + k_y' \cos \phi + k_z' \sin \theta \sin \phi, \quad (69)$$

$$K_z' = -k_x' \sin \theta + k_z' \cos \theta$$

The strain tensor elements used in these calculations are formulated according to the model developed by Romanov *et al.* [165]. The strain model assumes that the piezoelectric and elastic properties are the same in any direction within the (0001) plane [135]. As a result, the strain elements depend only on the crystal orientation angle θ . This angle dependence of the strain components is demonstrated in Figure 41. For $\theta=0^\circ$, the strain elements reduce to the regular c-plane strain expressions presented earlier. The various strain elements are [165],

$$\begin{aligned} \epsilon_{xx} &= \epsilon'_{xx}, \\ \epsilon_{yy} &= \cos^2 \theta \epsilon'_{yy} + \sin^2 \theta \epsilon'_{zz} + \sin 2\theta \epsilon'_{yz}, \\ \epsilon_{zz} &= \sin^2 \theta \epsilon'_{yy} + \cos^2 \theta \epsilon'_{zz} - \sin 2\theta \epsilon'_{yz}, \\ \epsilon_{yz} &= \sin 2\theta \frac{\epsilon'_{zz} - \epsilon'_{yy}}{2} + \cos 2\theta \epsilon'_{yz}, \\ \epsilon_+ &= \epsilon_{xx} + 2i\epsilon_{xy} - \epsilon_{yy}, \\ \epsilon_{z+} &= \epsilon_{zx} + i\epsilon_{yz}, \end{aligned} \quad (70)$$

where,

$$\begin{aligned}
\epsilon'_{xx} &= \epsilon_1, \\
\epsilon'_{yy} &= \epsilon_2, \\
\epsilon'_{zz} &= \frac{(B_{41}\epsilon_1 + B_{42}\epsilon_2)A_{32} - (B_{31}\epsilon_1 + B_{32}\epsilon_2)A_{42}}{A_{31}A_{42} - A_{32}A_{41}}, \\
\epsilon'_{yz} &= \frac{(B_{31}\epsilon_1 + B_{32}\epsilon_2)A_{41} - (B_{41}\epsilon_1 + B_{42}\epsilon_2)A_{31}}{A_{31}A_{42} - A_{32}A_{41}}
\end{aligned} \tag{71}$$

here,

$$\begin{aligned}
\epsilon_1 &= \frac{a_{subs} - a_0}{a_0} \\
\epsilon_2 &= \frac{a_{subs}c_{subs} - \sqrt{\cos^2 \theta (a_0 c_{subs})^2 + \sin^2 \theta (a_{subs} c_0)^2}}{\sqrt{\cos^2 \theta (a_0 c_{subs})^2 + \sin^2 \theta (a_{subs} c_0)^2}} \\
A_{31} &= C_{11} \sin^4 \theta + \left(\frac{1}{2} C_{13} + C_{44} \right) \sin^2 2\theta + C_{33} \cos^4 \theta, \\
A_{32} &= [C_{11} \sin^2 \theta + (C_{13} + 2C_{44}) \cos 2\theta - C_{33} \cos^2 \theta] \sin 2\theta, \\
A_{41} &= \frac{1}{2} [(C_{11} - C_{13}) \sin^2 \theta + 2C_{44} \cos 2\theta + (C_{13} - C_{33}) \cos^2 \theta] \sin 2\theta, \\
A_{42} &= \left(\frac{C_{11} + C_{33}}{2} - C_{13} \right) \sin^2 2\theta + 2C_{44} \cos^2 2\theta, \\
B_{31} &= C_{12} \sin^2 \theta + C_{13} \cos^2 \theta, \\
B_{32} &= C_{13} (\sin^4 \theta + \cos^4 \theta) + \left(\frac{C_{11} + C_{33}}{4} - C_{44} \right) \sin^2 2\theta, \\
B_{41} &= \frac{C_{12} - C_{13}}{2} \sin 2\theta, \\
B_{42} &= \frac{1}{2} [C_{11} \cos^2 \theta - (C_{13} + 2C_{44}) \cos 2\theta - C_{33} \sin^2 \theta] \sin 2\theta
\end{aligned} \tag{72}$$

where, a_{subs} and a_0 are the lattice constants of the substrate and epitaxial layers respectively, and $\{C_i\}$ are the stiffness coefficients.

From Figure 41, ϵ_{xx} is independent of the crystal angle and ϵ_{zz} reaches its absolute maximum at $\theta=90^\circ$. ϵ_{zy} is zero for $\theta=0^\circ$ and $\theta=90^\circ$, and hence it is not expected to have an impact on the energy dispersion at these angles. As the crystal orientation angle increases, the strain tensor loses its biaxial nature, which it possessed at $\theta=0^\circ$.

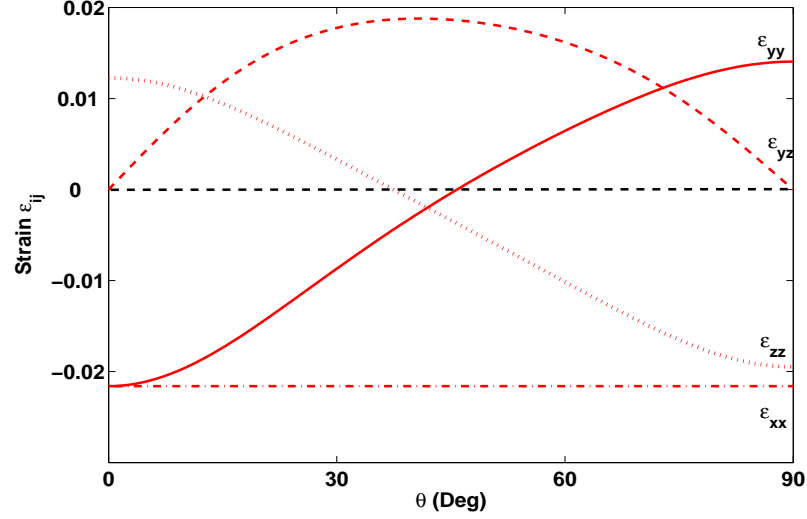


Figure 41: Elastic strain as a function of crystal orientation for bulk $\text{In}_{0.2}\text{Ga}_{0.8}\text{N}$.

In wurtzite crystals, the polar axis is parallel to the $[0001]$ direction, and the spontaneous polarization is along this direction. The spontaneous polarization along an arbitrary growth direction can then be estimated by a simple assumption shown below [146],

$$P_{sp} = p_{sp}^{(0001)} \cos \theta \quad (73)$$

where, $p_{sp}^{(0001)}$ is the value of the spontaneous polarization along $[0001]$ direction.

If piezoelectric crystals like wurtzite GaN are subjected to stress σ_{jk} , they develop polarization P_i that is proportional to applied stress i.e.,

$$P_i = d_{ijk} \sigma_{jk} \quad (74)$$

here, d_{ijk} are the piezoelectric moduli. According to Hooke's law, the applied stress is proportional to the strain and is given by,

$$\sigma_{ij} = c_{ijkl} \epsilon_{kl} \quad (75)$$

where, c_{ijkl} are the stiffness constants of the crystal. Owing to the symmetry properties of the tensors d_{ijk} and c_{ijkl} , it is possible to use the matrix or the Voigt notation instead of the tensor notation, where the second and third suffixes of d_{ijk} and the first two and last two suffixes of c_{ijkl} are abbreviated into a single suffix from 1 to 6 as shown below [135],

tensor notation	11	22	33	23,32	31,13	12,21
matrix notation	1	2	3	4	5	6

Thus equations (74) and (75) now become,

$$P_i = d_{ij}\sigma_j, \quad \sigma_i = c_{ij}\epsilon_j \quad (76)$$

where, $i=1, 2, 3$; and $j=1, 2, \dots, 6$. Using the correspondence between the matrix and tensor notations just described, the relations between polarization and strain can be expressed using arrays. Assuming that,

$$P_1 = P_x, \quad P_2 = P_y, \quad P_3 = P_z \quad (77)$$

$$\epsilon_1 = \epsilon_{xx}, \quad \epsilon_2 = \epsilon_{yy}, \quad \epsilon_3 = \epsilon_{zz}$$

$$\epsilon_4 = 2\epsilon_{yz}, \quad \epsilon_5 = 2\epsilon_{xz}, \quad \epsilon_6 = 2\epsilon_{xy} \quad (78)$$

Equation (76) becomes,

$$\begin{pmatrix} P_x \\ P_y \\ P_z \end{pmatrix} = \begin{pmatrix} 0 & 0 & 0 & 0 & d_{15} & 0 \\ 0 & 0 & 0 & d_{15} & 0 & 0 \\ d_{31} & d_{31} & d_{33} & 0 & 0 & 0 \end{pmatrix} \begin{pmatrix} c_{11} & c_{12} & c_{13} & 0 & 0 & 0 \\ c_{12} & c_{11} & c_{13} & 0 & 0 & 0 \\ c_{13} & c_{13} & c_{33} & 0 & 0 & 0 \\ 0 & 0 & 0 & c_{44} & 0 & 0 \\ 0 & 0 & 0 & 0 & c_{44} & 0 \\ 0 & 0 & 0 & 0 & 0 & c_{66} \end{pmatrix} \begin{pmatrix} \epsilon_{xx} \\ \epsilon_{yy} \\ \epsilon_{zz} \\ 2\epsilon_{yz} \\ 2\epsilon_{xz} \\ 2\epsilon_{xy} \end{pmatrix} \quad (79)$$

Hence,

$$\begin{pmatrix} P_x \\ P_y \\ P_z \end{pmatrix} = \begin{pmatrix} 2d_{15}C_{44}\epsilon_{xz} \\ 2d_{15}C_{44}\epsilon_{yz} \\ (d_{31}(C_{11} + C_{12}) + d_{33}C_{13})(\epsilon_{xx} + \epsilon_{yy}) + (2d_{31}C_{13} + d_{33}C_{33})\epsilon_{zz} \end{pmatrix} \quad (80)$$

The normal component of the piezoelectric polarization along the growth direction is given as [150],

$$P_{pe} = P_x \sin \theta + P_z \cos \theta \quad (81)$$

The parameters used in the calculation of the strain and polarization charges are listed in Table 7.

The spontaneous (P_{sp}) and the piezoelectric (P_{pe}) polarization charges calculated from (73) and (81) for the barrier (Figure 42a) and well (Figure 42b) region are plotted as a function of crystal orientation for a 3 nm $\text{In}_{0.2}\text{Ga}_{0.8}\text{N}/\text{GaN}$ SQW. Since GaN is assumed to be the substrate material for this structure, the piezoelectric polarization is zero in the barriers. The maximum values of the polarization charges occur at $\theta=0^\circ$ i.e., along [0001], while at $\theta=90^\circ$, which is the orientation of a- and m-plane structures, these charges are completely absent.

Figure 43 shows the crystal angle dependence of the net polarization charges at the well/barrier interface of a 3 nm $\text{In}_{0.2}\text{Ga}_{0.8}\text{N}/\text{GaN}$ SQW. The net polarization charge at the interface is calculated as $\Delta P = P_{tot}^b - P_{tot}^w$, where, $P_{tot}^b = P_{sp}^b + P_{pe}^b$ and $P_{tot}^w = P_{sp}^w + P_{pe}^w$. The subscript ‘b’ and ‘w’ denote barrier and well respectively. The maximum and minimum value of the net polarization occurs at $\theta=0^\circ$ and 90° . However, there is an additional zero-crossing point at $\theta \approx 58^\circ$. Although the spontaneous and piezoelectric charges at the well and barrier are non-zero, they cancel out each other at this angle. However, growth related issues could restrict the development of lasers along this crystal plane.

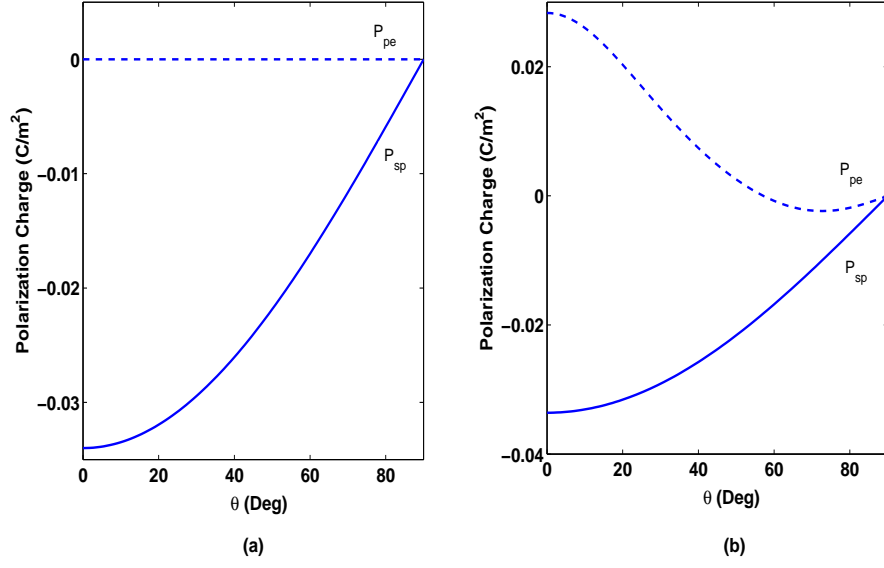


Figure 42: Spontaneous and piezoelectric polarization charges in (a) barrier and (b) well region of a 3 nm $\text{In}_{0.2}\text{Ga}_{0.8}\text{N}/\text{GaN}$ SQW as a function of crystal orientation.

Since the two main planes of growth for non-polar devices are the m- and a-planes, these two cases are considered here,

Case 1: a-plane $(11\bar{2}0)$ growth orientation with $\phi=0^\circ$ and $\theta=90^\circ$, the wavevectors can be written as,

$$\begin{aligned} K'_x &= k'_z, \\ K'_y &= k'_y, \\ K'_z &= -k'_x \end{aligned} \tag{82}$$

With the above wavevectors, the elements of the Hamiltonian in (68) become,

$$\begin{aligned} F' &= \Delta_1 + \Delta_2 + \lambda' + \theta', \\ G' &= \Delta_1 - \Delta_2 + \lambda' + \theta', \\ \lambda' &= \frac{\hbar^2}{2m_o} [A_1(-k'_x)^2 + A_2(k'^2_z + k'^2_y)] + D_1\epsilon_{zz} + D_2(\epsilon_{xx} + \epsilon_{yy}), \\ \theta' &= \frac{\hbar^2}{2m_o} [A_3(-k'_x)^2 + A_4(k'^2_z + k'^2_y)] + D_3\epsilon_{zz} + D_4(\epsilon_{xx} + \epsilon_{yy}), \end{aligned}$$

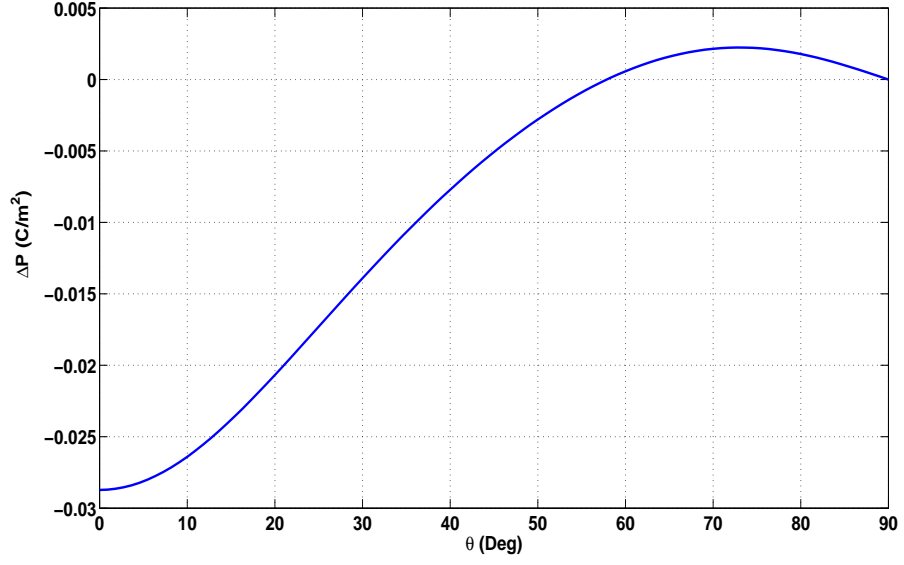


Figure 43: Crystal dependence of the net polarization charge $\Delta P = P_{tot}^b - P_{tot}^w$ at the well/barrier interface of a 3 nm $\text{In}_{0.2}\text{Ga}_{0.8}\text{N}/\text{GaN}$ SQW.

$$\begin{aligned}
 K' &= \frac{\hbar^2}{2m_o} A_5 (k'_z + ik'_y)^2 + D_5 \epsilon_+, \\
 H' &= \frac{\hbar^2}{2m_o} iA_6 (k'_z + ik'_y)(-k'_x) - A_7 (k'_z + ik'_y) + D_6 \epsilon_{z+}, \\
 I' &= \frac{\hbar^2}{2m_o} iA_6 (k'_z + ik'_y)(-k'_x) + A_7 (k'_z + ik'_y) + D_6 \epsilon_{z+},
 \end{aligned}$$

and,

$$\begin{aligned}
 \epsilon_{xx} &= \epsilon_1, \quad \epsilon_{yy} = -\frac{C_{12}\epsilon_1 + C_{13}\epsilon_2}{C_{11}}, \\
 \epsilon_{zz} &= \epsilon_2, \quad \epsilon_{yz} = 0,
 \end{aligned} \tag{83}$$

$$\epsilon_+ = \epsilon_1 + \frac{C_{12}\epsilon_1 + C_{13}\epsilon_2}{C_{11}}, \quad \epsilon_{z+} = 0$$

Case 2: m-plane with $\phi=30^\circ$ and $\theta=90^\circ$. The wavevectors become,

$$\begin{aligned}
 K'_x &= \frac{-1}{2}k'_y + \frac{\sqrt{3}}{2}k'_z, \\
 K'_y &= \frac{\sqrt{3}}{2}k'_y + \frac{1}{2}k'_z, \\
 K'_z &= -k'_x
 \end{aligned} \tag{84}$$

Table 7: Elastic stiffness and piezoelectric coefficients GaN and InN [154].

Parameters	GaN	InN
C_{11} (GPa)	390	223
C_{12} (GPa)	145	115
C_{13} (GPa)	106	92
C_{33} (GPa)	398	224
C_{44} (GPa)	105	48
d_{13} (pm V ⁻¹)	-1.0	-3.5
d_{33} (pm V ⁻¹)	1.9	7.6
d_{15} (pm V ⁻¹)	3.1	5.5

and the elements of the Hamiltonian become,

$$\begin{aligned}
F' &= \Delta_1 + \Delta_2 + \lambda' + \theta', \\
G' &= \Delta_1 - \Delta_2 + \lambda' + \theta', \\
\lambda' &= \frac{\hbar^2}{2m_o} [A_1(-k'_x)^2 + A_2(k'^2_z + k'^2_y)] + D_1\epsilon_{zz} + D_2(\epsilon_{xx} + \epsilon_{yy}), \\
\theta' &= \frac{\hbar^2}{2m_o} [A_3(-k'_x)^2 + A_4(k'^2_z + k'^2_y)] + D_3\epsilon_{zz} + D_4(\epsilon_{xx} + \epsilon_{yy}), \\
K' &= \frac{\hbar^2}{2m_o} A_5 \left\{ \frac{-1 - i\sqrt{3}}{2} k'^2_y + \frac{1 + i\sqrt{3}}{2} k'^2_z + (-\sqrt{3} + i) k'_y k'_z \right\} + D_5\epsilon_+, \\
H' &= \frac{\hbar^2}{2m_o} iA_6 \left\{ \frac{1 - i\sqrt{3}}{2} k'_x k'_y - \frac{\sqrt{3} + i}{2} k'_x k'_z \right\} - A_7 \left\{ \frac{-1 + i\sqrt{3}}{2} k'_y + \frac{\sqrt{3} + i}{2} k'_z \right\} + D_6\epsilon_{z+}, \\
I' &= \frac{\hbar^2}{2m_o} iA_6 \left\{ \frac{1 - i\sqrt{3}}{2} k'_x k'_y - \frac{\sqrt{3} + i}{2} k'_x k'_z \right\} + A_7 \left\{ \frac{-1 + i\sqrt{3}}{2} k'_y + \frac{\sqrt{3} + i}{2} k'_z \right\} + D_6\epsilon_{z+},
\end{aligned} \tag{85}$$

The elements of the strain tensor for m-plane remain unchanged and are given by (83).

The transition energy is plotted in Figure 44 as a function of crystal angle θ for a 3 nm In_{0.2}Ga_{0.8}N/GaN SQW. The transition energy in this case is defined as the energy difference between the first conduction and valence subbands at $|\bar{\mathbf{k}}| = 0$. The transition energy is independent of the basal plane angle ϕ , because at $|\bar{\mathbf{k}}| = 0$ the

elements of the $\mathbf{k}\cdot\mathbf{p}$ Hamiltonian are only functions of strain and polarization charges, both of which depend on the θ according to the formulation presented previously.

The transition energy for c-plane structures is significantly smaller than the m- and a-plane structures. This is significant because it is technologically more difficult to grow ternary InGaN with In-rich materials, and offers at least a small incentive to exploit the QCSE to achieve lasing with material which is easier to grow. The m- and a-plane QWs are associated with zero polarization charges at the interfaces and hence their transition energies are blue shifted compared to the c-plane structures.

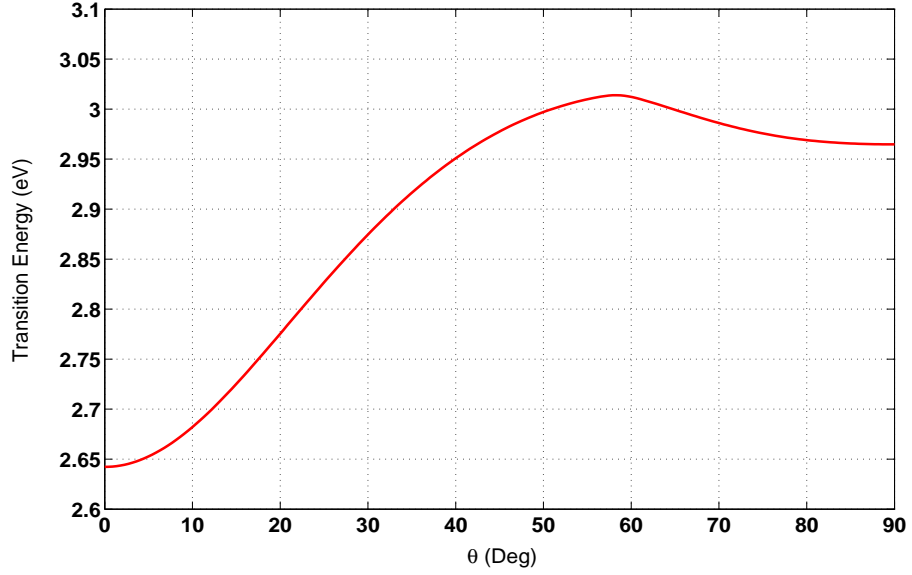


Figure 44: Transition energy between the first conduction and valence bands as a function of crystal orientation angle of a 3 nm $\text{In}_{0.2}\text{Ga}_{0.8}\text{N}/\text{GaN}$ SQW.

The valence band dispersion for bulk $\text{In}_{0.2}\text{Ga}_{0.8}\text{N}$ is illustrated in Figure 45 for (a) c-, (b) m-, and (c) a-planes. Macroscopic polarization charges are not included in the bulk dispersion calculations. From the figure, it is seen that the dispersion becomes more anisotropic in the k'_x - k'_y plane with increasing crystal angles, but the HH bands retain their nearly parabolic shape along k'_x for all the crystal orientations. Along k'_y , the coupling between the LH and CH bands is significantly reduced for

the non-polar orientations. Additionally, in the k'_x -direction, the elements of the $\mathbf{k} \cdot \mathbf{p}$ Hamiltonian for the m- and a-planes are identical, and hence, the dispersion curves along this direction are also the same. The energy bands for m- and a-planes are shifted upwards with respect to the c-plane, and this may be attributed to the effect of uniaxial strain.

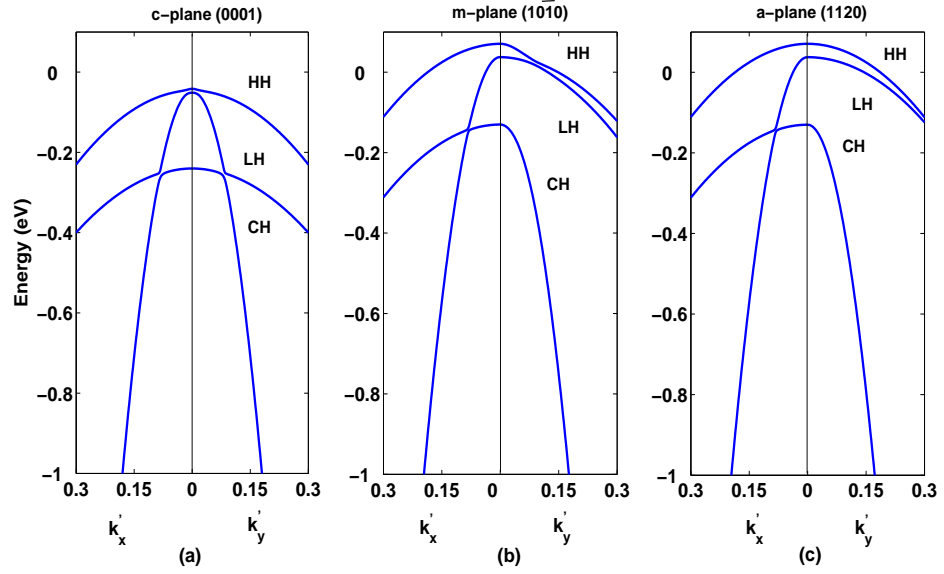


Figure 45: Valence band dispersion for bulk $\text{In}_{0.2}\text{Ga}_{0.8}\text{N}$ for (a) c-, (b) m-, and (c) a-planes.

Figure 46 shows the valence band dispersion for a 3 nm $\text{In}_{0.2}\text{Ga}_{0.8}\text{N}/\text{GaN}$ SQW for (a) c-, (b) m-, and (c) a-planes. Thirty Fourier coefficients have been used in the quantum well calculations, resulting in sixty one plane waves. One hundred points are used in the k -space discretization. The substrate material is assumed to be GaN and the barriers are lattice matched to the substrate. The GaN barriers are 4 nm wide.

The naming of the valence subbands at the Γ point is dependent on the dominant composition of the coefficients of the wavefunctions in terms of $|X'\rangle$, $|Y'\rangle$, and $|Z'\rangle$ [148]. If $g_m^{(i)}$'s are the coefficients of the i^{th} wavefunctions, then components that

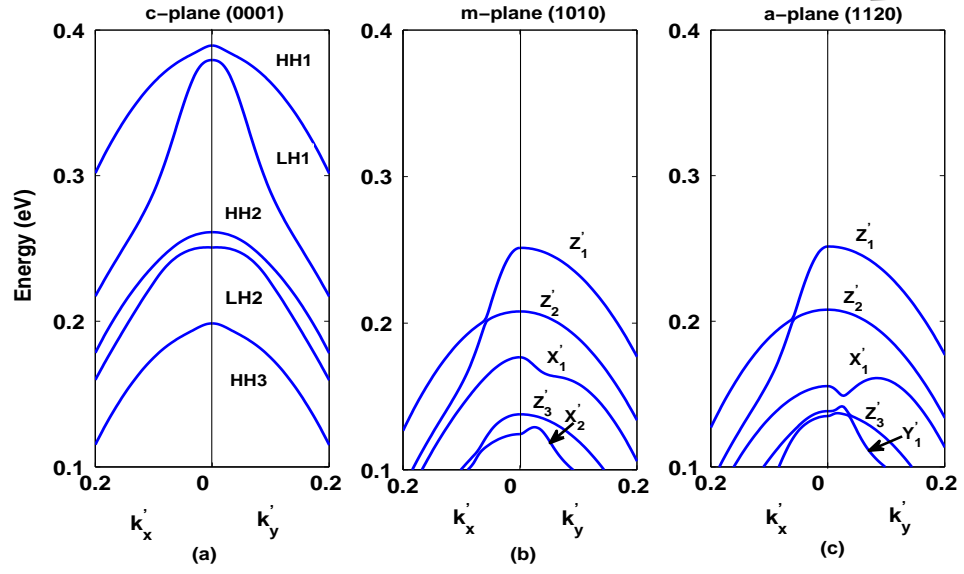


Figure 46: Valence band dispersion of a 3 nm $\text{In}_{0.2}\text{Ga}_{0.8}\text{N}/\text{GaN}$ SQW. (a) c-, (b) m-, and (c) a-planes.

define the subbands are given as,

$$P_m^{X'} = \frac{\langle g_m^{(2)} - g_m^{(1)} | g_m^{(2)} - g_m^{(1)} \rangle + \langle g_m^{(4)} - g_m^{(5)} | g_m^{(4)} - g_m^{(5)} \rangle}{2}$$

$$P_m^{Y'} = \frac{\langle g_m^{(2)} + g_m^{(1)} | g_m^{(2)} + g_m^{(1)} \rangle + \langle g_m^{(4)} + g_m^{(5)} | g_m^{(4)} + g_m^{(5)} \rangle}{2} \quad (86)$$

and

$$P_m^{Z'} = \langle g_m^{(3)} | g_m^{(3)} \rangle + \langle g_m^{(6)} | g_m^{(6)} \rangle$$

Accordingly, the topmost valence subband for m- and a-plane quantum wells is $|Z'\rangle$ -like.

The valence band dispersion becomes anisotropic for the m- and a-plane quantum wells, which is the same trend that is seen for the bulk case (Figure 45). This also results in an anisotropy in the in-plane optical matrix elements [149, 147].

Because of the non-polar nature of the m- and a-plane QW structures, the polarization-induced built-in fields are zero, and hence, quantum confined Stark effects are significantly reduced, resulting in a blue shift of the transition energy between the first conduction and valence subbands (also see Figure 44).

Another advantage of designing laser diodes on non-polar m- and a-planes may be best understood by plotting the spatial variation of the band edges and envelope functions. The conduction and valence band edges and envelope functions for the first conduction and valence subbands are displayed for three crystal angles, namely, $\theta=0^\circ$ (Figure 47), $\theta=45^\circ$ (Figure 48), and $\theta=90^\circ$ (Figure 49). The in-plane angle is set at $\phi=0^\circ$. The active region consists of a 3 nm $\text{In}_{0.2}\text{Ga}_{0.8}\text{N}$ SQW with 4 nm wide GaN barriers. The barriers are assumed to be lattice matched to the substrate.

Owing to the maximum net polarization charge at the well/barrier interfaces at $\theta=0^\circ$, the spatial separation of the electron and hole envelope functions is the highest, thereby, considerably reducing the transition probabilities and degrading the luminescence efficiencies [50].

At $\theta=45^\circ$, the net polarization charge at the interfaces is reduced to about 18% of the maximum value. Although the band edges resemble nearly flat band conditions, the spatial separation of the conduction and valence envelope functions is still high enough to cause suboptimal emission efficiencies.

The conduction and valence band edges attain flat band conditions at $\theta=90^\circ$ because of zero net polarization charge at the interfaces, and the electron and hole envelope functions now have maximum overlap. It is expected that laser diodes designed on non-polar m- and a-planes will enable lower radiative lifetimes, increased luminescence efficiencies [207], and higher optical gain compared to c-axis designs [225, 145, 146].

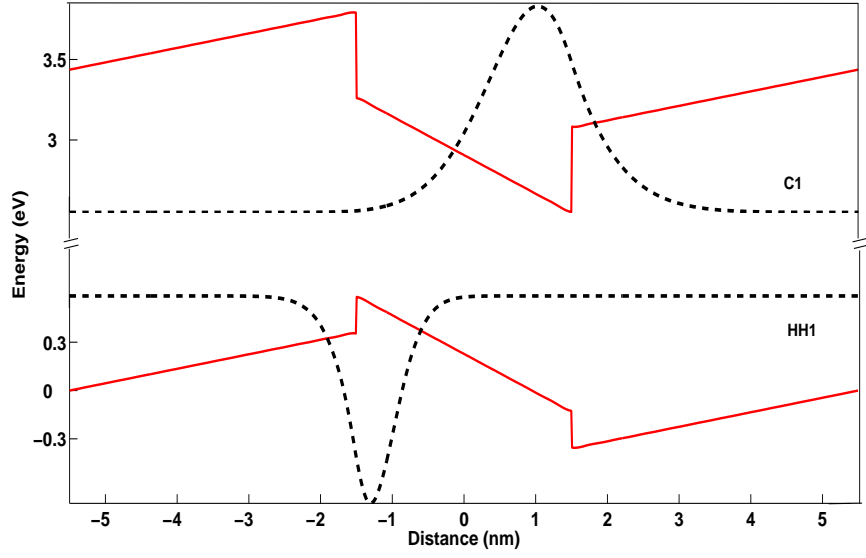


Figure 47: Conduction and valence band edges and envelope functions of the first conduction and heavy hole bands of a 3 nm $\text{In}_{0.2}\text{Ga}_{0.8}\text{N}/\text{GaN}$ SQW at $\theta=0^\circ$.

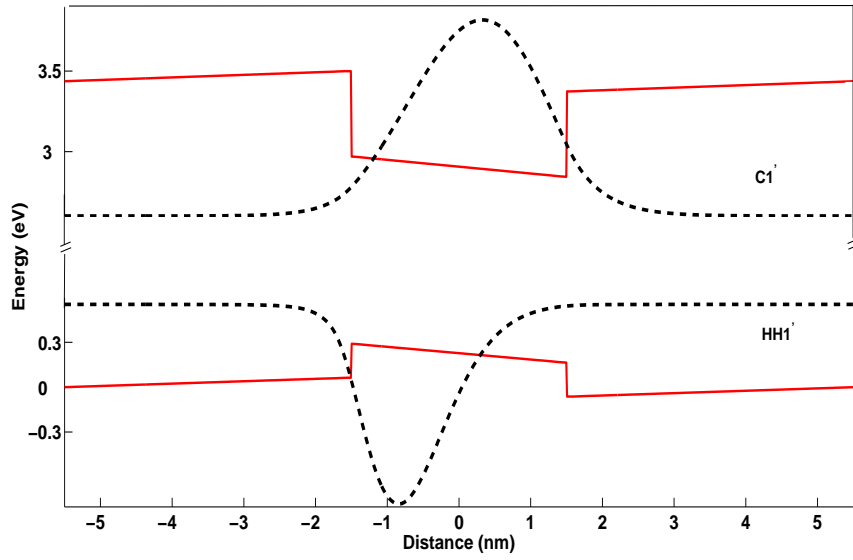


Figure 48: Conduction and valence band edges and envelope functions of the first conduction and heavy hole bands of a 3 nm $\text{In}_{0.2}\text{Ga}_{0.8}\text{N}/\text{GaN}$ SQW at $\theta=45^\circ$.

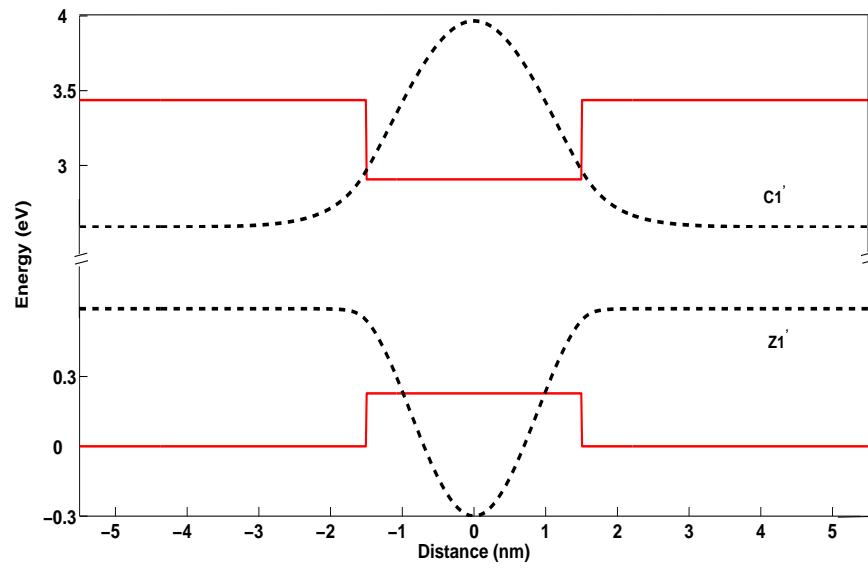


Figure 49: Conduction and valence band edges and envelope functions of the first conduction and heavy hole bands of a 3 nm $\text{In}_{0.2}\text{Ga}_{0.8}\text{N}/\text{GaN}$ SQW at $\theta=90^\circ$.

CHAPTER VII

DESIGN STRATEGIES FOR INGAN-BASED GREEN LASERS

7.1 Optimization of TE optical gain

Green laser diodes are a challenge to designers because of the problems associated with the high indium content needed in the active regions [64]. To date the longest reported emission wavelength for InGaN-based laser diodes is 485 nm [96].

This chapter explores design strategies for $\text{In}_x\text{Ga}_{1-x}\text{N}$ -based green quantum well lasers [203]. A combination of design parameters is described that would maximize the gain spectral density at a target wavelength of 525 nm and the factors which limit its magnitude are discussed. Additionally, sensitivity analysis has been performed to assess the two most influential parameters that affect the gain spectral density at 525 nm and identify other design parameters to which this result is insensitive. Previously reported theoretical analysis of gain in QW LDs has assumed the absence of strain within the barrier layers [42, 66, 34]. This assumption is justified in the special cases of 1) pure binary GaN barrier material in a design grown on thick GaN buffer [42, 66], or 2) ternary barrier material in a design grown on a sufficiently thick comparable ternary material in order to largely relax the in-plane strain [34]. This chapter provides a comparative analysis of the significance of the choice of buffer layer material as it affects strain in the active region.

The electronic states are calculated using the Fourier-space $\mathbf{k}\cdot\mathbf{p}$ model described in Chapter 4. Thirty Fourier coefficients are used in the bandstructure calculation, resulting in sixty-one plane waves and one hundred points are used in the discretization of the \mathbf{k} -space. Spontaneous and piezoelectric polarization charges are included

in the calculations according to equation (50)-(53). Binary material parameters are taken from [154, 157].

To gain insight into the effect of quantum well width on the optical characteristics of an $\text{In}_x\text{Ga}_{1-x}\text{N}$ -based single quantum well (SQW), the transition energy between the first conduction and heavy hole subband has been calculated and is shown in Figure 50 as a function of well width for two mole fractions of ternary well material.

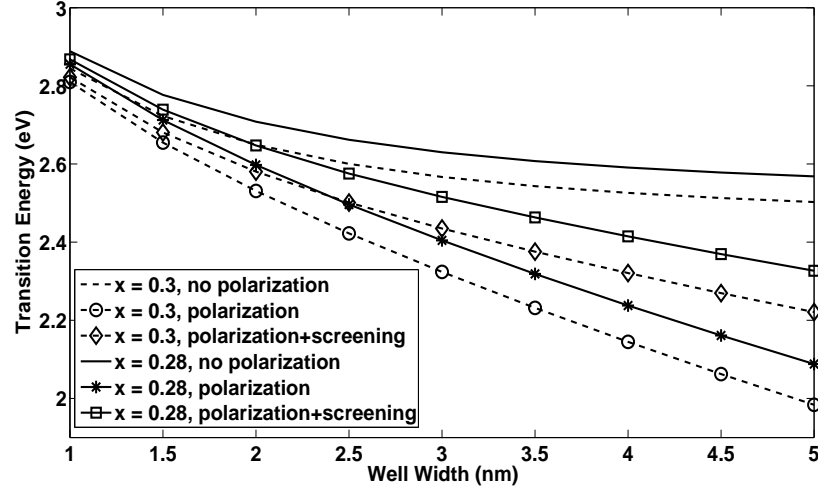


Figure 50: Transition energy as a function of well width for 28% and 30% indium mole fractions in the well. The barrier material is $\text{In}_{0.06}\text{Ga}_{0.94}\text{N}$ and the barrier width is 13.4 nm. The carrier density is $3 \times 10^{19} \text{ cm}^{-3}$.

In the absence of spontaneous and piezoelectric polarization charges at the hetero-interfaces, there is very little variation in the transition energy with increasing well widths (solid and dashed curves in Figure 50 denotes this case). This trend changes in the presence of the macroscopic polarization charges at the interface (star and circle symbols in Figure 50). In InGaN -based quantum well structures, the net spontaneous polarization charge at the interfaces is negligible even with increasing indium mole fractions in the well. On the other hand, for a given well width, with an increase in the well indium mole fraction, the wells are more strained as there is a greater lattice mismatch between the well and the substrate layers. This increases the net

piezoelectric polarization charge at the interfaces and results in an increase in the magnitude of the polarization-induced built-in electric fields. These fields are responsible for QCSE, leading to a red shift in the transition energy [191]. The QCSE is more pronounced at larger well widths, which exhibits even greater shift in transition energy.

QW carrier density used in the simulations is $3 \times 10^{19} \text{ cm}^{-3}$, which are the values typically used in nitride-based QW laser simulations. These charges screen the polarization fields, thereby resulting in a blue shift in the transition energy (square and diamond symbols in Figure 50). However, screening is only partial and the transition energies never attain their flatband values.

In Figure 51 the fundamental optical transition energy is shown as a function of indium barrier mole fraction for an $\text{In}_{0.3}\text{Ga}_{0.7}\text{N}/\text{In}_x\text{Ga}_{1-x}\text{N}$ SQW for four different well widths. Macroscopic polarization charges are included in the calculations. For a given indium barrier mole fraction, the transition energy is demonstrated to decrease with increasing well width (also see Figure 50).

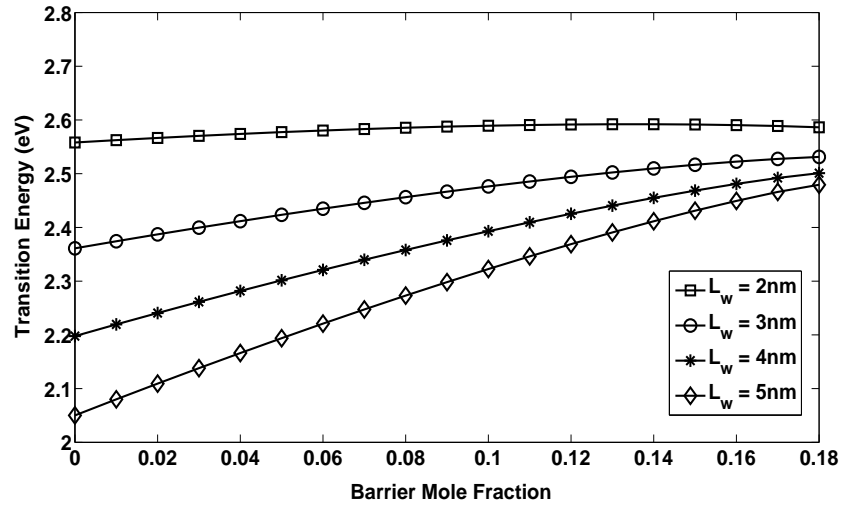


Figure 51: Transition energy versus the barrier $\text{In}_x\text{Ga}_{1-x}\text{N}$ mole fraction for different quantum well widths.

With well thickness held constant, if the indium barrier mole fraction is increased,

the lattice mismatch between the well and the barrier may be reduced. This leads to a reduction in the magnitude of polarization charges at the interfaces, which in turn gives rise to lower polarization-induced built-in electric fields. The result is a blue shift in the optical transition energy with increasing indium barrier mole fraction. Because of the interplay of the polarization charges at the interfaces, increasing the well and barrier mole fractions has a qualitatively opposite effect on the fundamental transition energy.

Figure 52 shows the wavelength dependence of the TE optical gain as a function of (a) well indium mole fraction, (b) barrier indium mole fraction, (c) well width, and (d) barrier width. For this case, an $\text{In}_{0.32}\text{Ga}_{0.68}\text{N}/\text{In}_{0.04}\text{Ga}_{0.96}\text{N}$ SQW with $L_w=2.9$ nm and $L_b=14.4$ nm is taken as the reference design (solid curve in each subfigure). Each of the design parameter (well/barrier width and indium mole fraction) is then varied about the reference value to demonstrate its effect on the transition wavelength and TE optical gain. Increasing the well indium mole fraction and/or the well width increases the lasing wavelength and decreases the gain, while increasing the barrier indium mole fraction displays the opposite effect. The barrier width has a lesser influence on the optical gain and transition wavelength.

To elaborate upon the point presented in the previous paragraph, TE optical gain as a function of wavelength is shown in Figure 53 for combination of well indium mole fraction and well width, keeping the barrier composition and barrier width unchanged. The barrier material here is GaN and $L_b = 12.4$ nm. Since the well indium mole fraction and width have a qualitatively similar effect on the transition wavelength, adjusting the two would result in a gain spectral density peak at 525 nm. The highest value of gain in this case occurs for a design with the smallest well width. This can be attributed to the significantly lower polarization-induced spatial separation of the electron and hole wavefunction for smaller well width.

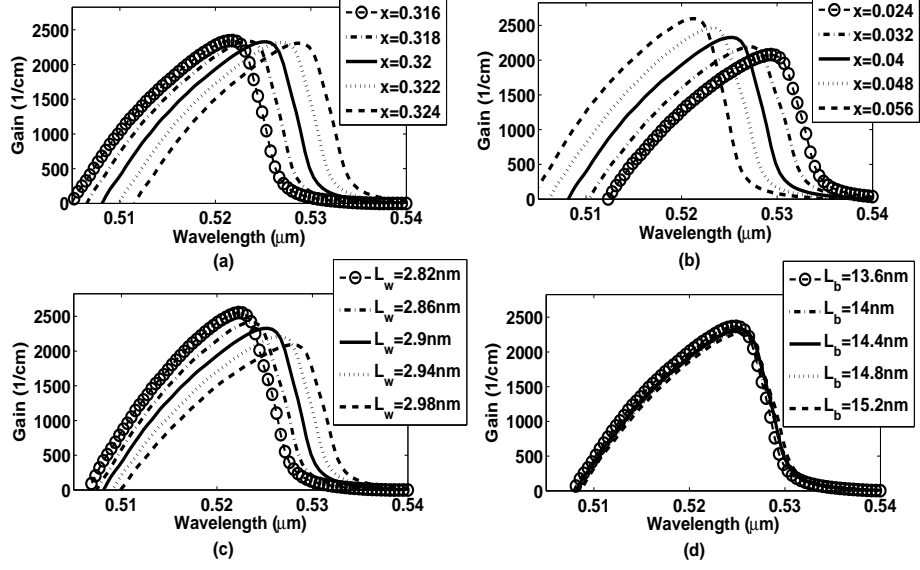


Figure 52: TE optical gain as a function of wavelength for (a) varying indium well mole fraction, (b) varying indium barrier mole fraction, (c) varying well width, and (d) varying barrier width. The charge density is $N = 3 \times 10^{19} \text{ cm}^{-3}$.

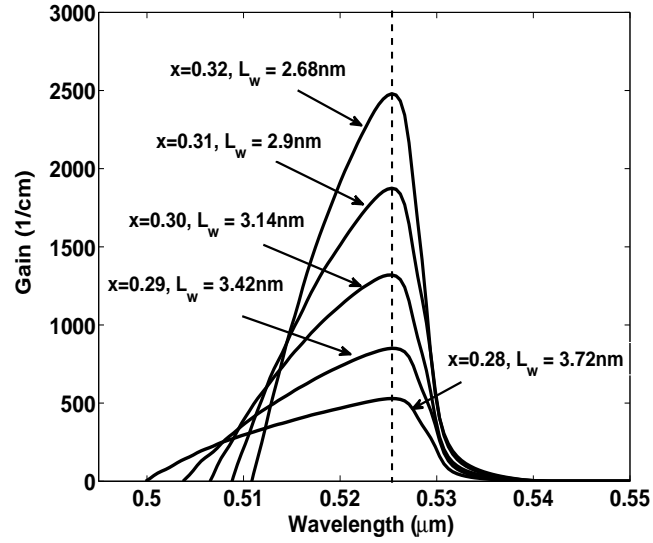


Figure 53: TE optical gain as a function of wavelength for combination of indium well mole fraction and well width. The charge density is $N = 3 \times 10^{19} \text{ cm}^{-3}$. The barrier material is GaN and $L_b = 12.4 \text{ nm}$.

Maximum gain spectral density at 525 nm may also be achieved with a combination of two or more design parameters such as the well/barrier widths and indium

mole fractions as shown in Figure 54. Among the designs considered, the highest value of gain is obtained for the design with the largest indium mole fraction in the well and the smallest well width. This design is an $\text{In}_{0.32}\text{Ga}_{0.68}\text{N}/\text{GaN}$ SQW with $L_w=2.62$ nm and $L_b=14.4$ nm (curve (a) in Figure 54). Although higher indium mole fractions in the well regions are associated with higher polarization-induced electric fields, decreasing the well width provides better carrier confinement in the well. This increased confinement by thinner wells outweighs the detrimental effects of the polarization-induced fields, thereby resulting in higher gain. This is evident in Figure 53 and Figure 54a. Material growth issues may also limit the amount of indium that can be used [64], making alternative design strategies highly desirable.

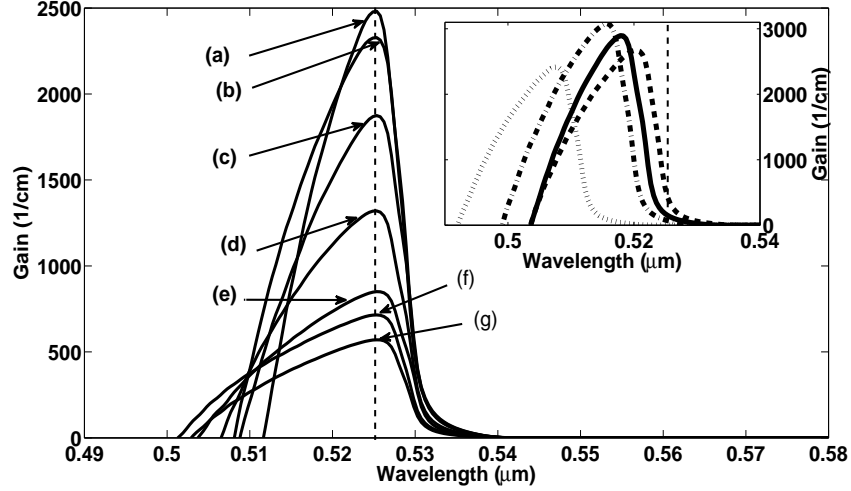


Figure 54: TE optical gain as a function of wavelength. The charge density is $N = 3 \times 10^{19} \text{ cm}^{-3}$. (a) $L_w=2.62\text{nm}$, $L_b=14.4\text{nm}$ $\text{In}_{0.32}\text{Ga}_{0.68}\text{N}/\text{GaN}$, (b) $L_w=2.9\text{nm}$, $L_b=14.4\text{nm}$ $\text{In}_{0.32}\text{Ga}_{0.68}\text{N}/\text{In}_{0.04}\text{Ga}_{0.96}\text{N}$, (c) $L_w=2.9\text{nm}$, $L_b=12.4\text{nm}$ $\text{In}_{0.31}\text{Ga}_{0.69}\text{N}/\text{GaN}$, (d) $L_w=3.14\text{nm}$, $L_b=12.4\text{nm}$ $\text{In}_{0.3}\text{Ga}_{0.7}\text{N}/\text{GaN}$, (e) $L_w=3.42\text{nm}$, $L_b=12.4\text{nm}$ $\text{In}_{0.29}\text{Ga}_{0.71}\text{N}/\text{GaN}$, (f) $L_w=3.65\text{nm}$, $L_b=12.4\text{nm}$ $\text{In}_{0.29}\text{Ga}_{0.71}\text{N}/\text{In}_{0.02}\text{Ga}_{0.98}\text{N}$, and (g) $L_w=3.72\text{nm}$, $L_b=12.4\text{nm}$ $\text{In}_{0.28}\text{Ga}_{0.72}\text{N}/\text{GaN}$. Inset: Optical gain as a function of wavelength. The charge density is $N = 3 \times 10^{19} \text{ cm}^{-3}$. Solid curve: $L_w=2.7\text{nm}$, $L_b=14.4\text{nm}$ $\text{In}_{0.32}\text{Ga}_{0.68}\text{N}/\text{In}_{0.04}\text{Ga}_{0.96}\text{N}$, Dashed curve: $L_w=2.9\text{nm}$, $L_b=14.4\text{nm}$ $\text{In}_{0.32}\text{Ga}_{0.68}\text{N}/\text{In}_{0.06}\text{Ga}_{0.94}\text{N}$, Dotted curve: $L_w=2.9\text{nm}$, $L_b=14.4\text{nm}$ $\text{In}_{0.3}\text{Ga}_{0.7}\text{N}/\text{In}_{0.04}\text{Ga}_{0.96}\text{N}$, Dotted-dashed curve: $L_w=2.9\text{nm}$, $L_b=14.4\text{nm}$ $\text{In}_{0.32}\text{Ga}_{0.68}\text{N}/\text{In}_{0.08}\text{Ga}_{0.92}\text{N}$.

A peak in the gain spectral density at 525 nm may also be obtained with smaller indium mole fractions, through careful selection of design parameters. One such configuration is an $\text{In}_{0.28}\text{Ga}_{0.72}\text{N}/\text{GaN}$ SQW with $L_w=3.72$ nm and $L_b=12.4$ nm (curve (g)). Nevertheless, it is evident that this design shows significantly lower gain. This may be attributed to the fact that the polarization-induced spatial separation of electron and hole wavefunctions is directly proportional to the well width, which exerts direct influence on the optical matrix element. Thus, by judicious choice of design parameters, it is possible to partially compensate for material growth related limitations on indium content, and achieve peak gain spectral density at the desired wavelength.

Layer thicknesses and material composition both play important roles in determining not only the gain but also the gain roll-off near 525 nm. As an example, the TE optical gain as a function of wavelength is shown in the inset of Figure 54 for four combinations of design parameters. Increased indium barrier mole fraction causes a blue shift in the gain curve and significantly reduces the available gain at 525 nm (dot-dashed and dashed curves in the inset plot). The gain peak shifts to smaller wavelength for lower indium well mole fractions (dotted curve). This is a direct consequence of the fact that the bandgap and hence the wavelength are related to the indium mole fraction. Narrower wells (solid curve) also cause a blue shift in the gain curve, degrading the gain at 525 nm.

For purposes of sensitivity analysis, design (b) of Figure 54 is taken as a reference. Each of the four design parameters (well/barrier mole fractions and widths) is varied while keeping the other three constant at their reference values. Our analysis reveals that the well and barrier mole fractions play the greatest role in determining the gain, while the barrier width is the least influential design parameter. Figure 55 shows contours of the optical gain at 525 nm as a function of the well and barrier mole fractions. The lasing wavelength for most of these curves is shifted from 525 nm.

In situations where choice of material composition is constrained by growth-related issues, gain contours provide insight, which may be used as a guide to design when compromise becomes necessary.

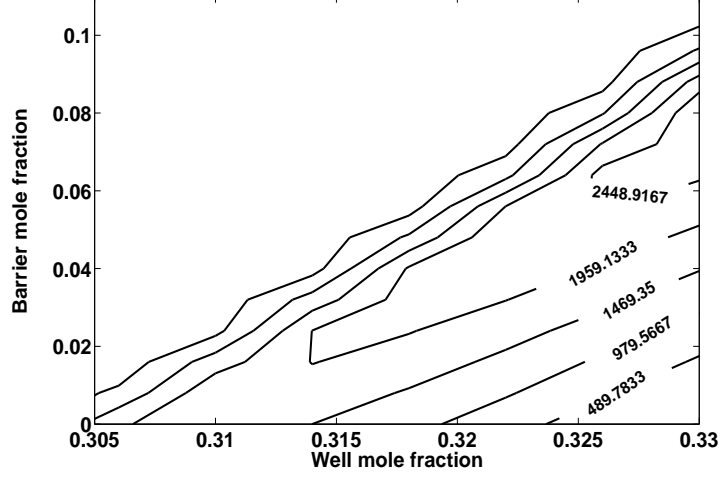


Figure 55: TE optical gain contours at a wavelength of 525 nm as a function of well and barrier mole fraction. The charge density is $N = 3 \times 10^{19} \text{ cm}^{-3}$. The well and barrier widths are $L_w = 2.9 \text{ nm}$ and $L_b = 14.4 \text{ nm}$.

Each of the results presented above were calculated with strain in the barriers taken into account under the assumption of biaxial compressive strain consistent with the in-plane lattice constant of bulk GaN. Figure 56(a) shows the variation of the in-plane component of strain as a function of indium mole fraction in the barrier material. The well indium mole fraction is 30% and $L_w = 2.9 \text{ nm}$ and $L_b = 13.4 \text{ nm}$. As the mole fraction increases, the barriers are subjected to increasing strain, causing the piezoelectric charge to increase. Hence the net polarization charge at the well-barrier interface decreases, leading to a reduction in the magnitude of the built-in fields in the barrier and well regions according to (53), as shown in Figure 56(b).

The most significant effect of strain in the barrier is observed when the fundamental optical transition energy is plotted as a function of barrier mole fraction for

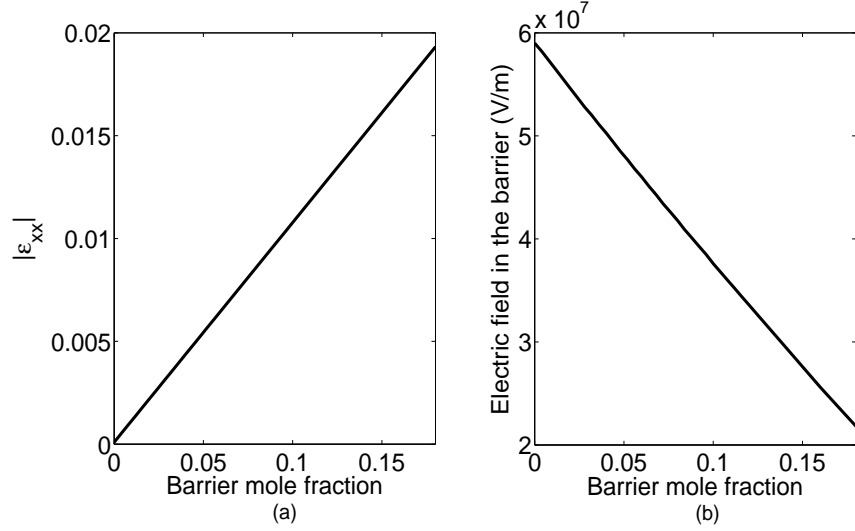


Figure 56: ((a) in-plane component of strain as a function of barrier mole fraction. (b) Polarization-induced built-in electric field in the barrier regions as a function of barrier mole fraction. The well indium mole fraction is 30% and $L_w = 2.9$ nm and $L_b = 13.4$ nm.

strained and unstrained barriers (shown in Figure 57). Such situations are of practical interest when buffer layer material may be considered a design parameter. The well and barrier widths are 2.9 nm and 13.4 nm respectively, and the well mole fraction is 30% indium. The general trend in the transition energy essentially remains the same, i.e., as the barrier mole fraction is increased, the transition energy is blue shifted. However, for a given barrier mole fraction, strained barriers may be associated with somewhat lower built-in polarization fields in the active region, giving rise to higher values of the fundamental optical transition energy compared to the case of unstrained barriers.

Figure 58 shows the transition energy as a function of well width for an $\text{In}_{0.3}\text{Ga}_{0.7}\text{N}/\text{In}_{0.06}\text{Ga}_{0.94}\text{N}$ SQW with strained and unstrained barriers. For a given well width, there is very little difference between the polarization charges at the well-barrier interface for the strained and unstrained cases. This explains why there is only a small change in the transition energy in Figure 58 for any fixed well width.

In Figure 59, the optical gain spectrum is shown as a function of wavelength for

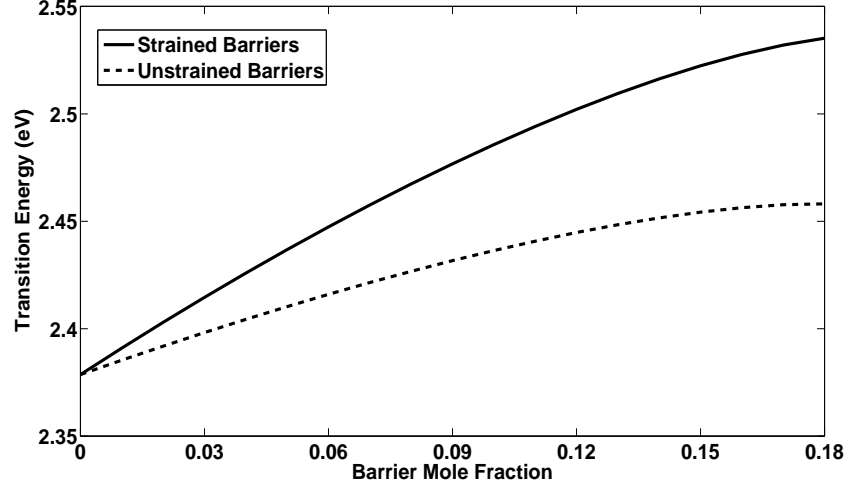


Figure 57: Transition energy versus the barrier $\text{In}_x\text{Ga}_{1-x}\text{N}$ mole fraction for a 2.9 nm $\text{In}_{0.3}\text{Ga}_{0.7}\text{N}$ SQW with strained and unstrained barriers.

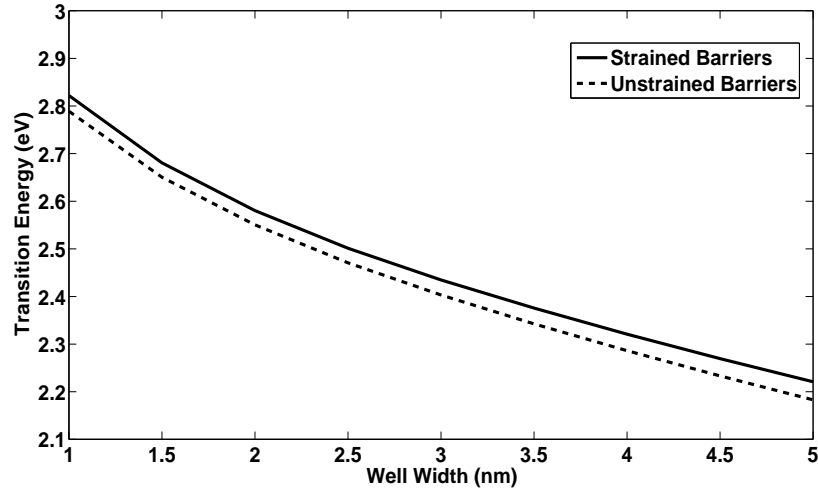


Figure 58: Transition energy versus well width in $\text{In}_{0.3}\text{Ga}_{0.7}\text{N}/\text{In}_{0.06}\text{Ga}_{0.94}\text{N}$ SQW with strained and unstrained barriers. The barriers are 13.4 nm wide.

the case of unstrained barriers. Even under the assumption of unstrained barriers, the same design trends for optical gain spectrum hold true i.e., the highest gain value occurs for the design with the largest indium well mole fractions (curve (a)). Keeping the barrier composition and width unchanged, the gain can be manipulated to exhibit a peak at 525 nm with various combinations of indium mole fraction in the well and

well width (curves (d) and (e)). The inset plot in Figure 59 shows the same trend in gain roll-off at 525 nm as was the case for strained barriers.

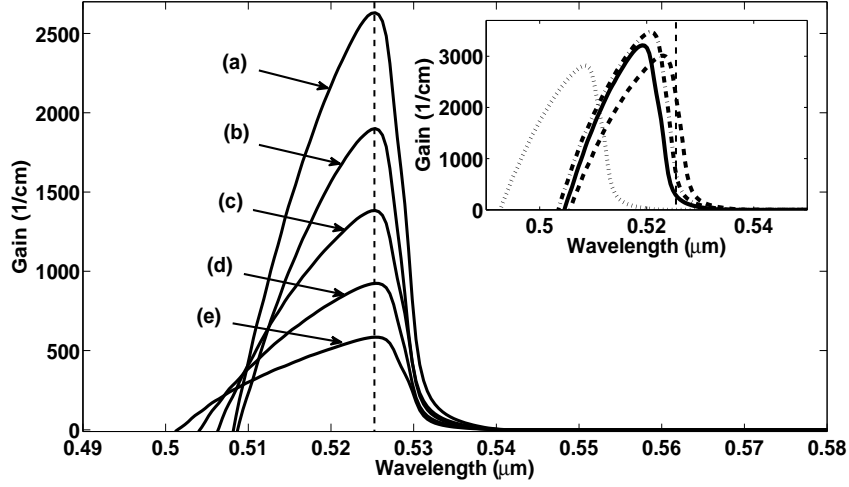


Figure 59: TE optical gain as a function of wavelength. The charge density is $N = 3 \times 10^{19} \text{ cm}^{-3}$. (a) $L_w=2.9\text{nm}$, $L_b=14\text{nm}$ $\text{In}_{0.32}\text{Ga}_{0.68}\text{N}/\text{In}_{0.07}\text{Ga}_{0.93}\text{N}$, (b) $L_w=2.9\text{nm}$, $L_b=14.4\text{nm}$ $\text{In}_{0.31}\text{Ga}_{0.69}\text{N}/\text{In}_{0.01}\text{Ga}_{0.99}\text{N}$, (c) $L_w=3.14\text{nm}$, $L_b=14.4\text{nm}$ $\text{In}_{0.3}\text{Ga}_{0.7}\text{N}/\text{In}_{0.01}\text{Ga}_{0.99}\text{N}$, (d) $L_w=3.4\text{nm}$, $L_b=15.2\text{nm}$ $\text{In}_{0.29}\text{Ga}_{0.71}\text{N}/\text{In}_{0.01}\text{Ga}_{0.99}\text{N}$, and (e) $L_w=3.7\text{nm}$, $L_b=15.2\text{nm}$ $\text{In}_{0.28}\text{Ga}_{0.72}\text{N}/\text{In}_{0.01}\text{Ga}_{0.99}\text{N}$. Inset: Optical gain as a function of wavelength. The charge density is $N = 3 \times 10^{19} \text{ cm}^{-3}$. Solid curve: $L_w=2.7\text{nm}$, $L_b=14\text{nm}$ $\text{In}_{0.32}\text{Ga}_{0.68}\text{N}/\text{In}_{0.07}\text{Ga}_{0.93}\text{N}$, Dashed curve: $L_w=2.9\text{nm}$, $L_b=14\text{nm}$ $\text{In}_{0.32}\text{Ga}_{0.68}\text{N}/\text{In}_{0.09}\text{Ga}_{0.91}\text{N}$, Dotted curve: $L_w=2.9\text{nm}$, $L_b=14\text{nm}$, $\text{In}_{0.3}\text{Ga}_{0.7}\text{N}/\text{In}_{0.07}\text{Ga}_{0.93}\text{N}$, Dotted-dashed curve: $L_w=2.9\text{nm}$, $L_b=14\text{nm}$, $\text{In}_{0.32}\text{Ga}_{0.68}\text{N}/\text{In}_{0.11}\text{Ga}_{0.89}\text{N}$.

Sensitivity analysis is also performed for the case of unstrained barriers, and it is found that the optical gain spectrum is most sensitive to the well and barrier mole fractions and is least sensitive to the barrier width. The contours of the optical gain at 525 nm for different indium well and barrier mole fractions are shown in Figure 60 and are similar to the case of strained barriers.

From the plots in Figure 57, the transition energy is blue shifted with strain in the barriers. So for the barriers that are under strain, one can expect the gain peak to occur at lower wavelengths compared to unstrained barriers. Also due to reduced built-in electric fields at the barriers, the magnitude of the gain peak will also be high

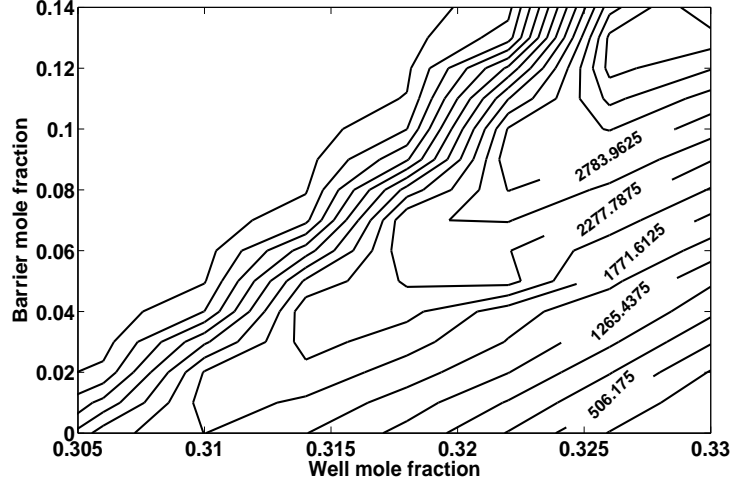


Figure 60: Contours of the TE optical gain at 525 nm as a function of well and barrier mole fraction. The charge density is $N = 3 \times 10^{19} \text{ cm}^{-3}$. The well and barrier widths are $L_w = 2.9 \text{ nm}$ and $L_b = 14 \text{ nm}$.

in the case of strained barriers. Figure 61 shows this effect of strain on the gain peak and lasing wavelength for a 2.9 nm $\text{In}_{0.32}\text{Ga}_{0.68}\text{N}/\text{In}_{0.04}\text{Ga}_{0.96}\text{N}$ SQW structure.

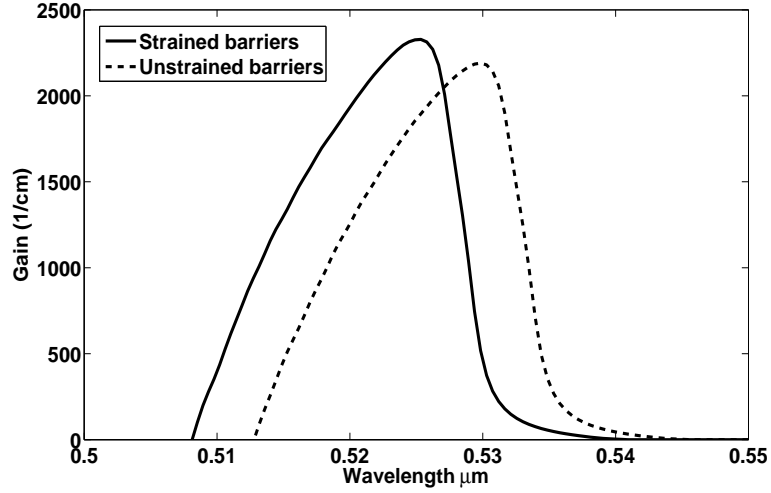


Figure 61: TE optical gain as a function of wavelength in a 2.9 nm $\text{In}_{0.32}\text{Ga}_{0.68}\text{N}/\text{In}_{0.04}\text{Ga}_{0.96}\text{N}$ SQW. The barriers are 14.4 nm wide. The charge density is $N = 3 \times 10^{19} \text{ cm}^{-3}$.

CHAPTER VIII

CONCLUSION AND FUTURE RESEARCH DIRECTIONS

8.1 Conclusion

8.1.1 Electrothermal simulation of AlGa_N/Ga_N HEMTs

In chapter III, the effect of hot phonons on the temperature distribution in AlGa_N/Ga_N HEMTs was investigated. It was found that the decay of the non-equilibrium longitudinal optical phonons into acoustic phonons in conjunction with the direct emission of acoustic phonons by the channel electrons contributed to the rise in the acoustic phonon temperature of sufficient magnitude to degrade drain current in a HEMT under normal operating conditions. Substrate material and dimension also played an important role in controlling the peak temperature throughout the device. SiC, featuring the highest thermal conductivity among available substrate materials, was most effective in transporting the heat toward the heat sink located at the bottom of the substrate. We believe that the electrothermal solver presented in this thesis coupled with the ensemble Monte Carlo simulator may be able to predict the electrical and thermal characteristics of nitride-based HFETs.

8.1.2 Simulation of InGa_N-based quantum well lasers

With the aim of developing a tool to simulate nitride-based lasers, the electronic part of MINILASE was extended to include nitride materials and models. From the bulk and quantum well dispersion it was found that unlike in arsenide-based structures, the strain in nitride layers does not significantly change the shape of the dispersion curves, and merely shifts the energy values.

However, the presence of macroscopic polarization charges at the heterointerfaces induced built-in electric fields that caused red-shifts in the transition energies owing

to quantum confined Stark effects. These charges also reduced the electron-hole wavefunction overlap, thereby, leading to lower optical gain.

The formulation of the k.p Hamiltonian for non-polar crystal orientation planes was presented in chapter VI. a- and m-planes have no polarization charges along the growth directions and hence these growth planes may offer opportunities for the fabrication of optoelectronic devices having superior performance.

8.1.3 Design of InGaN-based green lasers

In chapter VII, some design strategies for green InGaN-based lasers were outlined. For operation in the green portion of the spectrum, it was demonstrated that strain engineering may partially ameliorate much of the deleterious influence of built-in polarization fields found in wurtzite III-nitride laser diodes.

Increasing the well width or indium mole fraction in the well red shifts the transition energy. The barrier material can be chosen to partially reduce the polarization effects. At 525 nm, significant gain can be achieved for small well widths and high indium mole fractions in the active region. It was also shown that with some flexibility in the target wavelength, designs may be identified that still maximize the gain in the required range of spectrum, even under material-related constraints.

Finally, the influence of the choice of buffer material, which defines the in-plane lattice constant, and hence the strain, throughout the active region of a laser diode was analyzed. Barrier strain is shown to be an important consideration, as its inclusion may lead to an enhancement of the optical gain through a reduction of the quantum confined Stark effect.

8.2 *Future research directions*

The following subsections describe future research directions for this thesis.

8.2.1 Electrothermal analysis of metal-oxide-semiconductor HFETs

Conventional AlGa_N/Ga_N HEMTs suffer from large gate leakage currents and surface trap-induced drain current collapse, which may significantly reduce the efficiency and reliability of these devices [18, 205, 30]. It has been shown by Green *et al.* that surface passivation with Si₃N₄ reduces the current collapse [76]. Additionally, Si₃N₄ passivation as a gate insulator significantly suppresses the gate leakage [94]. Such structures are called metal-insulator-semiconductor HFETs (MISHFETs). Several oxides such as SiO₂ [92], Al₂O₃ [81], MgO [112], and Sc₂O₃ [116] have also been used as gate insulators giving rise to metal-oxide-semiconductor HFETs (MOSHFETs), as shown in Figure 62. Using the electrothermal model presented in this thesis in conjunction with the Monte Carlo simulator, the electrical and thermal characteristics of AlGa_N/Ga_N MOSHFETs can be predicted and analyzed.

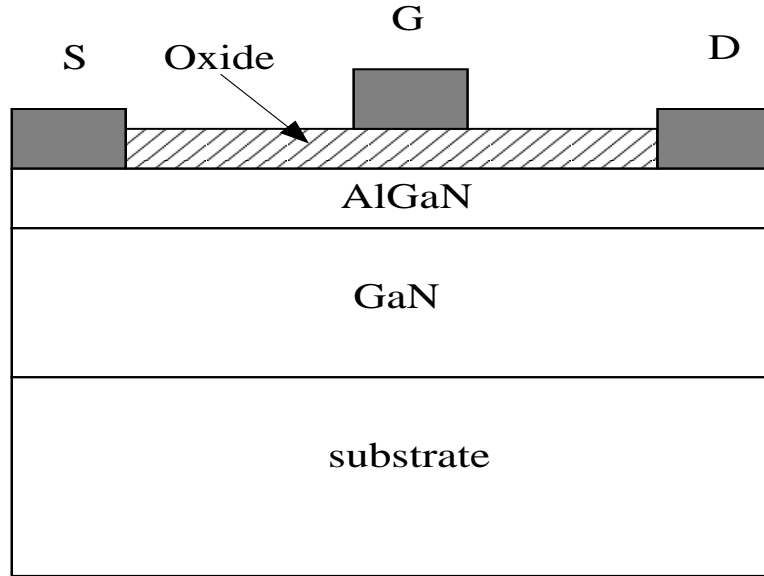


Figure 62: Schematic view of an AlGa_N/Ga_N MOSHFET.

8.2.2 Thermal analysis of InGa_N-based laser diodes

Heat generation and dissipation is a critical issue in high power laser diodes. High operating temperatures result in higher threshold current densities and lower slope

efficiencies. Due to the limitations in p-type doping in nitride-based laser diodes, heat is mainly generated in the p-regions of the device, and this generated heat traverses the active regions of the laser to reach the heat sink placed at the bottom of the substrate, unless top-down mounting is used. To address the thermal issues in GaN-based lasers, the laser simulator can be further extended to include the solution of the lattice heat conduction equation for the acoustic phonons throughout the laser structure, with the source term representing Joule, recombination and/or Thomson/Peltier heat.

REFERENCES

- [1] *MDRAW 10.0 User's Manual*, Synopsys Inc., Mountain View, CA, 2004.
- [2] "T. Mimura, Japanese Patent number 1409643, 8 September 1987."
- [3] AGGARWAL, R. L., MAKI, P. A., MOLNAR, R. J., LIAU, Z. L., and MELNGAILIS, I., "Optically pumped GaN/Al_{0.1}Ga_{0.9}N double-heterostructure ultraviolet laser," *J. Appl. Phys.*, vol. 79, pp. 2148–2150, 1996.
- [4] AHN, D. and CHUANG, S., "Optical gain in a strained-layer quantum-well laser," *IEEE J. Quant. Elec.*, vol. 24, pp. 2400–2406, 1988.
- [5] AHN, D. and CHUANG, S., "Optical gain and gain suppression of quantum-well lasers with valence band mixing," *IEEE J. Quant. Elec.*, vol. 26, pp. 13–24, 1990.
- [6] AKASAKI, I. and AMANO, H., "Recent progress of crystal growth, conductivity control and light emitters of group III nitride semiconductors," in *International Electron Devices Meeting. Technical Digest*, pp. 231–237, 1996.
- [7] AKATAS, O., FAN, Z. F., BOTCHKAREV, A., MOHAMMAD, S. N., ROTH, M., JENKINS, T., KEHIAS, L., and MORKOC, H., "Microwave performance of AlGaIn/GaN inverted MODFET," *IEEE Elec. Dev. Lett.*, vol. 18, pp. 293–295, 1997.
- [8] ALEXANDER, F. B., BIRD, V. R., CARPENTER, D. R., MANLEY, G. W., MCDERMOTT, P. S., PELOKE, J. R., QUINN, H. F., RILEY, R. J., and YETTER, L. R., "Spontaneous and stimulated infrared emission from indium phosphide arsenide diodes," *Appl. Phys. Lett.*, vol. 4, pp. 13–15, 1964.
- [9] AMANO, H., ASAHI, T., and AKASAKI, I., "Stimulated emission near ultraviolet at room temperature from a GaN film grown on sapphire by MOVPE using as AlN buffer layer," *Jpn. J. Appl. Phys.*, vol. 29, pp. L205–L206, 1990.
- [10] AMANO, H., KITO, M., HIRAMATSU, K., and AKASAKI, I., "p-type conduction in Mg-doped GaN treated with low-energy electron beam irradiation (LEEPI)," *Jpn. J. Appl. Phys., Part 2*, vol. 28, pp. L2112–L2114, 1989.
- [11] AMANO, H., SAWAKI, N., AKASAI, I., and TOYODA, T., "Metalorganic vapor phase epitaxial growth of a high quality GaN film using an AlN buffer layer," *Appl. Phys. Lett.*, vol. 48, pp. 353–355, 1986.

- [12] AMANO, H., TANAKA, T., KUNII, Y., KATO, K., KIM, S. T., and AKASAKI, I., "Room-temperature violet stimulated emission from optically pumped AlGa_N/GaInN double heterostructure," *Appl. Phys. Lett.*, vol. 64, pp. 1377–1379, 1994.
- [13] AMBACHER, O., "Growth and applications of group III-nitrides," *Phys. D: Appl. Phys.*, vol. 31, pp. 2653–2710, 1998.
- [14] AMBACHER, O., DIMITROV, R., STUTZMAN, M., FOUTZ, B. E., MURPHY, M. J., SMART, J. A., SHEALY, J. R., WEIMANN, N. G., CHU, K., CHUMBES, M., GREEN, B., SIERAKOWSKI, A. J., SCHAFF, W. J., and EASTMAN, L. F., "Role of Spontaneous and Piezoelectric Polarization Induced Effects in Group-III Nitride Based Heterostructures and Devices," *Phys. Stat. Sol (b)*, vol. 216, pp. 381–389, 1999.
- [15] AMBACHER, O., SMART, J., SHEALY, J. R., WEIMANN, N. G., CHU, K., MURPHY, M., SCHAFF, W. J., EASTMAN, L. F., DIMITROV, R., WITTMER, L., STUTZMAN, M., RIEGER, W., and HILSENBECK, J., "Two-dimensional electron gases induced by spontaneous and piezoelectric polarization charges in N- and G-face AlGa_N/Ga_N heterostructures," *J. Appl. Phys.*, vol. 85, pp. 3222–3233, 1999.
- [16] ARANY, I., SMYTH, W. F., and SZODA, L., "An Improved Method for Reducing the Bandwidth of Sparse Symmetric Matrices," in *Proc. IFIP Congress*, pp. 1246–1250, 1972.
- [17] ARDARAVIČIUS, L., MATULIONIS, A., LIBERIS, J., KIPRIJANOVIC, O., RAMONAS, M., EASTMAN, L. F., SHEALY, J. R., and A., "Electro drift velocity in AlGa_N/Ga_N channel at high electric fields," *Appl. Phys. Lett.*, vol. 83, pp. 4038–4040, 2003.
- [18] ARULKUMARAN, S., EGAWA, T., ISHIKAWA, H., and JIMBO, T., "Temperature dependence of gate-leakage current in AlGa_N/Ga_N high-electron-mobility transistors," *Appl. Phys. Lett.*, vol. 82, pp. 3110–3112, 2003.
- [19] ASTHANA, P., "A long road to overnight success," *IEEE Spectrum Mag.*, vol. 31, pp. 60–66, 1994.
- [20] BARDEEN, J., *Collected works of John von Neumann*, vol. 5.
- [21] BARKER, J. M., FERRY, D. K., GOODNICK, S. M., KOLESKE, D. D., ALLERMAN, A., and SHUL, R. J., "Studies of high field transport in Ga_N/AlGa_N heterostructures," in *2004 7th International Conference on Solid-State and Integrated Circuits Technology*, pp. 2261–2264, 2005.
- [22] BARKER, J. M., FERRY, D. K., KOLESKE, D. D., and SHUL, R. J., "Bulk Ga_N and AlGa_N/Ga_N heterostructure drift velocity measurements and comparison to theoretical models," *J. Appl. Phys.*, vol. 97, pp. 063705–1–063705–5, 2005.

- [23] BARMAN, S. and SRIVASTAVA, G. P., “Long-wavelength nonequilibrium optical phonon dynamics in cubic and hexagonal semiconductors,” *Phys. Rev. B*, vol. 69, pp. 235208–1–235208–16, 2004.
- [24] BATTY, W., CHRISTOFFERSEN, C. E., PRANKS, A. J., DAVID, S., SNOWDEN, C. M., and STEER, M. B., “Electrothermal CAD of power devices and circuits with fully physical time dependent compact thermal modeling of complex nonlinear 3-D systems,” *IEEE Trans. Compon. Packag. Technol.*, vol. 24, pp. 566–590, 2001.
- [25] BEECHEM, T. and GRAHAM, S., “Temperature and doping dependence of phonon lifetimes and decay pathways in GaN,” *J. Appl. Phys.*, vol. 103, pp. 093507–1–093507–8, 2008.
- [26] BERGE, C., *The Theory of Graphs and its Applications*. New York: Wiley, 1962.
- [27] BERNARDINI, F. and FIORENTINI, V., “Macroscopic polarization and band offsets in nitride heterojunctions,” *Phys. Rev. B*, vol. 57, pp. R9427–R9430, 1998.
- [28] BERNARDINI, F. and FIORENTINI, V., “Spontaneous versus piezoelectric polarization in III-V nitrides: Conceptual aspects and practical consequences,” *Phys. Stat. Sol. (b)*, vol. 216, pp. 391–398, 1999.
- [29] BERNARDINI, F., FIORENTINI, V., and VANDERBILT, D., “Spontaneous polarization and piezoelectric constants of III-V nitrides,” *Phys. Rev. B*, vol. 56, pp. R10024–R10027, 1997.
- [30] BINARI, S. C., KLEIN, P. B., and KAZIOR, T. E., “Trapping Effects in GaN and SiC Microwave FETs,” *Proc. IEEE*, vol. 90, pp. 1048–1058, 2002.
- [31] BIR, G. L. and PIKUS, G. E., *Symmetry and Strained-Induced Effects in Semiconductor*. New York: Wiley, 1974.
- [32] BIRDSALL, C. K. and FUSS, D., “Clouds-in-clouds, clouds-in-cells physics for many-body plasma simulation,” *J. Comp. Phys.*, vol. 3, pp. 494–511, 1969.
- [33] BULASHEVICH, K. A., MYMRIN, V. F., KARPOV, S. Y., ZHMAKIN, I. A., and ZHMAKIN, A. I., “Simulation of visible and ultra-violet group-iii nitride light emitting diodes,” *J. Comp. Phys.*, vol. 213, pp. 214–238, 2006.
- [34] BULUTAY, C., DAGLI, N., and IMAMOĞLU, A., “Characterization of excitons in wurtzite GaN quantum wells under valence band mixing, strain and piezoelectric field,” *IEEE J. Quant. Elec.*, vol. 35, pp. 590–602, 1999.
- [35] BUNGARO, C., RAPCEWICZ, K., and BERNHOLC, J., “Ab initio phonon dispersions of wurtzite AlN, GaN, and InN,” *Phys. Rev. B*, vol. 61, pp. 6720–6725, 2000.

- [36] BURK, A. A. J., O'LOUGHLIN, M. J., SIERGIEJ, R. R., AGARWAL, A. K., SRIRAM, S., CLARKE, R. C., MACMILLAN, M. F., BALAKRISHNA, V., and BRANDT, C. D., "SiC and GaN wide bandgap semiconductor materials and devices," *Solid-state Elec.*, vol. 43, pp. 1459–1464, 1999.
- [37] BURNHAM, S. D., *Improved understanding and control of Mg-doped GaN by plasma assisted molecular beam epitaxy*. PhD thesis, School of Electrical and Computer Engineering, Georgia Institute of Technology, 2007.
- [38] CARDONA, M. and MERLIN, R., eds., *Light Scattering in solids IX*. Berlin: Springer, 2007.
- [39] CHAKRABORTY, A., HASKELL, B. A., KELLER, S., SPECK, J. S., DENBAARS, S. P., NAKAMURA, S., and MISHRA, U. K., "Nonpolar InGaN/GaN emitters on reduced-defect lateral epitaxially overgrown a-plane GaN with drive-current-independent electroluminescence emission peak," *Appl. Phys. Lett.*, vol. 85, pp. 5143–5145, 2004.
- [40] CHEN, W. K., ed., *VLSI Technology*. Boca Raton: CRC Press, 2003.
- [41] CHINI, A., COFFIE, R., MENEGHESSO, G., ZANONI, E., BUTTARI, D., HEIKMAN, S., KELLER, S., and MISHRA, U., "2.1A/mm Current Density AlGaIn/GaN HEMT," *Electron. Lett.*, vol. 39, pp. 625–626, 2003.
- [42] CHRISTMAS, U. M. E., ANDREEV, A. D., and FAUX, D. A., "Calculation of electric field and optical transitions in InGaIn/GaN quantum wells," *J. Appl. Phys.*, vol. 98, pp. 073522–1–073522–12, 2005.
- [43] CHUANG, S. L., *Physics of Optoelectronic Devices*. New York: Wiley, 1995.
- [44] CHUANG, S. L., "Optical gain of strained wurtzite GaN quantum-well lasers," *IEEE J. Quant. Elec.*, vol. 32, pp. 1791–1800, 1996.
- [45] CHUANG, S. and CHANG, C., "k.p method for strained wurtzite semiconductors," *Phys. Rev. B*, vol. 54, pp. 2491–2504, 1996.
- [46] COOKE, M., "Gallium nitride futures and other stories," *III-Vs Review*, vol. 19, pp. 20–24, 2006.
- [47] CRAFT, M. G., HOLONYAK, N. J., and KISH, F. A. J., "In pursuit of the ultimate lamp," *Scientific American*, vol. 284, pp. 62–67, 2001.
- [48] CRANK, J. and NICOLSON, P., "A practical method for numerical evaluation of solutions of partial differential equations of the heat-conduction type," *Proc. Camb. Philos. Soc.*, vol. 43, pp. 50–67, 1947.
- [49] CUTHILL, E. and MCKEE, J., "Reducing the Bandwidth of Sparse Symmetric Matrices," in *Proc. ACM National Conference, Association for Computing Machinery*, pp. 157–172, 1969.

- [50] DEGUCHI, T., SEKIGUCHI, K., NAKAMURA, A., SOTA, T., MATSUO, R., CHICHIBU, S., and NAKAMURA, S., “Quantum-Confined Stark Effect in an AlGa_N/Ga_N/AlGa_N Single Quantum Well Structure,” *Jpn. J. Appl. Phys.*, vol. 38, pp. L914–L916, 1999.
- [51] DINGLE, D., SHAKLEE, K. L., LEHENY, R. F., and ZETTERSTROM, R. B., “Stimulated emission and laser action in Gallium Nitride,” *Appl. Phys. Lett.*, vol. 19, pp. 5–7, 1971.
- [52] DOEBELIN, E. O., *System dynamics: modeling, analysis, simulation, design*. CRC Press, 1998.
- [53] DRÄGER, A. D., JÖNEN, H., BREMERS, H., ROSSOW, U., DEMOLON, P., SCHENK, H. P. D., DUBOZ, J. Y., CORBETT, B., , and HANGLEITER, A., “Towards green lasing: ingredients for a green laser diode based on GaInN,” *Phys. Stat. Sol. (c)*, vol. 34, p. DOI 10.1002/pssc.200880963, 2009.
- [54] DRESSELHAUS, G., KIP, A., and KITTEL, C., “Cyclotron resonance of electrons and holes in silicon and germanium crystals,” *Phys. Rev.*, vol. 98, pp. 368–384, 1955.
- [55] DUBOZ, J. Y., “Ga_N as seen by the industry,” *Phys. Stat. Sol. A*, vol. 176, pp. 5–14, 1999.
- [56] DUPUIS, R. D., DAPKUS, P. D., JR., N. H., REZEK, E. A., and CHIN, R., “Room-temperature laser operation of quantum-well Ga_(1-x)Al_xAs-GaAs laser diodes grown by metalorganic chemical vapor deposition,” *Appl. Phys. Lett.*, vol. 32, pp. 295–297, 1978.
- [57] EASTMAN, L. F. and MISHRA, U. K., “The toughest transistor yet,” *IEEE Spectrum Mag.*, vol. 39, pp. 28–33, 2002.
- [58] EASTMAN, L. F., TILAK, V., SMART, J., GREEN, B. M., CHUMBES, E. M., DIMITROV, R., KIM, H., AMBACHER, O. S., WEIMANN, N., PRUNTY, T., MURPHY, M., SCHAFF, W. J., and SHEALY, J. R., “Undoped AlGa_N/Ga_N HEMTs for Microwave Power Amplification,” *IEEE Trans. Elect. Dev.*, vol. 48, pp. 479–485, 2001.
- [59] EISENSTAT, S. C., GURSKY, M. C., SCHULTZ, M. H., and SCHERMAN, A. H., “The Yale Sparse Matrix Package 1: The symmetric codes,” *Int. J. Numer. Methods Eng.*, vol. 18, pp. 1145–1151, 1982.
- [60] ELASSER, A. and CHOW, T. P., “Silicon Carbide benefits and advantages for power electronics circuits and systems,” *Proc. IEEE*, vol. 90, pp. 969–986, 2002.
- [61] FARRELL, R. M., FEEZELL, D. F., SCHMIDT, M. C., HAEGER, D. A., KELCHNER, K. M., ISO, K., YAMADA, H., SAITO, M., FUJITO, K., COHEN,

- D. A., SPECK, J. S., DENBAARS, S. P., and NAKAMURA, S., "Continuous-wave operation of AlGa_N-cladding-free nonpolar m-plane InGa_N/Ga_N laser diodes," *Jpn. J. Appl. Phys.*, vol. 46, pp. L761–763, 2007.
- [62] FEEZELL, D. F., SCHMIDT, M. C., FARRELL, R. M., KIM, K.-C., SAITO, M., FUJITO, K., COHEN, D. A., SPECK, J. S., DENBAARS, S. P., and NAKAMURA, S., "AlGa_N-cladding-free nonpolar m-plane InGa_N/Ga_N laser diodes," *Jpn. J. Appl. Phys.*, vol. 46, pp. L284–286, 2007.
- [63] FIORENTINI, V., BERNARDINI, F., SALA, F. D., CARLO, A. D., and LUGLI, P., "Effects of macroscopic polarization in III-V nitride multiple quantum wells," *Phys. Rev. B*, vol. 60, pp. 8849–8858, 1999.
- [64] FUHRMAN, D., JÖNEN, H., HOFFMANN, L., BREMERS, H., ROSSOW, U., and HANGLEITER, A., "High quality, high efficiency and ultrahigh In-content InGa_N QWs-the problem of thermal stability," *Phys. Stat. Sol. (c)*, vol. 5, pp. 1662–1664, 2008.
- [65] FUNATO, M., UEDA, M., KAWAKAMI, Y., NARUKAWA, Y., KOSUGI, T., TAKAHASHI, M., and MUKAI, T., "Blue, Green and Amber InGa_N/Ga_N Light-Emitting Diodes on Semipolar 1122 Ga_N Bulk Substrates," *Jpn. J. Appl. Phys.*, vol. 45, pp. L659–L662, 2006.
- [66] GALCZAK, J., SARZAŁA, R. P., and NAKWASKI, W., "The modified **k.p** method to investigate polarization effects in nitride quantum-well devices," *Phys. E*, vol. 25, pp. 504–514, 2005.
- [67] GASKA, R., OSINSKY, A., YANG, J. W., and SHUR, M. S., "Self-heating in high-power AlGa_N-Ga_N HFETs," *IEEE Elect. Dev. Letts.*, vol. 19, pp. 89–91, 1998.
- [68] GASKA, R., SHUR, M. S., BYKHOVSKI, A., ORLOV, A. O., and SNIDER, G. L., "Electron mobility in modulation-doped AlGa_N-Ga_N heterostructures," *Appl. Phys. Lett.*, vol. 74, pp. 287–289, 1999.
- [69] GASKA, R., YANG, J. W., OSINSKY, A., CHEN, Q., KHAN, M. A., ORLOV, A. O., SNIDER, G. L., and SHUR, M. S., "Electron transport in AlGa_N-Ga_N heterostructures grown on 6H-SiC substrates," *Appl. Phys. Lett.*, vol. 72, pp. 707–709, 1998.
- [70] GEORGE, A., *Computer Implementation of the Finite Element Method*. PhD thesis, Stanford University, 1971.
- [71] GEORGE, A., "An automatic one-way dissection algorithm for irregular finite element problems," *SIAM Jour. Numer. Anal.*, vol. 17, pp. 740–751, 1980.
- [72] GEORGE, A. and LIU, J. W. H., "An Implementation of a Pseudoperipheral Node Finder," *ACM Transactions on Mathematical Software*, vol. 5, pp. 284–295, 1979.

- [73] GIL, B., ed., *Group III Nitride Semiconductor Compounds: Physics and Applications*. New York: Oxford Univ. Press, 1998.
- [74] GIL, B., ed., *Low-dimensional nitride semiconductors*, ch. Electron-phonon interaction in GaN and its low-dimensional structures. Oxford Univ. Press, 2002.
- [75] GRANDJEAN, N., DAMILANO, B., DALMASSO, S., LEROUX, M., and LA M.
- [76] GREEN, B. M., CHU, K. K., CHUMBES, E. M., SMART, A. J., SHEALY, J. R., and EASTMAN, L. F., "The effect of surface passivation on the microwave characteristics of undoped AlGa_N/Ga_N HEMTs," *IEEE Elect. Dev. Lett.*, vol. 21, pp. 268–270, 2000.
- [77] GRUPEN, M., *The self-consistent simulation of carrier transport and its effect on the modulation response in semiconductor quantum well laser*. PhD thesis, University of Illinois at Urbana-Champaign, 1994.
- [78] GURNETT, K. and ADAMS, T., "Considerations for GaN-powered base stations," *III-Vs Rev.*, vol. 19, pp. 20–22, 2006.
- [79] HAASE, M. A., QUI, J., DEPUYDT, J. M., and CHENG, H., "Blue-green laser diodes," *Appl. Phys. Lett.*, vol. 59, pp. 1272–1274, 1991.
- [80] HALL, R. N., FENNER, G. E., KINGSLEY, J. D., SOLTYS, T. J., and CARLSON, R. O., "Coherent light emission from GaAs junctions," *Phys. Rev. Lett.*, vol. 9, pp. 366–368, 1962.
- [81] HASHIZUME, T., ANANTATHANASARN, S., NEGORO, N., SANO, E., HASEGAWA, H., KUMAKURA, K., and MAKIMOTO, T., "Al₂O₃ insulated-gate structure for AlGa_N/Ga_N heterostructure field effect transistors having thin AlGa_N barrier layers," *Japan. J. Appl. Phys.*, vol. 43, pp. L777–L779, 2004.
- [82] HAYASHI, I. and PANISH, M. B., "GaAs-Ga_xAl_{1-x}As heterostructure injection lasers which exhibit low thresholds at room temperature," *J. Appl. Phys.*, vol. 41, pp. 150–163, 1970.
- [83] HEIBLUM, M., GALBI, D., and WECKWERTH, M., "Observation of single-optical-phonon emission," *Phys. Rev. Lett.*, vol. 62, pp. 1057–1060, 1989.
- [84] HINCKLEY, J. M. and SINGH, J., "Influence of substrate composition and crystallographic orientation on the band structure of pseudomorphic Si-Ge alloy films," *Phys. Rev. B*, vol. 42, pp. 3546–3566, 1990.
- [85] HOLONYAK, N. J. and BEVACQUA, S. F., "Coherent (visible) light emission from Ga(As_{1-x}P_x) junctions," *Appl. Phys. Lett.*, vol. 1, pp. 82–83, 1962.
- [86] HOLONYAK N., J., "Is the light emitting diode (LED) an ultimate lamp?," *Am. J. Phys.*, vol. 68, pp. 864–868, 2000.

- [87] JIANG, H. and SINGH, J., “Linear electro-optic effect due to the built-in electric field in InGaN/GaN quantum wells,” *Appl. Phys. Lett.*, vol. 75, pp. 1932–1934, 1999.
- [88] JOSHIN, K., KIKKAWA, T., HAYASHI, H., MANIWA, T., YOKOKAWA, S., YOKOYAMA, M., ADACHI, N., and TAKIKAWA, M., “A 174 W high-efficiency GaN HEMT power amplifier for W-CDMA base station applications,” in *IEEE IEDM Tech. Dig.*, pp. 12.6.1–12.6.3, 2003.
- [89] KANE, E. O., “Band structure of Indium Antimonide,” *J. Phys. Chem. Solids.*, vol. 1, pp. 249–261, 1957.
- [90] KASH, J. and TSANG, J., “Secondary Emission Studies of hot carrier relaxation in polar semiconductors,” *Solid State Elect.*, vol. 31, pp. 419–424, 1988.
- [91] KHAN, A. M., KUZNIA, J. N., OLSON, D. T., SCHAFF, W. J., BURM, W. J., and SHUR, M. S., “Microwave performance of a $0.25\mu\text{m}$ gate AlGaIn/GaN Heterostructure Field Effect Transistor,” *Appl. Phys. Lett.*, vol. 65, pp. 1121–1123, 1994.
- [92] KHAN, M. A., HU, X., LUNEV, G. S. A., YANG, J., GASKA, R., and SHUR, M. S., “AlGaIn/GaN Metal oxide semiconductor heterostructure field effect transistors,” *IEEE Elect. Dev. Lett.*, vol. 21, pp. 63–65, 2000.
- [93] KHAN, M. A., KRISHNANKUTTY, S., SKOGMAN, R. A., KUZNIA, J. N., and OLSON, D. T., “Vertical-cavity stimulated emission from photopumped InGaIn/GaN heterojunctions at room temperature,” *Appl. Phys. Lett.*, vol. 65, pp. 520–521, 1994.
- [94] KHAN, M. A., SHUR, M. S., and SIMIN, G., “Strain-engineered novel III-N electronic devices with high quality dielectric/semiconductor interfaces,” *Phys. Status Solidi (a)*, vol. 200, pp. 155–160, 2003.
- [95] KIM, H. S., LIN, J. Y., JIANG, H. X., CHOW, W. W., BOTCHKAREV, A., and MORKOÇ, H., “Piezoelectric effects on the optical properties of $\text{gan/al}_x\text{ga}_{1-x}\text{n}$ multiple quantum wells,” *Appl. Phys. Lett.*, vol. 73, pp. 3426–3428, 1998.
- [96] KIM, K. S., SON, J. K., LEE, S. N., SUNG, Y. J., PAEK, H. S., KIM, H. K., KIM, M. Y., HA, K. H., RYU, H. Y., NAM, O. H., JANG, T., and PARK, Y. J., “Characteristics of long wavelength InGaIn quantum well laser diodes,” *Appl. Phys. Lett.*, vol. 92, pp. 101103–1–101103–3, 2008.
- [97] KIM, S. T., AMANO, H., and AKASAKI, I., “Surface-mode stimulated emission from optically pumped GaInN at room temperature,” *Appl. Phys. Lett.*, vol. 67, pp. 267–269, 1995.
- [98] KOCEVAR, P., “Hot phonon dynamics,” *Physica B+C*, vol. 134, pp. 155–163, 1985.

- [99] KOLOKOLOV, K. I., LI, J., and NING, C. Z., “k.p Hamiltonian without spurious-state solutions,” *Phys. Rev. B*, vol. 68, pp. 161308–1–161308–4, 2003.
- [100] KOZODOY, P., XING, H. L., DENBAARS, S. P., MISHRA, U. K., SAXLER, A., PERRIN, R., ELHAMRI, S., and MITCHEL, W. C., “Heavy doping effects in Mg-doped GaN,” *J. Appl. Phys.*, vol. 87, pp. 1832–1835, 2000.
- [101] KRESSEL, H. and NELSON, H. *RCA Rev.*, vol. 30, p. 106, 1969.
- [102] KROEMER, H., “A proposed class of hetero-junction lasers,” *Proc. IEEE*, vol. 51, pp. 1782–1783, 1963.
- [103] KUNOLD, A. and PEREYRA, P., “Photoluminescence transitions in semiconductor superlattices. Theoretical calculations for InGaN blue laser device,” *J. Appl. Phys.*, vol. 93, pp. 5018–5024, 2003.
- [104] LAI, C. Y., HSU, T. M., CHANG, W. H., TSENG, K. U., LEE, C. M., CHUO, C. C., and CHYI, J. I., “Direct measurement of piezoelectric field in $\text{In}_{0.23}\text{Ga}_{0.77}\text{N}/\text{GaN}$ multiple quantum wells by electrotransmission spectroscopy,” *J. Appl. Phys.*, vol. 91, pp. 531–533, 2002.
- [105] LANGER, R., SIMON, J., ORTIZ, V., PELEKANOS, N. T., BARSKI, A., ANDRÉ, R., and GODLEWSKI, M., “Giant electric fields in unstrained GaN single quantum wells,” *Appl. Phys. Lett.*, vol. 74, pp. 3827–3829, 1999.
- [106] LAUX, S., “On particle-mesh coupling in Monte Carlo semiconductor device simulation,” *IEEE Trans. Computer-Aided Design*, vol. 15, pp. 1266–1277, 1996.
- [107] LEROUX, M., GRANDJEAN, N., LAÜGT, M., MASSIES, J., GIL, B., LEFEBVRE, P., and BIGENWALD, P., “Quantum confined Stark effect due to built-in internal polarization fields in $(\text{Al,Ga})\text{N}/\text{GaN}$ quantum wells,” *Phys. Rev B*, vol. 58, pp. R13371–R13374, 1998.
- [108] LÖWDIN, P., “A note on the quantum-mechanical perturbation theory,” *J. Phys. Chem.*, vol. 19, pp. 1396–1401, 1951.
- [109] LIN, M. E., STRITE, S., AGARWAL, A., SALVADOR, A., ZHOU, G. L., TERAGUCHI, N., ROCKETT, A., and MORKOÇ, H., “GaN grown on hydrogen plasma and cleaned 6H-SiC substrates,” *Appl. Phys. Lett.*, vol. 62, pp. 702–704, 1993.
- [110] LIU, W. and SHERMAN, A., “Comparative Analysis of the Cuthill-McKee and the reverse Cuthill-McKee ordering algorithms for sparse matrices,” *SIAM Jour. Numer. Anal.*, vol. 13, pp. 198–213, 1976.
- [111] LONG, D., *Energy Bands in Semiconductors*. New York: Interscience, 1968.

- [112] LUO, B., JOHNSON, J. W., KIM, J., MEHANDRU, R. M., REN, F., GILA, B. P., ONSTINE, A. H., ABERNATHY, C. R., PEARTON, S. J., BACA, A. G., BRIGGS, R. D., SHUL, R. J., MONIER, C., and HAN, J., "Influence on MgO and Sc₂O₃ passivation on AlGa_xN/GaN high-electron-mobility transistors," *Appl. Phys. Lett.*, vol. 80, pp. 1661–1663, 2002.
- [113] MATULIONIS, A., "Hot-electron transport and noise in GaN two-dimensional channels for HEMTs," *IEICE Trans. Elect.*, vol. E89-C, pp. 913–920, 2006.
- [114] MATULIONIS, A., LIBERIS, J., ARDARAVIČIUS, L., EASTMAN, L. F., SHEALY, J. R., and VERTIATCHIKH, A., "Hot-phonon lifetime in AlGa_xN/GaN at a high lattice temperature," *Semicond. Sci. Technol.*, vol. 19, pp. S421–S423, 2004.
- [115] MATULIONIS, A., LIBERIS, J., MATULIONIENE, I., RAMONAS, M., EASTMAN, L. F., SHEALY, J. R., TILAK, V., and VERTIATCHIKH, A., "Hot-phonon temperature and lifetime in a biased Al_xGa_{1-x}N/GaN channel estimated from noise analysis," *Phys. Rev. B*, vol. 68, p. 035338, 2003.
- [116] MEHANDRU, R., LUO, B., KIM, J., REN, F., GILA, B. P., ONSTINE, A. H., ABERNATHY, C. R., PEARTON, S. J., GOTTHOLD, D., BIRKHAHN, R., and PERES, B., "AlGa_xN/GaN metal-oxide-semiconductor high electron mobility transistors using Sc₂O₃ as the gate oxide and surface passivation," *Appl. Phys. Lett.*, vol. 82, pp. 2530–2532, 2003.
- [117] MELNGAILIS, I. and REDIKER, R. H., "Properties of InAs diode masers," *IEEE Trans. Elect. Dev.*, vol. 10, pp. 333–334, 1963.
- [118] MIMURA, T., HIYAMIZU, S., FUJII, T., and NANBU, K., "A New Field-Effect Transistor with Selectively Doped GaAs/n-Al_xGa_{1-x}As heterojunctions," *Jpn. J. Appl. Phys.*, vol. 19, pp. L225–L227, 1980.
- [119] MIMURA, T., JOSHIN, K., HIYAMIZU, S., HIKOSAKA, K., and ABE, M., "High Electron Mobility Transistor Logic," *Jpn. J. Appl. Phys.*, vol. 20, pp. L598–L600, 1981.
- [120] MINSKY, M. S., FLEISCHER, S. B., ABARE, A. C., BOWERS, J. E., HU, E. L., KELLER, S., and DENBAARS, S. P., "Characterization of high-quality InGa_xN/GaN multiquantum wells with time-resolved photoluminescence," *Appl. Phys. Lett.*, vol. 72, pp. 1066–1068, 1998.
- [121] MISHRA, U. K., PARIKH, P., and WU, Y., "AlGa_xN/GaN HEMTs—an overview of device operation and applications," *Proc. IEEE*, vol. 90, pp. 1022–31, 2002.
- [122] MOHAMMAD, S. N., SALVADOR, A. A., and MORKOÇ, H., "Emerging Gallium Nitride Based Devices," *Proc. of the IEEE*, vol. 83, pp. 1306–1355, 1995.
- [123] MONEMAR, B. and POZINA, G., "Group III-nitride based hetero and quantum structures," *Prog. Quant. Elect.*, vol. 24, pp. 239–290, 2000.

- [124] MORKOÇ, H., *Nitride Semiconductors and Devices*. Berlin: Springer, 1999.
- [125] NAKAMURA, S., “GaN growth using GaN buffer layer,” *Jpn. J. Appl. Phys., Part 2*, vol. 30, pp. L1705–L1707, 1991.
- [126] NAKAMURA, S. and CHICHIBU, S. F., eds., *Introduction to nitride semiconductor blue lasers and light emitting diodes*, ch. Theoretical analysis of optical gain spectra. Taylor and Francis, 2000.
- [127] NAKAMURA, S., MUKAI, T., SENOH, M., and IWASA, I., “Thermal annealing effects on p-type Mg-doped GaN films,” *Jpn. J. Appl. Phys. Part 1*, vol. 31, pp. L139–L142, 1992.
- [128] NAKAMURA, S., PEARTON, S., and FASOL, G., *The Blue Laser Diode*. Berlin: Springer, 2000.
- [129] NAKAMURA, S., SENOH, M., IWASA, N., NAGAHAMA, S., YAMADA, T., and MUKAI, T., “Superbright green InGaN single-quantum-well-structure light emitting diodes,” *Jpn. J. Appl. Phys.*, vol. 34, pp. L1332–L1335, 1995.
- [130] NAKAMURA, S., SENOH, M., NAGAHAMA, S., and IWASA, N., “Continuous-wave operation of InGaN multi-quantum-well-structure laser diodes at 233K,” *Appl. Phys. Lett.*, vol. 69, pp. 3034–3036, 1996.
- [131] NAKAMURA, S., SENOH, M., NAGAHAMA, S., IWASA, N., and YAMADA, T., “InGaN-based multi-quantum-well-structure laser diodes,” *Jpn. J. Appl. Phys.*, vol. 35, pp. L74–L75, 1996.
- [132] NAMKOONG, G., DOOLITTLE, W. A., and BROWN, A. S., “Incorporation of Mg in GaN grown by plasma-assisted molecular beam epitaxy,” *Appl. Phys. Lett.*, vol. 77, pp. 4386–4388, 2000.
- [133] NATHAN, M. I., DUMKE, W. P., BURNS, G., DILL, F. H. J., and LASHER, G., “Stimulated emission of radiation from GaAs p-n junctions,” *Appl. Phys. Lett.*, vol. 1, pp. 62–64, 1962.
- [134] NIWA, A., OHTOSHI, T., and KURODA, T., “Valence subband structures of (10 $\bar{1}$ 0)-GaN/AlGaIn strained quantum wells calculated by the tight-binding method,” *Appl. Phys. Lett.*, vol. 70, pp. 2159–2160, 1997.
- [135] NYE, J. F., *Physical Properties of Crystals*. Oxford: Oxford University Press, 1985.
- [136] OHTOSHI, T., NIWA, A., and KURODA, T., “Crystal Orientation Effect on Valence-Subband Structures in Wurtzite-GaN Strained Quantum Wells,” *Jpn. J. Appl. Phys. 2*, vol. 35, pp. L1566–L1568, 1996.
- [137] OHTOSHI, T., NIWA, A., and KURODA, T., “Dependence of optical gain on crystal orientation in wurtzite-GaN strained quantum-well lasers,” *J. Appl. Phys.*, vol. 82, pp. 1518–1520, 1997.

- [138] OKAMOTO, K., OHTA, H., CHICHIBU, S. F., ICHIHARA, J., and TAKASU, H., "Continuous-wave operation of m-plane InGaN multiple quantum well laser diodes," *Jpn. J. Appl. Phys.*, vol. 46, pp. L187–L189, 2007.
- [139] OYAFUSO, F., *Fully Coupled Electrical and Optical Simulation of Vertical Cavity Surface Emitting Lasers*. PhD thesis, University of Illinois at Urbana-Champaign, 2001.
- [140] OYAFUSO, F., VON ALLMEN, P., and HESS, K., "Inclusion of bandstructure and many-body effects in a quantum well laser simulator," *VLSI Design*, vol. 8, pp. 463–468, 1998.
- [141] PALACIOS, T., CHAKRABORTY, A., KELLER, S., DENBAARS, S. P., and MISHRA, U. K., "Optimization of Device Structure and Harmonic Tuning in AlGaIn/GaN HEMTs for High Power Added Efficiency," in *Proc. of the International Symposium on Compound Semiconductors*, 2005.
- [142] PALACIOS, T., CHAKRABORTY, A., RAJAN, S., POBLENZ, C., KELLER, S., DENBAARS, S. P., SPECK, J. S., and MISHRA, U. K., "High-power AlGaIn/GaN HEMTs for Ka-band applications," *IEEE Elec. Dev. Lett.*, vol. 26, pp. 781–783, 2005.
- [143] PANISH, M. B., HAYASHI, I., and SUMSKI, S., "Double-heterostructure injection lasers with room-temperature thresholds as low as 2300 A/cm^2 ," *Appl. Phys. Lett.*, vol. 16, pp. 326–327, 1970.
- [144] PARK, J., SHIN, M. W., and LEE, C. C., "Thermal Modeling and Measurement of AlGaIn-GaN HFETs Built on Sapphire and SiC Substrates," *IEEE Trans. Elect. Dev.*, vol. 51, pp. 1753–1759, 2004.
- [145] PARK, S. H., "Effect of $(10\bar{1}0)$ crystal orientation on many-body optical gain of wurtzite InGaIn/GaN quantum well," *J. Appl. Phys.*, vol. 93, pp. 9665–9668, 2003.
- [146] PARK, S. H., "Piezoelectric and spontaneous polarization effects on many-body optical gain of wurtzite InGaIn/GaN quantum well with arbitrary crystal orientation," *Jpn. J. Appl. Phys.*, vol. 42, pp. 5052–5055, 2003.
- [147] PARK, S. H., "Optical anisotropy in non-polar $(10\bar{1}0)$ -oriented *m*-plane GaIn/AlGaIn quantum wells and comparison with experiment," *Appl. Phys. A*, vol. 91, pp. 361–364, 2008.
- [148] PARK, S. H., AHN, D., and CHUANG, S. L., "Electronic and Optical Properties of a- and m-plane wurtzite InGaIn-GaN quantum wells," *IEEE J. Quant. Elec.*, vol. 43, pp. 1175–1182, 2007.
- [149] PARK, S. H., AHN, D., and OH, J. E., "Optical anisotropy in ultraviolet InGaIn/GaN quantum-well light emitting diodes with a general crystal orientation," *Appl. Phys. Lett.*, vol. 92, pp. 011130–1–011130–3, 2008.

- [150] PARK, S. H. and S. L. CHUANG, “Crystal-orientation effects on the piezoelectric field and electronic properties of strained wurtzite semiconductors,” *Phys. Rev. B*, vol. 59, pp. 4725–4737, 1999.
- [151] PEARTON, S. J., ed., *GaN and Related Materials*. Amsterdam: Gordon and Breach, 1997.
- [152] PEARTON, S. J., REN, F., ZHANG, A. P., and LEE, K. P., “Fabrication and performance of GaN electronic devices,” *Mat. Sci. Eng. R: Reports*, vol. R30, pp. 55–212, 2000.
- [153] PENG, H. Y., MCCLUSKEY, M. D., GUPTA, Y. M., KNEISSEL, M., and JOHNSON, N. M., “Shock-induced band-gap shift in GaN: Anisotropy of the deformation potentials,” *Phys. Rev. B*, vol. 71, p. 115207, 2005.
- [154] PIPREK, J., ed., *Nitride Semiconductor Devices: Principles and Simulation*, ch. Electron Bandstructure Parameters. Wiley-VCH, 2007.
- [155] PIPREK, J., ed., *Nitride Semiconductor Devices: Principles and Simulation*, ch. Introduction. Wiley-VCH, 2007.
- [156] PIPREK, J., ed., *Nitride Semiconductor Devices: Principles and Simulation*, ch. Interband Transition in InGaN Quantum Wells. Wiley-VCH, 2007.
- [157] PIPREK, J., ed., *Nitride Semiconductor Devices: Principles and Simulation*, ch. Visible light emitting diodes. Wiley-VCH, 2007.
- [158] PIPREK, J., FARRELL, R., DENBAARS, S., and NAKAMURA, S., “Effects of built-in polarization on InGaN-GaN vertical-cavity surface-emitting lasers,” *IEEE Photon. Tech. Lett.*, vol. 18, pp. 7–9, 2006.
- [159] POP, E., DUTTON, R., and GOODSON, K., “Detailed Heat Generation Simulations via the Monte Carlo Method,” in *2003 IEEE International Conference on Simulation of Semiconductor Processes and Devices*, pp. 121–124, 2003.
- [160] QUIST, T. M., REDIKER, R. H., KEYES, R. J., KRAG, W. E., LAX, B., MCWHORTER, A. L., and ZEIGER, H. J., “Semiconductor maser of GaAs,” *Appl. Phys. Lett.*, vol. 1, pp. 91–92, 1962.
- [161] RAMONAS, M., MATULIONIS, A., LIBERIS, J., EASTMAN, L., CHEN, X., and SUN, Y. J., “Hot-phonon effect on power dissipation in a biased $\text{Al}_x\text{Ga}_{1-x}\text{N}/\text{GaN}$ channel,” *Phys. Rev. B*, vol. 71, pp. 075324–1–075324–8, 2005.
- [162] REN, G. B. and BLOOD, P., “Many-body effects in GaN/AlGaN quantum well with the spin-orbit interaction,” in *Conference on Lasers and Electro-Optics, CLEO '99*, pp. 171–172, 1999.
- [163] REN, G. B., LIU, Y. M., and BLOOD, P., “Valence-band structure of wurtzite GaN including the spin-orbit interaction,” *App. Phys. Lett.*, vol. 74, pp. 1117–1119, 1999.

- [164] RIDLEY, B. K., “The LO phonon lifetime in GaN,” *J. Phys.: Condens. Matter*, vol. 8, pp. L511–L513, 1996.
- [165] ROMANOV, A. E., BAKER, T. J., NAKAMURA, S., and SPECK, S., “Strain-induced polarization in wurtzite III-nitride semipolar layers,” *J. Appl. Phys.*, vol. 100, pp. 023522–1–023522–10, 2006.
- [166] ROSE, D. J. and WILLOUGHBY, R. A., eds., *Sparse Matrices and Their Applications*, ch. Several Strategies for Reducing the Bandwidth of Matrices. Plenum Press, 1972.
- [167] RYOU, J. H., YODER, P. D., LIU, J., LOCHNER, Z., KIM, H., CHOI, S., KIM, H. J., and DUPUIS, R. D., “Control of quantum-confined stark effect in InGaN-based quantum wells,” *IEEE J. Selected topics Quant. Elec.*, vol. in press, 2009.
- [168] SADI, T., KELSALL, R. W., and PILGRIM, N. J., “Investigation of Self-Heating Effects in Submicrometer GaN/AlGaN HEMTs Using an Electrothermal Monte Carlo Method,” *IEEE Trans. Elect. Dev.*, vol. 53, pp. 2892–2900, 2006.
- [169] SALOKATVE, A., JEON, H., HOVINEN, M., KELKAR, P., NURMIKKO, A. V., GRILLO, D. C., HE, L., HAN, J., FAN, Y., RINGLE, M., and GUNSHOR, R. L., “Low voltage, room temperature, ridge waveguide green-blue diode laser,” *Elect. Lett.*, vol. 29, pp. 2041–2042, 1993.
- [170] SCHARFETTER, D. L. and GUMMEL, H. K., “Large-signal analysis of a silicon read diode oscillator,” *IEEE Trans. Elect. Dev.*, vol. 16, pp. 64–77, 1969.
- [171] SCHMIDT, M. C., KIM, K.-C., FARRELL, R. M., FEEZELL, D. F., COHEN, D. A., SAITO, M., FUJITO, K., SPECK, J. S., DENBAARS, S. P., and NAKAMURA, S., “Demonstration of Nonpolar m-plane InGaN/GaN Laser Diodes,” *Jpn. J. Appl. Phys.*, vol. 46, pp. L190–L191, 2007.
- [172] SCHMIDT, T. J., YANG, X. H., SHAN, W., SONG, J. J., SALVADOR, A., KIM, W., AKTAS, O., BOTCHKAREV, A., and MORKOÇ, H., “Room-temperature stimulated emission in GaN/AlGaN separate confinement heterostructures grown by molecular beam epitaxy,” *Appl. Phys. Lett.*, vol. 68, pp. 1820–1822, 1996.
- [173] SEITZ, F., “The theoretical constitution of metallic lithium,” *Phys. Rev.*, vol. 47, pp. 400–412, 1935.
- [174] SEITZ, F., *Modern Theory of Solids*. New York: McGraw Hill, 1940.
- [175] SELBERHERR, S., *Analysis and Simulation of Semiconductor Devices*. Verlag: Springer, 1984.

- [176] SHARMA, R., PATTISON, P. M., MASUI, H., FARRELL, R. M., BAKER, T. J., HASKELL, B. A., WU, F., DENBAARS, S. P., SPECK, J. S., and NAKAMURA, S., “Demonstration of a semipolar (10 $\bar{1}$ 3) InGa \bar{N} /Ga \bar{N} green light emitting diode,” *Appl. Phys. Lett.*, vol. 87, pp. 231110–231112, 2005.
- [177] SHEIH, S. J., TSEN, K. T., FERRY, D. K., BOTCHKAREV, A., SVERDLOV, B., SALVADOR, A., and MORKOÇ, H., “Electron-phonon interactions in the wide band-gap semiconductor Ga \bar{N} ,” *Appl. Phys. Lett.*, vol. 67, pp. 1757–1759, 1996.
- [178] SHEPPARD, S. T., DOVERSPIKE, K., PRIBBLE, W. L., ALLEN, S. T., and PALMOUR, J. W., “High power microwave Ga \bar{N} /AlGa \bar{N} HEMTs on silicon carbide,” *IEEE Elec. Dev. Lett.*, vol. 20, pp. 161–163, 1999.
- [179] SHOCKLEY, W., “Energy band structures in semiconductors,” *Phys. Rev.*, vol. 78, pp. 173–174, 1950.
- [180] SMITH, D. L. and MAILHIOT, C., “Piezoelectric effect in strained-layer superlattices,” *J. Appl. Phys.*, vol. 63, pp. 2717–19, 1998.
- [181] SONG, D. Y., NIKISHIN, S. A., HOLTZ, M., SOUKHOVEEV, V., USIKOV, A., and DIMITRIEV, V., “Decay of zone-center phonons in Ga \bar{N} with A_1 , E_1 , and E_2 symmetries,” *J. Appl. Phys.*, vol. 101, pp. 053535–1–053535–6, 2007.
- [182] SONG, G. H., *Two-dimensional Simulation of Quantum-well Lasers Including Energy Transport*. PhD thesis, University of Illinois at Urbana-Champaign, 1990.
- [183] SPECK, J. and ROSNER, S. J., “The role of threading dislocations in the physical properties of Ga \bar{N} and its alloys,” *Physica B*, vol. 273, pp. 24–32, 1999.
- [184] SRIDHARAN, S., VENKATACHALAM, A., and YODER, P. D., “Electrothermal Analysis of AlGa \bar{N} /Ga \bar{N} High Electron Mobility Transistors,” *J. Comput. Electron.*, vol. 7, pp. 236–239, 2008.
- [185] SRIDHARAN, S. and YODER, P. D., “Anisotropic transient and stationary electron velocity in bulk wurtzite Ga \bar{N} ,” *IEEE Elect. Dev. Lett.*, vol. 29, pp. 1190–1192, 2008.
- [186] SUN, D. and TOWE, E., “Strain-Generated Internal Fields in Pseudomorphic (In,Ga)As/GaAs Quantum Well Structures on 11 \bar{l} GaAs Substrates,” *Japan. J. Appl. Phys.*, vol. 33, pp. 702–708, 1994.
- [187] SUZUKI, H., OHISHI, M., KAIFU, N., ISHIKAWA, S., and KASUGA, T., “Detection of the Interstellar C $_6$ H Radical,” *Publ. Astron. Soc. Japan*, vol. 38, pp. 911–917, 1986.

- [188] SUZUKI, M., UENOYAMA, T., and YANASE, A., “First-principles calculations of effective-mass parameters of AlN and GaN,” *Phys. Rev. B*, vol. 52, pp. 8132–8139, 1995.
- [189] TAKEUCHI, T., AMANO, H., and AKASAKI, I., “Theoretical Study of Orientation Dependence of Piezoelectric Effects in Wurtzite Strained GaInN/GaN Heterostructures and Quantum Wells,” *Japan. J. Appl. Phys.*, vol. 39, pp. 413–416, 2000.
- [190] TAKEUCHI, T., SOTA, S., KATSURAGAWA, M., KOMORI, M., TAKEUCHI, H., AMANO, H., and AKASAKI, I., “Quantum-confined stark effect due to piezoelectric fields in gainn strained quantum wells,” *Japan. J. Appl. Phys.*, vol. 36, pp. L382–385, 1997.
- [191] TAKEUCHI, T., WETZEL, C., YAMAGUCHI, S., SAKAI, H., AMANO, H., AKASAKI, I., KANEKO, Y., NAKAGAWA, S., and YAMADA, N., “Determination of piezoelectric fields in strained GaInN quantum wells using the quantum-confined stark effect,” *Appl. Phys. Lett.*, vol. 73, pp. 1691–1693, 1998.
- [192] TRAETTA, G., PASSASEO, A., LONGO, M., CANNOLETTA, D., CINGOLANI, R., LOMASCOLO, M., BONFIGLIO, A., CARLO, A. D., SALA, F. D., LUGLI, P., BOTCHKAREV, A., and MORKOÇ, H., “Effects of the spontaneous polarization and piezoelectric fields on the luminescence spectra of gan/al_{0.15}ga_{0.85}n quantum wells,” *Physica E*, vol. 7, pp. 929–933, 2000.
- [193] TREW, R. J., “Wide bandgap semiconductor transistors for microwave power amplifiers,” *IEEE Micro. Mag.*, vol. 1, pp. 46–54, 2000.
- [194] TSEN, K. T., FERRY, D. K., BOTCHKAREV, A., SVERDLOV, B., SALVADOR, A., and MORKOC, H., “Direct measurements of electron-longitudinal optical phonon scattering rates in wurtzite GaN,” *Appl. Phys. Lett.*, vol. 71, pp. 1852–1853, 1997.
- [195] TSEN, K. T., FERRY, D. K., BOTCHKAREV, A., SVERDLOV, B., SALVADOR, A., and MORKOÇ, H., “Time-resolved Raman Studies of the decay of the Longitudinal Optical phonons in wurtzite GaN,” *App. Phys. Lett.*, vol. 72, pp. 2132–2134, 1998.
- [196] TSEN, K. T., JOSHI, R. P., FERRY, D. K., BOTCHKAREV, A., SVERDLOV, B., SALVADOR, A., and MORKOÇ, H., “Nonequilibrium electron distributions and phonon dynamics in wurtzite GaN,” *App. Phys. Lett.*, vol. 68, pp. 2990–2992, 1996.
- [197] TYAGI, A., LIN, Y., COHEN, D. A., SAITO, M., FUJITO, K., SPECK, J. S., DENBAARS, S. P., and NAKAMURA, S., “Stimulated emission at blue-green (480 nm) and green (514 nm) wavelengths from nonpolar (m-plane) and semipolar (11 $\bar{2}2$) InGa \bar{N} multiple quantum well laser diode structures,” *Appl. Phys. Expr.*, vol. 1, pp. 091103–1–091103–3, 2008.

- [198] TYAGI, A., ZHONG, H., CHUNG, R. B., FEEZELL, D. F., SAITO, M., FUJITO, K., SPECK, J. S., DENBAARS, S. P., and NAKAMURA, S., “Semipolar (10 $\bar{1}\bar{1}$) InGa \bar{N} /Ga \bar{N} laser diodes on bulk Ga \bar{N} substrates,” *Jpn. J. Appl. Phys.*, vol. 46, pp. L444–445, 2007.
- [199] TYAGI, A., ZHONG, H., FELLOWS, N. N., IZA, M., SPECK, J. S., DENBAARS, S. P., and NAKAMURA, S., “High Brightness Violet InGa \bar{N} /Ga \bar{N} Light Emitting Diodes on Semipolar (10 $\bar{1}\bar{1}$) Bulk Ga \bar{N} Substrates,” *Jpn. J. Appl. Phys.*, vol. 46, pp. L129–L131, 2007.
- [200] UENOYAMA, T. and SUZUKI, M., “Valence subband structures of wurtzite Ga \bar{N} /AlGa \bar{N} quantum wells,” *Appl. Phys. Lett.*, vol. 67, pp. 2527–2529, 1995.
- [201] VALLÉE, F., “Time-resolved investigation of coherent LO-phonon relaxation in III-V semiconductors,” *Phys. Rev. B*, vol. 49, pp. 2460–2468, 1994.
- [202] VARGA, R. S., *Matrix Iterative Analysis*. Englewood Cliffs: Prentice-Hall, 1962.
- [203] VENKATACHALAM, A., KLEIN, B., and YODER, P. D., “Design strategies in InGa \bar{N} -based green lasers,” *IEEE J. Quant. Elec.*, vol. under review, 2009.
- [204] VENKATACHALAM, A., YODER, P. D., KLEIN, B., and KULKARNI, A., “Nitride band-structure model in a quantum well laser simulator,” *Opt. Quant. Electron.*, vol. 40, pp. 295–299, 2008.
- [205] VETURY, R., ZHANG, N. Q., KELLER, S., and MISHRA, U. K., “The impact of surface states on the DC and RF characteristics of AlGa \bar{N} /Ga \bar{N} HFETs,” *IEEE. Trans. Elect. Dev.*, vol. 48, pp. 560–566, 2001.
- [206] VON ALLMEN, P., “Derivation of the effective-mass equation for a superlattice: A perturbational approach,” *Phys. Rev. B*, vol. 46, pp. 15277–15381, 1992.
- [207] WALTEREIT, P., BRANDT, O., TRAMPERT, A., GRAHN, H. T., MENNINGER, J., RAMSTEINER, M., REICHE, M., and PLOOG, K. H., “Nitride semiconductors free of electrostatic fields for efficient white light-emitting diodes,” *Nature*, vol. 406, pp. 865–868, 2000.
- [208] WEBER, H. J. and ARFKEN, G. B., *Essential mathematical methods for physicists*. Academic Press, 2004.
- [209] WEISER, K., LEVITT, R. S., NATHAN, M. I., and BURNS, G., “Indium phosphide laser characteristics,” *IEEE Trans. Elect Dev.*, vol. 10, pp. 334–334, 1963.
- [210] WEITZEL, C. E., PALMOUR, J. W., CARTER, C. H. J., MOORE, K., NORDQUIST, K. J., ALLEN, S., THERO, C., and BHATNAGAR, M., “Silicon carbide high-power devices,” *IEEE Trans. Elec. Dev.*, vol. 43, pp. 1732–1741, 1996.

- [211] WILLANDER, M. and HARTNAGEL, H. L., eds., *High Temperature Electronics*. London: Chapman and Hall, 1997.
- [212] WITZIGMANN, B., LAINO, V., LUISIER, M., ROEMER, F., FEICHT, G., and SCHWARZ, U. T., "Simulation and design of optical gain in In(Al)GaN/GaN short wavelength lasers," in *Semiconductor Lasers and Laser Dynamics*, pp. 61840E-1-61840E-8, 2006.
- [213] WITZIGMANN, B., LAINO, V., LUISIER, M., SCHWARZ, U. T., FEICHT, G., WEGSCHEIDER, W., ENGL, K., FURITSCH, M., LEBER, A., LELL, A., and Härle, V., "Microscopic analysis of optical gain in InGa_N/Ga_N quantum wells," *Appl. Phys. Lett.*, vol. 88, pp. 021104-1-021104-3, 2006.
- [214] WITZIGMANN, B., TOMAMICHEL, M., STEIGER, S., VEPREK, R. G., KOJIMA, K., and SCHWARZ, U. T., "Analysis of gain and luminescence in violet and blue GaInN-GaN quantum wells," *IEEE J. Quant. Elec.*, vol. 44, pp. 144-149, 2008.
- [215] WU, Y.-F., KELLER, B. P., KELLER, S., KAPOLNEK, D., DENBAARS, S. P., and MISHRA, U. K., "Measured Microwave Power Performance of AlGa_N/Ga_N MODFET," *IEEE Elec. Dev. Lett.*, vol. 17, pp. 455-457, 1996.
- [216] WU, Y.-F., KELLER, B. P., KELLER, S., KAPOLNEK, D., KOZODOY, P., DENBAARS, S. P., and MISHRA, U. K., "High Power AlGa_N/Ga_N HEMTs for Microwave Applications," *Solid State Electron.*, vol. 41, pp. 1569-1574, 1997.
- [217] WU, Y.-F., KELLER, B. P., KELLER, S., NGUYEN, N., LE, M., NGUYEN, C., JENKINS, T. J., DENBAARS, S. P., and MISHRA, U. K., "Short channel AlGa_N/Ga_N MODFETs with 50GHz f_t and 1.7-W/mm output-power at 10GHz," *IEEE Elec. Dev. Lett.*, vol. 18, pp. 438-440, 1997.
- [218] WU, Y.-F., KELLER, B. P., KELLER, S., XU, J. J., THIBEAULT, B. J., DENBAARS, S. P., and MISHRA, U. K., "Ga_N-based FETs for Microwave Power Amplification," *IEICE Trans. Elec.*, vol. E82-C, pp. 1895-1905, 1999.
- [219] WU, Y.-F., KELLER, B. P., P.FINI, KELLER, S., DENBAARS, S. P., and MISHRA, U. K., "High Al-content AlGa_N/Ga_N MODFETs for ultra-high performance," *IEEE Elec. Dev. Lett.*, vol. 19, pp. 50-53, 1998.
- [220] WU, Y.-F., KELLER, B. P., P.FINI, PUSL, J., LE, M., NGUYEN, N. X., NGUYEN, C., WIDMAN, D., KELLER, S., DENBAARS, S. P., and MISHRA, U. K., "Short-channel Al_{0.5}Ga_{0.85}N/Ga_N MODFETs with power density > 3W/mm at 18GHz," *Elec. Lett.*, vol. 33, pp. 1742-1743, 1997.
- [221] WU, Y.-F., KELLER, S., KOZODOY, P., KELLER, B. P., PARIKH, P., KAPOLNEK, D., DENBAARS, S. P., and MISHRA, U. K., "Bias dependent microwave performance of AlGa_N/Ga_N MODFETs up to 100V," *IEEE Elec. Dev. Lett.*, vol. 18, pp. 290-292, 1997.

- [222] WU, Y. F., SAXLER, A., MOORE, M., SMITH, R. P., SHEPPARD, S., CHAVARKAR, P. M., WISLEDER, T., MISHRA, U. K., and PARIKH, P., “30-W/mm GaN HEMTs by Field Plate Optimization,” *IEEE Electron Dev. Lett.*, vol. 25, pp. 117–119, 2004.
- [223] WU, Y.-R. and SINGH, J., “Transient study of self-heating effects in Al-GaN/GaN HFETs: Consequence of carrier velocities, temperature, and device performance,” *J. Appl. Phys.*, vol. 101, p. 113712, 2007.
- [224] YAMAKAWA, S., SARANITI, M., and GOODNICK, S. M., “High field transport in GaN and AlGaIn/GaN heterojunctions,” in *Ultrafast Phenomena in Semiconductors and Nanostructure Materials XI and Semiconductor Photodetector IV*, pp. 64710M–1–7, 2007.
- [225] YEO, Y. C., CHONG, T. C., and LI, M. F., “Effect of the (10 $\bar{1}$ 0) crystal orientation on the optical gain of wurtzite GaN-AlGaIn quantum well lasers,” *IEEE. J. Quant. Elect.*, vol. 34, pp. 1270–1279, 1998.
- [226] YEO, Y. C., CHONG, T. C., and LI, M. F., “Electronic band structures and effective-mass parameters of wurtzite GaN and InN,” *J. Appl. Phys.*, vol. 83, pp. 1429–1436, 1998.
- [227] YEO, Y. C., CHONG, T. C., LI, M. F., and FAN, W. J., “Analysis of optical gain and threshold current density of wurtzite InGaIn/GaN/AlGaIn quantum well lasers,” *J. Appl. Phys.*, vol. 84, pp. 1813–1819, 1998.
- [228] YU, T. and BRENNAN, K. F., “Theoretical study of the two-dimensional electron mobility in strained III-nitride heterostructures,” *J. Appl. Phys.*, vol. 89, pp. 3827–3834, 2001.
- [229] YU, T. and BRENNAN, K. F., “Monte Carlo calculation of two-dimensional electron dynamics in GaN-AlGaIn heterostructures,” *J. Appl. Phys.*, vol. 91, pp. 3730–3736, 2002.
- [230] ZORY, P. S. J., *Quantum Well Lasers*. San Diego: Academic Press, 1993.
- [231] ZUBRILOV, A. S., NIKOLAEV, V. I., TSVETKOV, D. V., DMITRIEV, V. A., IRVINE, K. G., EDMOND, J. A., and C. H. CARTER, J., “Spontaneous and stimulated emission from photopumped GaN grown on SiC,” *Appl. Phys. Lett.*, vol. 67, pp. 533–535, 1995.

VITA

Anusha Venkatachalam earned the Bachelor of Engineering (B. E.) degree in Electronics and Telecommunication Engineering from K. J. Somaiya College of Engineering at University of Mumbai, India, in 2001, the Master of Science (M. S.) degree in Electrical Engineering from Syracuse University, Syracuse in 2002 and is expected to receive her Ph.D. in Electrical and Computer Engineering from Georgia Institute of Technology in 2009. Her advisor is Dr. Douglas Yoder.

She has been previously involved with the simulation and modeling of silicon-based metal oxide semiconductor field effect transistors. Her current research focuses on the theory, simulation and design of nitride-based high field effect transistors and blue and green lasers.

She has taken a variety of courses for her major and Math courses for her minor. She has attended and published in conferences including the international conference on numerical simulation of optoelectronic devices (NUSOD) in 2007. She is a member of Phi Beta Delta-an international honor society.